

Investigation of the activity and physical properties of the active asteroids 324P/La Sagra, 2010 LH15, and 62412 (2000 SY178)

Von der Fakultät für Elektrotechnik, Informationstechnik, Physik
der Technischen Universität Carolo-Wilhelmina zu Braunschweig

zur Erlangung des Grades einer Doktorin
der Naturwissenschaften (Dr. rer. nat.)

genehmigte Dissertation

von Maria Mastropietro
aus Maratea, Italy

1. Referentin:	Prof. Dr. Jessica Agarwal
2. Referent:	Prof. Dr. Jürgen Blum
eingereicht am:	24.01.2025
Disputation am:	24.04.2025

Druckjahr: 2025

**Dissertation an der Technischen Universität Braunschweig,
Fakultät für Elektrotechnik, Informationstechnik, Physik**

Abstract

Dust emissions from asteroids are commonly attributed to the sublimation of exposed ice, which can lead to comet-like activity in main-belt comets, or to disruptions from impacts or rapid rotation, which may expose sub-surface ice for sublimation. This thesis investigates the physical and dynamical characteristics of two main-belt comets, 324P/La Sagra and 2010 LH15, as well as the disrupted asteroid 62412 (2000 SY178).

For 324P/La Sagra, my research examines the temporal evolution of its activity during the 2010, 2015, and 2021 perihelion passages. A significant decline in activity was observed, potentially due to surface mantling or the depletion of volatile materials. An analysis of the $Af\rho$ profile of the coma revealed a transition near perihelion from a lower-activity pre-perihelion phase to a higher-activity steady state in the post-perihelion period. Additionally, I calculated the dust geometric albedo to range from 2% to 45%, which complicates efforts to accurately constrain the spectral type of 324P/La Sagra. Nevertheless, observations indicate evidence of dust superheating at a wavelength of 4.5 μm . A distinctive feature of 324P/La Sagra is the formation of a gap between the nucleus and its tail following the cessation of activity. The size of this gap helps constrain the dimensions of the largest ejected particles. Using the syndyne-synchrone modeling, I analyzed a faint dust trail of 324P/La Sagra captured during inactivity in 2011. This analysis indicated that the sizes of the large dust particles ranged from 0.2 mm to 0.8 mm, ejected over three months. The gas production rates were consistent with values observed for other main-belt comets, such as 238P/Read.

The study of 2010 LH15 focused on its inactive nucleus, which was observed in July 2023. Photometric measurements yielded an absolute R-band magnitude of (18.4 ± 0.2) mag, corresponding to a nucleus radius of (0.5 ± 0.1) km, assuming a C-type geometric albedo. Analysis of its lightcurve revealed no evidence of a rotational period shorter than two hours, highlighting the need for further investigation into its rotational dynamics.

Lastly, this thesis explores the disrupted asteroid 62412 during its 2024 perihelion passage to determine whether it reactivated close to perihelion. Following its 2013 perihelion, 62412 displayed dust emission, likely due to rotational destabilization as a result of its fast rotation. My analysis of archival data and pre-2024 perihelion observations showed significant changes in its lightcurve amplitude and brightness post-2013, suggesting modifications in its shape and size. If confirmed, the absence of reactivation during subsequent perihelion passages may be due to a lack of exposed ice or low surface temperatures resulting from its high perihelion distance of 2.9 AU.

Zusammenfassung

Staubemissionen von Asteroiden werden üblicherweise auf die Sublimation von freigelegtem Eis zurückgeführt, was bei Hauptgürtelkometen zu kometenähnlicher Aktivität führen kann, oder auf Störungen durch Einschläge oder schnelle Rotation, die unterirdisches Eis zur Sublimation freilegen können. In dieser Arbeit werden die physikalischen und dynamischen Eigenschaften von zwei Hauptgürtelkometen, 324P/La Sagra und 2010 LH15, sowie des zerbrochenen Asteroiden 62412 (2000 SY178) untersucht.

Bei 324P/La Sagra untersuchte ich die zeitliche Entwicklung seiner Aktivität während der Periheldurchgänge 2010, 2015 und 2021. Es wurde ein signifikanter Rückgang der Aktivität beobachtet, der möglicherweise auf eine Oberflächenverhüllung oder die Erschöpfung flüchtiger Stoffe zurückzuführen ist. Eine Analyse des $Af\rho$ -Profils der Koma ergab einen Übergang in der Nähe des Perihels von einer Phase mit geringerer Aktivität vor dem Perihel zu einem stabilen Zustand mit höherer Aktivität in der Zeit nach dem Perihel. Darüber hinaus berechnete ich eine geometrische Staubalbedo zwischen 2% und 45%, was die genaue Bestimmung des Spektraltyps von 324P/La Sagra erschwert. Dennoch deuten die Beobachtungen auf eine Staubüberhitzung bei einer Wellenlänge von 4.5 μm hin. Ein charakteristisches Merkmal von 324P/La Sagra ist die Bildung einer Lücke zwischen dem Kern und seinem Schweif nach dem Ende der Aktivität. Die Größe dieser Lücke hilft, die Dimensionen der größten ausgestoßenen Teilchen einzugrenzen. Mithilfe der Sydneyne-Synchrone-Modellierung analysierte ich eine schwache Staubschweifspur von 324P/La Sagra, die während der Inaktivität im Jahr 2011 aufgenommen wurde. Diese Analyse ergab, dass die Größe der großen Staubteilchen zwischen 0.2 mm und 0.8 mm lag, die über drei Monate hinweg ausgestoßen wurden. Die Gasproduktionsraten stimmten mit den Werten überein, die bei anderen Kometen des Hauptgürtels, wie 238P/Read, beobachtet wurden.

Die Untersuchung von 2010 LH15 konzentrierte sich auf seinen inaktiven Kern, der im Juli 2023 beobachtet wurde. Photometrische Messungen ergaben eine absolute R-Band-Magnitude von (18.4 ± 0.2) mag, was einem Kernradius von (0.5 ± 0.1) km entspricht, wobei eine geometrische Albedo vom Typ C angenommen wird. Die Analyse seiner Lichtkurve ergab keinen Hinweis auf eine Rotationsperiode von weniger als zwei Stunden, was die Notwendigkeit weiterer Untersuchungen seiner Rotationsdynamik unterstreicht.

Schließlich wird in dieser Arbeit der gestörte Asteroid 62412 während seines Periheldurchgangs im Jahr 2024 untersucht, um festzustellen, ob er in der Nähe des Perihels reaktiviert wurde. Nach seinem Perihel im Jahr 2013 zeigte 62412 Staubemissionen, die wahrscheinlich auf eine Destabilisierung der Rotation infolge seiner schnellen Rotation zurückzuführen sind. Meine Analyse von Archivdaten und Beobachtungen vor dem Perihel im Jahr 2024 zeigte signifikante Veränderungen in der Amplitude und Helligkeit seiner Lichtkurve nach 2013, was auf Veränderungen in seiner Form und Größe schließen lässt. Sollte sich dies bestätigen, könnte das Ausbleiben der Reaktivierung während der nachfolgenden Perihelpassagen auf einen Mangel an freiliegendem Eis oder auf niedrige Oberflächentemperaturen zurückzuführen sein, die sich aus seinem großen Perihelabstand von 2.9 AE ergeben.

Contents

1	Introduction	1
1.1	Small bodies	1
1.1.1	Asteroids	1
1.1.2	Near Earth Objects	10
1.1.3	Comets	11
1.1.4	TransNeptunian Objects	16
1.2	Active asteroids	17
1.2.1	Activity processes	20
1.3	The main-belt comet 324P/La Sagra	21
1.4	The main-belt comet 2010 LH15	22
1.5	The disrupted asteroid 62412 (2000 SY178)	22
1.6	Motivation	24
2	Concepts	27
2.1	Data reduction	27
2.1.1	Bias subtraction and flat-fielding	27
2.1.2	Photometric calibration	28
2.2	Photometry methods	29
2.2.1	Methods for visible light images	29
2.2.2	Methods for infrared images	30
2.3	Dust tail brightness profile method	31
2.4	Dust tail modelling	35
2.4.1	The Finson and Probst model	35
2.4.2	The syndynes and synchrones model	35
2.4.3	Implementation	36
3	Analysis of 324P/La Sagra	39
3.1	Dataset	39
3.1.1	Telescopes	39
3.1.2	Observations	39
3.2	Photometry	46
3.2.1	Photometry in visible light	46
3.2.2	Photometry in infrared	49
3.2.3	Nucleus magnitude	51
3.2.4	Aperture size dependence of dust absolute magnitudes and $Af\rho$	52
3.2.5	Dust mass estimates and onset of activity	54
3.2.6	Spectral energy distribution	57
3.3	Dust tail analysis	60
3.3.1	Dust tail brightness profile	60
3.3.2	Comparison of the synchrones ages	65
3.3.3	Gas production rate	67
3.3.4	Size distribution of particles	69

3.3.5	Dust-to-gas ratio	70
3.3.6	Particle velocities	72
4	Photometry on the nucleus of 2010 LH15	75
4.1	Dataset	75
4.1.1	Telescopes	75
4.1.2	Observations	75
4.2	Photometry	76
4.3	Lightcurve measurements and rotational period	78
4.4	Nucleus radius	79
5	Investigating the activity of the disrupted asteroid 62412 (2000 SY178)	81
5.1	Dataset	81
5.1.1	Telescopes	81
5.1.2	Observations	81
5.2	Photometry	83
5.3	Lightcurve measurements and rotational period	83
5.4	Nucleus radius size	83
5.5	Comparison with the literature	83
6	Summary, discussions and outlook	87
6.1	324P/La Sagra: Temporal activity and dust emission	87
6.2	2010 LH15: Comparative analysis	89
6.3	62412: A non-sublimation-driven active asteroid	89
6.4	Limitations and future work	90
	Bibliography	93
	Publications and conference proceedings	105
	Curriculum Vitae	107
	Acknowledgments	109

1 Introduction

1.1 Small bodies

According to IAU (International Astronomical Union) resolution B5 of 2006¹, any object that is not classified as a satellite, planet, or dwarf planet is considered a small Solar System body. This category includes asteroids, near Earth objects (NEO), comets, and transNeptunian objects (TNO) in the Kuiper belt, Scattered Disk, and Detached Scattered Disk (Spohn 2011; Davidsson et al. 2021).

1.1.1 Asteroids

Asteroids are bodies made of rocks, that orbit the Sun. They do not have sufficient mass for self-gravity to overcome the structural strength of their material. This lack of hydrostatic equilibrium prevents them to have a round shape. The first asteroid discovered was 1 Ceres in 1801, which was reclassified as a dwarf planet in 2006 (Spohn 2011). In 2014, Küppers et al. (2014) detected water vapor plumes on it.

Asteroids are remnants from the early stages of the Solar System, approximately 4.6 Gyr ago. During this period, dust and gas in the protoplanetary disk agglomerated into planetesimals (Pfalzner et al. 2015). Collisions among these planetesimals sometimes resulted in fragmentation, forming the present-day asteroids (Bottke et al. 2005). The gravitational influence of Jupiter prevented the formation of a planet from these bodies, leaving them as asteroids (Spohn 2011). These small bodies contain valuable information about the origin and evolution of the planets, providing insights into their original composition.

Size

While there are about a thousand asteroids larger than 30 kilometers and over 200 larger than 100 kilometers, calculations suggest the existence of roughly one million smaller asteroids, many of which have diameters around one kilometer, with some being smaller or larger. Sizes are estimated using thermal radiation or scattered light measurements, or occultations, where an asteroid passes in front of a star, or using radar measurements (Binzel et al. 1991).

Shape and rotation

Asteroids exhibit variability in brightness and rotational period. This variability can be caused by their irregular shapes and different surface features, which reflect sunlight unevenly as the asteroid rotates. Most asteroids are irregularly shaped due to insufficient gravity to pull them into a spherical shape. However, some larger bodies, such as the asteroid 4 Vesta, have sufficient mass to approximate a round shape (Lupishko & Mohamed 2009). Similarly, 1 Ceres, which was formerly classified as an asteroid, was designated a dwarf planet in 2006 due to its large size, nearly spherical shape, and its state of hydrostatic equilibrium.

¹<https://www.iau.org/news/pressreleases/detail/iau0603/>.

Lightcurves, which plot magnitude versus time, are crucial to determine the shape and spin rates of asteroids, satellites, comets, and TNOs. Typically displaying a sinusoidal periodic behavior with two maxima and two minima due to the rotation of an object, the amplitude of the lightcurve (difference between maximum and minimum brightness) indicates the elongation of a body, or can be due to bright and dark areas on its surface. Analyzing these lightcurves, often through methods like Fourier analysis, helps determine the rotational period of the object. Over years or even decades, careful monitoring can reveal changes in the rotational period of the object. Adequate lightcurve data can also provide insights into the shape and spin axis orientation (Spohn 2011).

Asteroids smaller than 125 kilometers in diameter can be shattered by major collisions. In contrast, asteroids larger than 200 meters possess sufficient mass for their gravity to either hold them together or cause the fragmented pieces to reassemble into a mass that spins more rapidly than before the impact. Many of these large, rapidly rotating, and elongated asteroids are thought to be gravitationally bound rubble piles, formed by collisions, held together by gravity, and with thoroughly shattered interiors (Binzel et al. 1991).

Location

The majority of asteroids in our Solar System are found within the main asteroid belt, located between Mars and Jupiter at a mean inclination of approximately 10° relative to the solar ecliptic plane. These asteroids have semimajor axes ranging from 2.1 to 3.3 AU from the Sun. The three largest asteroids (Ceres, Pallas, and Vesta) comprise nearly half of the total mass of the belt (Binzel et al. 1991).

Some asteroids are located in regions defined by orbital resonances, which occur when the orbital period of an asteroid forms a simple ratio with that of a planet, creating either stable or unstable configurations. Stable resonances include the 1:1 resonance, where objects like the Trojans share the same heliocentric distance and orbital period as Jupiter (Fig. 1.1). These Trojans orbit within two stable regions, known as Lagrange points, located 60° ahead of and behind Jupiter in its orbit. Similarly, Hilda asteroids reside in the 3:2 resonance with Jupiter, completing three orbits around the Sun for every two of the orbit of Jupiter. These resonances create stable regions where asteroids can remain for long timescales. In contrast, unstable resonances can lead to the removal or redirection of asteroids, contributing to the formation of gaps in the asteroid belt, such as the Kirkwood gaps. For instance, the 3:1 resonance, where an asteroid completes three orbits around the Sun for each orbit of Jupiter, produces chaotic motions that can redirect asteroids from the main belt into Earth-crossing orbits (see Sect. 1.1.2) (Binzel et al. 1991).

Kirkwood gaps and asteroids families

The gravitational influence of Jupiter significantly shapes the structure of the asteroid belt. Kirkwood (1867) recognized patterns in the asteroid distribution, the Kirkwood gaps, which correspond to specific orbital resonances with Jupiter. These resonances not only create gaps but also lead to the formation of distinct asteroid groupings or families within the belt (Fig. 1.1). The same gravitational resonances are believed to have prevented the formation of a planet in the region between Mars and Jupiter by increasing the orbital eccentricities of planetesimals. This led to high-speed collisions, that made accretion impossible. Consequently, the asteroid belt is characterized by high-velocity collisions, resulting in the fragmentation and dispersion of asteroids (Binzel et al. 1991).

Some asteroid family clusters, such as Themis, Eos and Koronis (Hirayama 1918), or Flora (Tedesco 1979), are believed to be remnants of larger parent bodies that were disrupted by collisions. The study of these families provides information on the interiors of the precursor asteroids (Binzel et al. 1991).

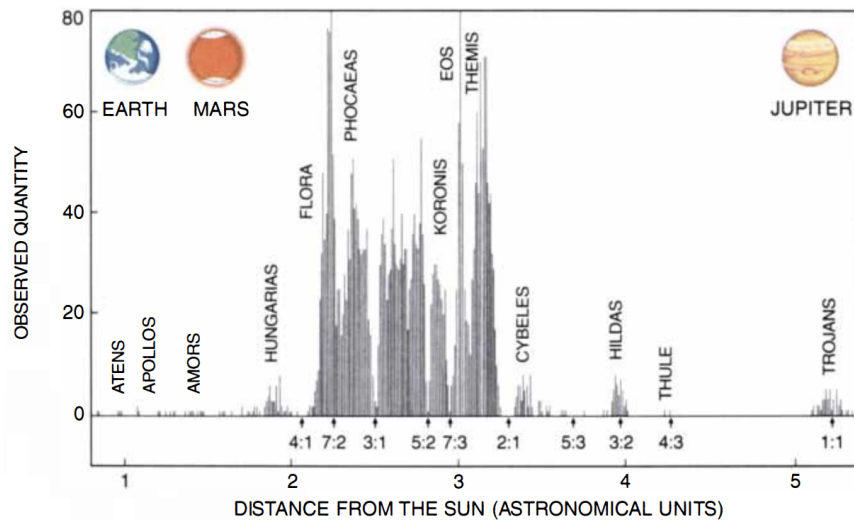


Figure 1.1: Asteroids locations, Kirkwood gaps and asteroids families. Credit: Binzel et al. (1991).

Yarkovsky and YORP effect

The Yarkovsky and Yarkovsky-O'Keefe-Radzievskii-Paddack (YORP) effects are thermal radiation forces and torques that impact the behavior of small celestial bodies, especially asteroids. The Yarkovsky effect influences the orbits of asteroids by producing a net force due to the differential heating and cooling of their surfaces as they rotate. Over time, this can alter their paths. The YORP effect affects the spin rates and orientations of asteroids by generating torques through similar thermal processes. This can lead to changes in spin rates, orientations, and in some cases, even causing the asteroid to split apart (Bottke et al. 2006).

Diurnal component of the Yarkovsky effect When the asteroid rotates, the side facing the Sun absorbs solar insolation and heats up, with the absorbed heat later being re-radiated into space. This process generates a net thermal force acting in the direction opposite to the heat absorption, inducing a change in the orbit of the asteroid. Thermal re-radiation produces a radiation recoil force that influences the trajectory of the asteroid. If the asteroid has prograde rotation, this effect causes it to gradually spiral outward, whereas retrograde rotation would result in an inward spiral (Fig. 1.2). The magnitude of the diurnal effect depends on several factors, including the proximity of the body to the Sun, the tilt of its spin axis², and its physical characteristics such as size, shape, thermal properties, and rotation speed (Bottke et al. 2006).

²Obliquity, also known as axial tilt, is the angle between the rotational axis of an object and its orbital axis.

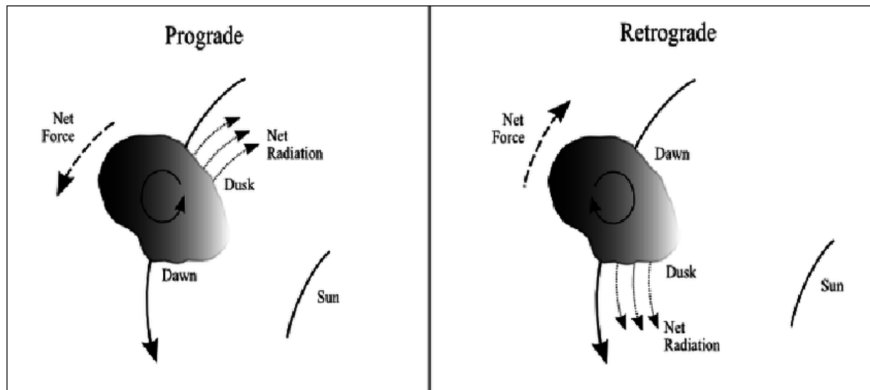


Figure 1.2: Yarkovsky diurnal effect depending on the rotation direction of the asteroid. Credit: Hyland et al. (2013), Figure 1.

Seasonal component of the Yarkovsky effect The seasonal component of the Yarkovsky effect results from the seasonal heating and cooling of the hemispheres of the body as it orbits, which creates a net thermal force acting along the spin axis. It operates regardless of the rotation direction of the body, consistently acting to shrink the orbit whether the body rotates prograde or retrograde (Fig. 1.3). Due to thermal inertia, there is a delay in the heating of the body, so the hottest part is not in the direction of the Sun anymore but at a different point in the orbit. This delay generates an average along-track force that opposes the motion of the asteroid, leading to orbital decay (Bottke et al. 2006), which is why the effect was originally called "thermal drag" (Rubincam 1987). The strength of the seasonal Yarkovsky effect is influenced by the proximity of the body to the Sun and the tilt of its spin axis. It vanishes when the spin axis is perpendicular to the orbital plane (Bottke et al. 2006). The effect is most pronounced in basaltic bodies in the inner main belt with size of around 10 meters (Farinella et al. 1998; Rubincam 1998). For small eccentricities it tends to circularize the orbit (Rubincam 1995, 1998; Vokrouhlický & Farinella 1998, 1999).

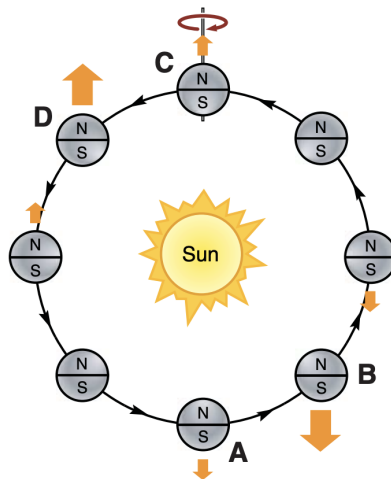


Figure 1.3: Yarkovsky seasonal effect. Credit: Bottke et al. (2006), Figure 1.

YORP effect The YORP effect is a thermal radiation torque on asteroids with irregular shapes that affects the spin rates and obliquities of small bodies. This effect arises from changes in the rotation of the asteroid due to the uneven distribution of heat on its surface, caused by solar radiation. The YORP effect can result in various evolutionary paths for asteroids. Some may consistently spin down, while others spin up, according to the direction of the rotation (Fig. 1.4). Some may even switch between these states over time, as the YORP torques can alter asteroid obliquities, creating the YORP cycle. Initially, the YORP effect increases the spin rate of the asteroid and its obliquity as well. However, at high obliquity, the effect reverses and slows down the spin, potentially causing the asteroid to enter an irregular tumbling state, where it no longer rotates smoothly around a single axis but instead spins irregularly around multiple axes. During this period, the rotational axis of the asteroid can re-orient itself randomly. Eventually, the asteroid might settle into a new principal axis of rotation. Once the asteroid stabilizes its rotation, the YORP effect can start influencing its spin and obliquity again, potentially initiating the cycle anew (Bottke et al. 2006). Energy reradiated from a symmetrical body produces no net YORP torque (Rubincam 2000; Bottke et al. 2002; Vokrouhlický & Čapek 2002).

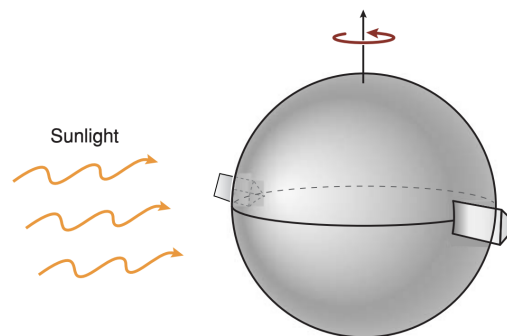


Figure 1.4: Spin up of an asteroid due to the YORP effect. Credit: Bottke et al. (2006), Figure 5.

Differentiated and undifferentiated asteroids

Differentiated asteroids originate through processes that cause the separation of their materials based on density, primarily due to heating and melting. Initially, they form from the aggregation of dust and small rocky fragments in the early Solar System, a process known as accretion, resulting in the creation of an early-stage, asteroid-sized object called a planetesimal. As the planetesimal grows, various heat sources can trigger it to warm-up: a strong solar wind during an early phase in the formation of the Sun; the radioactive decay of Aluminum-26, possibly injected into the nascent Solar System by a nearby supernova; impacts (Binzel et al. 1991). This heat can cause the interior to melt partially or completely. Once melting occurs, differentiation, or the sorting into layers, begins. In the molten state, materials can move more freely, allowing denser materials, mainly metals like iron and nickel, to sink towards the center, forming a core, while lighter silicate materials rise to the surface, forming a mantle and crust. Over time, the asteroid cools and solidifies, preserving the differentiated structure of core, mantle, and crust.

Undifferentiated asteroids, also referred to as primitive or homogeneous asteroids, have not experienced significant internal heating and melting, and thus have not undergone differentiation. They formed through the accretion of dust and small rocky fragments in the early Solar

System. These bodies did not accumulate sufficient heat to cause melting, so they consist mainly of a homogeneous mixture of various minerals and materials. Their composition closely resembles that of the primordial solar nebula from which they originated.

Following is a more detailed description of undifferentiated and differentiated asteroids (Council 1998):

Undifferentiated, primitive (C-type) asteroids According to meteoritic evidence, C-type asteroids formed from dust with a chemical composition similar to that of average protosolar system material for non-volatile elements, plus volatile substances like water ice, possibly other ices, and organic matter (Bunch & Chang 1980). Studies of carbonaceous chondrites indicate that some C-type asteroids experienced heating beyond the melting point of water ice shortly after their formation (Zolensky & McSween 1988). Although the resultant liquid water might have eventually vaporized into space, it persisted long enough in larger asteroids to generate a secondary, hydrated lithology from an initially anhydrous mixture of silicates, oxides, sulfides, and metals (Zolensky & McSween 1988). This liquid water also reacted with the initial organic matter, resulting in the secondary organic compounds found in carbonaceous chondrites today (Kerridge 1993).

Undifferentiated, metamorphosed asteroids Undifferentiated, metamorphosed asteroids were heated to temperatures below 1000 K, preventing differentiation but also leading to dehydration (if they were ever hydrated) and creating conditions unsuitable for biological materials. The most prevalent meteorites on Earth, known as ordinary chondrites, are fragments from such asteroids. These meteorites are identified as undifferentiated because their bulk elemental compositions³ are similar to the non-volatile elements of the Solar System (e.g. Wasson 1985).

Differentiated asteroids Differentiated asteroids, or fragments of them, were heated enough to undergo partial melting and differentiation. Vesta is an example of a mostly intact differentiated body. Its surface is covered with basalts (McCord et al. 1970). It is presumed (and partially confirmed by observations Binzel et al. (1997)) that a basaltic crust lies on top of an olivine mantle on Vesta, which likely also has an iron core. The various types of metallic, stony-iron, and achondritic stony meteorites are generally believed to originate from these differentiated asteroids or analogous ones, typically located in the inner to middle asteroid belt. These materials have been exposed to long-term heating well above 1000 K, in the absence of water.

Bell (1986) divided the asteroids into three superclasses based on their compositions and locations within the asteroid belt (Fig. 1.5):

1. Primitive asteroids include classes C, D, P, and are located in the outer asteroid belt;
2. Metamorphic asteroids include classes F, G, B, T, and are located in the central asteroid belt;
3. Igneous asteroids include classes S, M, E, and are located in the inner asteroid belt.

³Bulk composition refers to the overall composition of object, averaged over its entire mass.

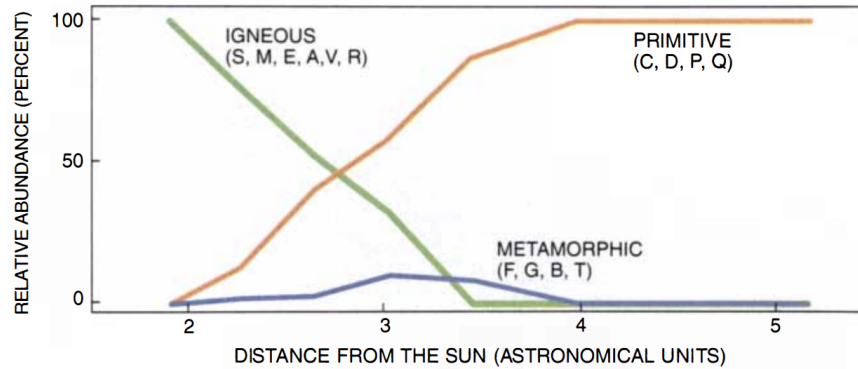


Figure 1.5: Distribution of the three superclasses of asteroids. Credit: Binzel et al. (1991).

The distribution pattern indicates that the primordial warm-up process likely created a steep temperature gradient, that altered the composition of the asteroids. Primitive asteroids, situated farthest from the Sun, are predominantly rich in carbon and water, representing unaltered remnants from the formation of the Solar System. Metamorphic asteroids, which are similar to primitive asteroids but contain fewer volatile compounds and little water, suggest that some heating process transformed certain primitive asteroids into metamorphic ones. Igneous asteroids, located closest to the Sun, appear to have undergone significant heating (Binzel et al. 1991).

Meteorites

When fragments of asteroids enter the atmosphere of the Earth and survive the passage to reach the surface, they are known as meteorites. Studying meteorites allows scientists to analyze the composition of asteroids without having to leave Earth, providing valuable information about the early Solar System.

Meteorites are categorized into three types (Spohn 2011; Burbine 2016):

Stony meteorites are composed mainly of silicates. They are divided into chondrites and achondrites (Krot et al. 2003). Chondrites contain chondrules, spherical bodies formed in the early Solar System, that together with small mineral grains aggregated to form asteroids. Achondrites lack chondrules and have undergone processes such as melting and differentiation. Some formed on asteroids, others on Mars (SNC meteorites (Makishima 2017): shergottites, nakhlites, and chassignites) and the Moon.

Stony-iron meteorites are composed of roughly equal parts metal and silicate. They have undergone differentiation.

Iron meteorites are composed mainly of iron. They represent core fragments of asteroids. Iron meteorites exhibit a distinctive Widmanstätten pattern, a series of geometric bands that arise from the slow cooling of iron-nickel minerals in the core of the asteroid (Burbine et al. 2002; Yang et al. 2007).

Chondrites, the more primitive type, are generally believed to contain organic materials. This contrasts with achondrites, which originate from parent bodies that underwent significant melting and differentiation into silicate mantles and iron cores. There is evidence suggesting that most chondrites accreted water, likely as ice, during their formation (Alexander 2011). Chon-

drites consist of three main components: calcium-aluminum-rich inclusions (CAIs), silicate-rich spherical chondrules (0.1 mm - a few centimeters (Makishima 2017)), and matrix (Woitke et al. 2024). CAIs are thought to have formed in the early Solar System (Connelly et al. 2012). Both CAIs and chondrules are high-temperature objects (1400°C - 1800°C) that formed within the solar nebula. Due to the high formation temperatures of inclusions and chondrules, organic matter could not have survived. Therefore, organic matter is expected to be found only in the matrix that binds the meteorite components together (Alexander 2011). The matrix is primarily composed of olivine, pyroxene, and Fe-Ni metals, which were formed by transient heating and rapid cooling approximately 2 - 4 Myr after the CAIs originated (Woitke et al. 2024). Additionally, sulfides, sulfates, carbonates, and various other minerals, including significant amounts of phyllosilicates in some meteorites, are also present (Brearley 1989; Buseck & Hua 1993). Based on their compositions and mineralogies, chondrites are classified into: ordinary, carbonaceous, and enstatite (Alexander 2011). Enstatite chondrites contain plagioclase, enstatite, high-calcium pyroxene, and sulfides (Taylor & Scott 2003). Carbonaceous chondrites are among the most water-rich materials in the inner Solar System (Alexander et al. 2012). They can have a high overall amount of carbon, which is mostly made up of organic matter. Additionally, they contain different types of minerals, such as carbonates, diamonds, silicon carbide, and graphite (Chan & Zolensky 2022). Ordinary chondrites consist of metal, olivine, and pyroxene (Cloutis et al. 2018). Each of these classes is further subdivided (Scott & Krot 2003; Weisberg et al. 2006) into several groups. Ordinary chondrites are categorized into H, L, and LL; carbonaceous chondrites into CI, CM, CR, CV, CO, CB, CH, and CK; and enstatite chondrites into EH and EL. The term carbonaceous chondrite is somewhat misleading, as some ordinary and enstatite chondrites contain more carbon than certain carbonaceous chondrites (Alexander 2011).

Achondrites have a diverse composition, including types like aubrites (with an unknown origin), eucrites (basaltic), diogenites (peridotitic), and howardites (a mixture of eucrites and diogenites). The howardites, eucrites, and diogenites are collectively referred to as HED meteorites, named after the initials of each type. These meteorites are thought to originate from 4 Vesta, a differentiated asteroid that has developed both a core and a mantle (Makishima 2017).

Tholen classification

Tholen's asteroid taxonomy system categorizes asteroids into 14 classes based on their spectral properties (Tholen 1984; Tholen & Barucci 1989). An additional class, K, was later introduced to the taxonomy by Bell (1988, 1989) after observing the family Eos, and two other classes, J and O, were introduced by Binzel & Xu (1993); Binzel et al. (1993); Xu et al. (1995) after observing small asteroids in the main belt (Bus & Binzel 2002).

These classes are categorized into three groups based on their albedo⁴:

Low albedo classes (< 0.1)

- **Class C:** Similar in surface composition to some types of carbonaceous chondrites (CI and CM). Subclasses are B, F, and G.
- **Class D:** Predominantly Trojan asteroids with a reddish color, possibly due to kerogen-like materials. No known meteorite analogs.

⁴<https://www.castfvg.it/Elidoro%20Claudio/Geocities/index.html>.

- **Class P:** Common near the outer parts of the main belt, likely rich in carbon. No known meteorite analogs.
- **Class T:** Rare, with unknown composition, possibly highly altered carbonaceous chondrites.
- **Class K:** Possible progenitors of CV and CO chondrites.

Moderate albedo classes

- **Class A:** Rare, with very red spectra and infrared absorption features indicative of olivine, possibly similar to brachinites.
- **Class M:** Likely composed of Fe-Ni metal, similar to metallic meteorites.
- **Class Q:** Includes asteroid 1862 Apollo, these asteroids might be potential progenitors of ordinary chondrites.
- **Class R:** The sole member is asteroid 349 Dembowska, with an olivine and pyroxene surface and some metals, analogous to olivine-rich achondrites.
- **Class S:** Consists of varying proportions of metals, olivine, and pyroxene. It is often associated with ordinary chondrites, and possibly related to asteroids like Itokawa (Tsuchiyama 2014).
- **Class V:** Includes 4 Vesta, these asteroids are characterized by strong pyroxene features, similar to basaltic achondrites.

High albedo classes (> 0.3)

- **Class E:** Rare, possibly similar to enstatite chondrites.

Key classes that are significant due to their composition (Barucci et al. 1987) and location within the asteroid belt include⁵:

- class C, these asteroids are rich in carbon and are predominantly found in the outer regions of the asteroid belt;
- class S, composed primarily of metallic iron, as well as iron- and magnesium-silicates, these asteroids are commonly located in the inner regions of the asteroid belt;
- class M, with a composition largely consisting of metallic iron, these asteroids are typically found in the middle regions of the asteroid belt.

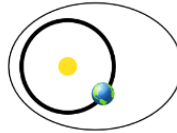
⁵<https://nssdc.gsfc.nasa.gov/planetary/text/asteroids.txt>.

1.1.2 Near Earth Objects

NEOs are defined as asteroids and comets with a perihelion distance $q < 1.3$ AU. Within this category, asteroids are referred to as Near Earth Asteroids (NEAs), and comets are known as Near Earth Comets (NECs). The majority of NEOs are asteroids. NEAs are further divided into groups (Atira, Aten, Apollo, and Amor) based on their perihelion distance, aphelion distance (Q), and their semimajor axes (a) (Fig. 1.6). Potentially Hazardous Asteroids (PHAs) are determined by specific criteria that evaluate their potential to make dangerously close approaches to Earth. In particular, asteroids with an Earth Minimum Orbit Intersection Distance (MOID) of 0.05 AU or less, and an absolute magnitude (H) of 22.0 or less are classified as PHAs (Harris & D'Abramo 2015). NEOs have chaotic orbits, almost unpredictable over decades. For this reason, various projects monitor them continuously (Tommei 2019, 2021).

Amors

Earth-approaching NEAs with orbits exterior to Earth's but interior to Mars' (named after asteroid (1221) Amor)



$$a > 1.0 \text{ AU}$$

$$1.017 \text{ AU} < q < 1.3 \text{ AU}$$

Apollos

Earth-crossing NEAs with semi-major axes larger than Earth's (named after asteroid (1862) Apollo)



$$a > 1.0 \text{ AU}$$

$$q < 1.017 \text{ AU}$$

Atens

Earth-crossing NEAs with semi-major axes smaller than Earth's (named after asteroid (2062) Aten)



$$a < 1.0 \text{ AU}$$

$$Q > 0.983 \text{ AU}$$

Atiras

NEAs whose orbits are contained entirely within the orbit of the Earth (named after asteroid (163693) Atira)



$$a < 1.0 \text{ AU}$$

$$Q < 0.983 \text{ AU}$$

Figure 1.6: NEA groups. Credit: NASA/JPL-Caltech.

1.1.3 Comets

Comets are pristine remnants from the formation of the outer Solar System 4.6 Gyr ago. These celestial bodies are divided into two main groups: the long-period Oort/Öpik cloud comets (OCCs, Oort Cloud Comets), consisting of comets with random orbital inclinations and aphelia located in the outer reaches of the gravitational influence of the Sun; and the short-period Kuiper/Edgeworth Belt comets, consisting of comets with low-inclination orbits that enter the inner Solar System through random gravitational interactions with the giant planets. The first objects to form in the outer protosolar nebula were cometsimals, which served as the building blocks for comets and planets. Comets that remained beyond the orbit of Neptune formed the Kuiper Belt. Those forming near the giant planets experienced one of three fates: accretion onto a giant planet, ejection from the Solar System on a hyperbolic trajectory, or capture at the edge of the Solar System within the Oort/Öpik cloud. As a result, these comets have been preserved in the cold, distant reaches of space for 4.6 Gyr years, only to be randomly scattered into the inner Solar System later (Combi et al. 2002).

The Oort Cloud is a spherical shell composed of icy bodies surrounding the Solar System. It may contain 10^{12} comets. It extends from 20000 up to 200000 AU from the Sun (Oort 1950; Hills 1981; Spohn 2011). By the influence of stars and giant molecular clouds passing near the Sun, OCCs are ejected into the inner Solar System as long-period comets (Mazeeva 2004). These comets have highly eccentric orbits (Moore 2005). In contrast, short-period comets orbit close to the plane of the ecliptic. These comets are believed to originate from the Kuiper Belt (between 30 and 55 AU) or the scattered disk, a dynamic zone formed by the interactions with Neptune during the early stages of planet formation that contains many icy objects with eccentric orbits (Duncan & Levison 1997; Delsemme 1998; Duncan et al. 2004; Spohn 2011).

Figure 1.7: Comet C/1995 O1 Hale-Bopp, on March 14, 1997. On this photo obtained with a telelens, the dust tail fans out to the right, while the bright, well separated blue ion tail is pointing straight away from the Sun. Credit: ESO/E. Slawik.

Whipple's model describes comets as dirty snowballs. According to this model, a comet is composed of a mixture of volatile ices (such as water, carbon dioxide, methane, and ammonia) and dust particles. When a comet approaches the Sun, the heat causes the ices to sublimate, transitioning directly from a solid to a gas. This process releases gases and dust, forming a glowing coma around the solid nucleus. The outflowing gases also drag dust away from the nucleus, creating the distinct tails of the comet (Whipple 1950). Typically, a comet shows two tails: the blue plasma tail and the red dust tail, also known as the Type 1 (ion) tail and Type 2 (dust) tail (Fig. 1.7). The plasma tail results from the interaction between the solar wind and the cometary plasma, whereas the dust tail is formed due to the pressure of solar radiation acting on the cometary dust (Saito et al. 1994). Solar radiation pressure acts on the dust to create long, curved dust tails along the path of the comet, while the ionization of gases and their interaction with the solar wind forms the long, straight ion tails (Combi et al. 2002).

Short- and long-period comets

According to models of Solar System formation, long-period comets originated in the region of the giant planets (between Jupiter and Neptune) before being ejected to the Oort Cloud by these planets (Meech & Svoren 2004; Rickman 2010; A'Hearn et al. 2012). Consequently, long-period comets are likely the least altered and contaminated objects since the formation of the Solar System. Everhart (1972) showed that long-period comets could be captured into short-period orbits if they lost energy through repeated encounters with Jupiter, particularly when they had small inclinations and perihelion distances near the orbit of Jupiter. However, Joss (1973) found that this capture process was too inefficient to explain the observed number of short-period comets. This led Fernandez (1980) to investigate the idea that a "comet belt beyond Neptune" could be the source. Long-period comets have orbital periods larger than 200 years.

Short-period comets orbit around the Sun in 200 years or less. Comet Halley is an example, which completes its orbit roughly every 76 years. Comets that complete an orbit in less than 20 years are referred to as Jupiter-Family Comets (JFCs). Their trajectories usually remain close to the planetary ecliptic plane and have their aphelia near the orbit of Jupiter. Their paths are frequently influenced by the gravitational forces of Jupiter and other planets. Comets with orbital periods ranging from 20 to 200 years are known as Halley-type comets. These comets orbit the Sun between the paths of Jupiter and Pluto and can approach at angles ranging from 0° to 90° relative to the planetary plane. Not all comets follow periodic orbits. Non-periodic comets possess parabolic or hyperbolic orbits, orbiting the Sun only once in their lifetimes. Furthermore, certain comets, known as interstellar comets or exocomets, originate from extrasolar systems, meaning that they were formed around stars other than the Sun. The only observed examples of this include 1I/'Oumuamua and 2I/Borisov, which entered our Solar System in 2017 and 2019, respectively (Moore 2005; Spohn 2011).

Orbital elements

The orbit of a small Solar System body, such as a comet or asteroid, can be described using two types of orbital elements: osculating elements and mean elements. Osculating elements describe the orbit calculated from the position and velocity vectors of the body at a specific instant. These elements represent the state of the orbit at that moment, but changes over time due to gravitational perturbations (Burbine 2016). Mean orbital elements, on the other hand, describe the average orbit of a comet over a longer period of time. Unlike the osculating elements, which are constantly changing due to perturbations, the mean elements provide a simplified representation of the orbit of the comet by averaging out these variations over time.

The key orbital elements that define the shape and orientation of the orbit (Fig. 1.8) are as follows (Spohn 2011; Burbine 2016; Wood 2019):

- Semimajor axis (a): Half of the major diameter of the elliptical orbit of the comet.
- Eccentricity (e): A measure of the shape of the orbit of the comet, where values can be: $e = 0$ for circular orbit, $e = 1$ for parabolic orbit, and $e > 1$ for hyperbolic orbit.
- Inclination (i): The angle between the reference plane (ecliptic plane, which is the plane of the orbit of the Earth) and the plane of the orbit of the comet.
- Longitude of the ascending node (Ω): The angle measured counterclockwise from the reference direction (vernal equinox) to the point where the comet crosses the ecliptic plane from south to north (ascending node; the line of intersection between the comet orbit plane and the ecliptic plane is called the line of nodes).
- Argument of perihelion (ω): The angle between the ascending node and the perihelion of the orbit.
- True anomaly (ν): The angle of the comet from the direction of perihelion and its current position.

Other frequently used elements that describe the orbit of a comet are equivalent to the ones listed above, and can be used as alternatives to characterize its orbit:

- Perihelion distance (q): The closest distance between the comet and the Sun.
- Aphelion distance (Q): The farthest distance between the comet and the Sun.
- Date of perihelion: The specific date when the comet reaches its perihelion, converted to a decimal Julian date.

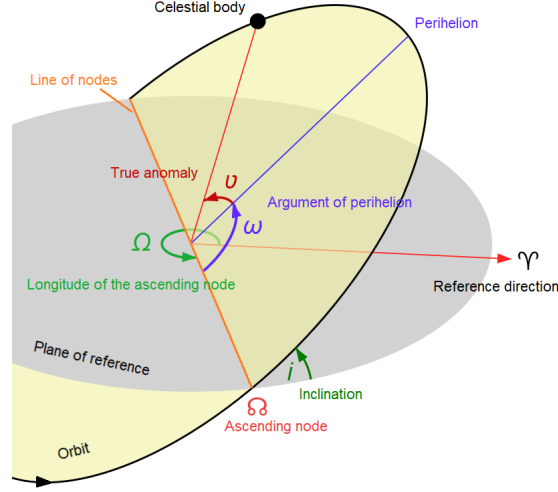


Figure 1.8: Orbital parameters. Modified image from: Wikimedia Commons, by Lasunncty. Licensed under the Creative Commons Attribution-Share Alike 3.0 Unported license.

The Tisserand parameter

The Tisserand parameter is a dynamical quantity that remains nearly constant during an encounter between a comet or an asteroid and a planet. Hence, it is used to identify comets and asteroids. Jupiter, being the most massive planet in the Solar System, exerts the strongest dynamical influence on comets and asteroids. Therefore, the Tisserand parameter most commonly referenced is the one calculated with respect to Jupiter, denoted as T_J (Eq. 1.1) (Tisserand 1891; Kresak 1982; Kosai 1992; Carusi et al. 1995; Jewitt 2012; Haranas et al. 2023).

$$T_J = \frac{a_J}{a} + 2 \left[(1 - e^2) \frac{a}{a_J} \right]^{1/2} \cos(i), \quad (1.1)$$

where a , e and i are the semimajor axis, the eccentricity and the inclination of the orbit of the comet or asteroid, respectively, and $a_J = 5.2$ AU is the semimajor axis of the orbit of Jupiter.

The Tisserand parameter is computed in a circular restricted three-body system, where one of the masses is assumed to be negligible (the one of the comet). The other two masses (the primary one, mass of the Sun, being larger than the secondary one, mass of Jupiter) orbit their common barycenter in fixed circular orbits (Szebehely 1967).

According to Carusi et al. (1987), comets with $T_J < 2$ are Halley-type comets, comets with $T_J > 2$ are Jupiter family comets. Levison (1996) gives instead the following definition. Comets with a $T_J > 2$ are classified as ecliptic comets and tend to have small inclinations. In contrast, those with $T_J < 2$ are predominantly sourced from the Oort Cloud. Ecliptic comets are further subdivided into three distinct groups:

- Comets with $2 < T_J < 3$ are on Jupiter-crossing orbits and are referred to as JFCs.
- Comets with $T_J > 3$ and $a < a_J$ are categorized as Encke-type comets. Objects in this group may resemble asteroids, as $T_J > 3$ is also a defining characteristic of asteroids.
- Comets with $T_J > 3$ and $a > a_J$ are known as Chiron-type comets.

Volatile ices

Our current understanding of the composition of cometary nuclear ices is predominantly derived from the study of the coma. Direct examination of the ices on the nucleus surface is feasible only via spacecraft (Bockelée-Morvan & Biver 2017). Near-infrared spectra of cometary surfaces detected the spectral signatures of water ice (Sunshine et al. 2007; Filacchione et al. 2016), CO₂ ice (Filacchione et al. 2016), and a semi-volatile organic material containing the carboxyl (COOH) group (Quirico et al. 2016). Analyses of cometary atmospheres reveal that the principal constituents of cometary nuclear ices, ordered by their relative abundances, are water, CO₂, CO, CH₃OH, CH₄, H₂S, and NH₃ (Bockelée-Morvan et al. 2004; Bockelée-Morvan & Biver 2017). According to Biver & Bockelée-Morvan (2015), the molecular abundance data indicates that the composition distribution of OCCs and JFCs is generally similar, with the exception of CO, which is observed in lower abundance in all observed JFCs. This finding is consistent with the Nice model, which suggests that both the Oort Cloud and the scattered disk were populated with comets formed in the same regions of the Solar System (Brasser & Morbidelli 2013). Dello Russo et al. (2016) report an overall depletion of volatiles in JFCs compared to OCCs. This depletion is most notable for C₂H₂, C₂H₆, CH₄, and CO. It might be a primordial characteristic (A'Hearn et al. 1995) or influenced by evolutionary processes after formation. One possible explanation is that the most volatile species were lost over time due to multiple perihelion passages in JFCs (Dello Russo et al. 2016).

H₂O ices begin to sublimate when a comet approaches within approximately 3 AU of the Sun in the inner Solar System, due to the relatively high sublimation temperature of H₂O, around 150 K (Yamamoto 1985; Womack et al. 2017). Some comets show activity at distances greater than 3 AU (Whitney 1955; Roemer 1962; Meech & Jewitt 1987; Hughes 1991; Sekanina et al. 1992). Water ice sublimation can still induce some activity at these distances if it is triggered by impacts, tidal disruptions caused by the interactions with massive planets, and interactions with solar flares and solar wind erosion (Strazzulla et al. 1983; Stern 1995; Sekanina et al. 1994; Boss 1994). However, these potential triggers for water ice sublimation are unlikely to account for the extended periods of activity observed in most distantly active comets (Mumma et al. 1993). Therefore, it is more plausible that most comets active beyond 3 AU have comae produced by volatiles other than water. Fig. 1.9 provides a list of sublimation temperatures for various cometary volatiles (Womack et al. 2017). For instance, CO, which has a low sublimation temperature (around 20 – 30 K), starts to sublimate at high distances from the Sun (> 35 AU; Womack et al. 2017), where H₂O remains frozen in the nucleus of the comet. Consequently, a high CO/H₂O production rate ratio greater than one is observed when comets are at large distances (≥ 3 AU) from the Sun, where the radiation field and nucleus temperatures are expected to be low (Ootsubo et al. 2012; Marboeuf & Schmitt 2014; Womack et al. 2017; Cordiner et al. 2022; Żółtowski et al. 2023).

Species	Temperature (K)
N ₂	22
CO	25
CH ₄	31
H ₂ S	57
C ₂ H ₂	57
H ₂ CO	64
CO ₂	72
HC ₃ N	74
NH ₃	78
CS ₂	78
SO ₂	83
CH ₃ CN	91
HCN	95
CH ₃ OH	99
H ₂ O	152

Figure 1.9: Sublimation temperatures of cometary volatiles (Yamamoto 1985; Sekanina 1996). Credit: Womack et al. (2017).

1.1.4 TransNeptunian Objects

TNOs are a broad category of small Solar System bodies that orbit the Sun at distances greater than Neptune. These objects display a variety of orbital characteristics and are classified into several distinct populations based on their specific orbits. The first major grouping is known as the classical Kuiper Belt, consisting of objects in near-circular orbits with semimajor axes around 45 AU. These orbits remain stable against the gravitational influence of Neptune over the lifetime of the Solar System. Another significant population is the Plutinos, named after Pluto. These objects are in a 2:3 orbital resonance with Neptune, meaning they complete two orbits around the Sun for every three orbits completed by Neptune. Both the classical Kuiper Belt objects and Plutinos are collectively referred to as Kuiper Belt Objects (KBOs). A third population is known as scattered disk objects. These bodies have highly eccentric orbits with perihelia generally within the classical Kuiper Belt, although some are inside the orbit of Neptune. Their aphelia extend far beyond, a result of dynamic interactions with Neptune (Cruikshank et al. 2007). The last group is the detached objects with orbits at large eccentricities, and with perihelion distances out of the influence of Neptune. All these objects are encompassed by the term trans-Neptunian objects. Furthermore, an additional class, known as Centaurs, can be linked to the TNO population. They have unstable orbits that lie between those of Jupiter and Neptune. It is likely that planetary perturbations and mutual collisions within the Kuiper Belt have resulted in the ejection of these objects into Centaur orbits (Barucci et al. 2010).

1.2 Active asteroids

Active asteroids (Fig. 1.10) are transitional objects between comets and asteroids. They exhibit comet-like dust emissions while maintaining asteroid-like orbits, which are defined by a Tisserand parameter with respect to Jupiter, $T_J \gtrsim 3$, and are located within the orbit of Jupiter. A subgroup of active asteroids is the main-belt comets (MBCs) (Jewitt et al. 2015; Hsieh & Sheppard 2015), which exhibit dust emission driven by ice sublimation (Hsieh et al. 2012a; Jewitt et al. 2015). The other subgroup of active asteroids is the non-sublimation-driven active asteroids, which produce dust emissions as a result of collisions (Jewitt et al. 2011; Bodewits et al. 2011; Ishiguro et al. 2011; Kim et al. 2017a,b) or rotational destabilization (Jewitt et al. 2013, 2014a; Drahus et al. 2015; Sheppard & Trujillo 2015). MBCs are typically identified by the specific temporal behavior of their activity, which occurs near perihelion, persists for a minimum of several weeks, and recurs during consecutive perihelion passes. In contrast, non-MBC active asteroids can initiate activity at any true anomaly and may exhibit single-time events, although they are not limited to such occurrences.

The James Webb Space Telescope (JWST) currently has the sensitivity to detect spectroscopic signatures of water vapor near an MBC. The first such detection was noted in 238P/Read (hereafter 238P) (Kelley et al. 2023). This marked the inaugural detection of water outgassing from a main-belt object that also exhibits visible dust emissions. In comparison, Küppers et al. (2014) previously identified water vapor plumes from Ceres, but without associated dust emissions. In the absence of spectroscopic evidence, the repeated and extended dust emissions from MBCs near perihelion are considered strong indicators of sublimation, as this behavior is challenging to attribute to other mechanisms (Hsieh et al. 2008, 2011, 2012a,b; Hsieh 2015; Moreno et al. 2011, 2013; Jewitt et al. 2014b; Pozuelos et al. 2015).

Numerical thermal models confirm that primordial water ice can survive in main-belt objects over Gyr timescales only if it is buried under a protective dusty layer (Fanale & Salvail 1989; Schorghofer 2008, 2016; Prialnik & Rosenberg 2009; Schörghofer & Hsieh 2018). Consequently, MBC activity requires events like collisions to expose the buried ice to solar irradiation (Haghighipour et al. 2016, 2018). The resulting sublimation of these freshly exposed materials then drives the dust emission (Hsieh et al. 2004; Hsieh & Jewitt 2006). Notably, even without direct ice exposure, reducing the thickness of the dust layer at the bottom of a crater can be sufficient for the underlying ice to sublimate (Capria et al. 2012). Rapid rotation may also initiate or sustain dust emissions against gravity. For instance, the activity of 133P/Elst-Pizarro, the first discovered MBC, could involve a combination of an initial collision, ongoing sublimation, and rapid rotation (Hsieh et al. 2004, 2010; Hsieh 2015; Jewitt et al. 2014b). The peak activity for MBCs typically occurs after perihelion. This delay in the sublimation process may be a result of the time required for the thermal wave to penetrate the surface and reach the ice buried beneath (Hsieh 2015).

Hsieh et al. (2018a) presented the evolution of activity during active periods of two MBCs, 238P and 288P/(300163) 2006 VW139 (hereafter 288P). Activity declined over the years for 238P, while it increased for 288P. A decrease in activity after each perihelion passage can be attributed to several factors that influence the sublimation and surface conditions of these bodies over time. One plausible explanation for the observed decrease in activity from one perihelion passage to the next is the gradual formation of a dry mantle. Ice-rich MBCs are thought to have a rubble mantle-type crust. Following a triggering event, such as an impact, the freshly exposed ice sublimates, causing the observable comet-like activity. However, over time, dust

particles that are too large to be ejected by gas drag against gravity start accumulating on the surface. This accumulation forms a layer of dust and pebbles that eventually becomes thick enough to act as a protective barrier, burying the ice beneath. Similar processes have been observed in comets (Thiel et al. 1989; Jewitt 1992, 1996), whereas MBCs, discovered more recently in 1996, exhibit analogous behavior. Initially, after the trigger event, the activity in MBCs decreases rapidly as the exposed ice sublimates. Over time, as the rubble mantle thickens sufficiently, the activity diminishes more slowly due to the reduced sublimation of the buried ice (Jewitt 1996; Hsieh et al. 2015, 2018a). This protective layer effectively prevents further sublimation, thereby stabilizing the long-term activity cycles of the MBC. In contrast, increases in activity over time may arise if additional processes, beyond the formation of a dust mantle, significantly influence dust production rates. These processes could include events like sinkhole collapses (Vincent et al. 2015) or landslides triggered by the rotation of the comet or impacts (Steckloff et al. 2016; Hofmann et al. 2017), both of which could expose fresh volatile material. Another possible explanation for enhanced activity is a reduction in perihelion distance, which would lead to increased solar heating and, consequently, higher sublimation rates (Licandro et al. 2000).

Numerical models indicate the dynamical stability of most of the orbits of MBCs, implying these objects formed within the main asteroid belt (Haghighipour 2009; Jewitt et al. 2009; Hsieh et al. 2012a,b), remaining dormant until recent activation (Hsieh et al. 2004; Capria et al. 2012). The collisional breakup of larger parent bodies may also lead to the activation of MBCs by exposing the sub-surface ice (Hsieh et al. 2018c). Conversely, some MBCs exhibit orbital instability over timescales of 20-30 Myr, implying potential relocations due to interactions with the giant planets (Haghighipour 2009; Jewitt et al. 2009). Furthermore, some MBCs might have originated from the outer Solar System and were subsequently captured within the main asteroid belt (Haghighipour 2009; Hsieh & Haghighipour 2016; Kim et al. 2022).

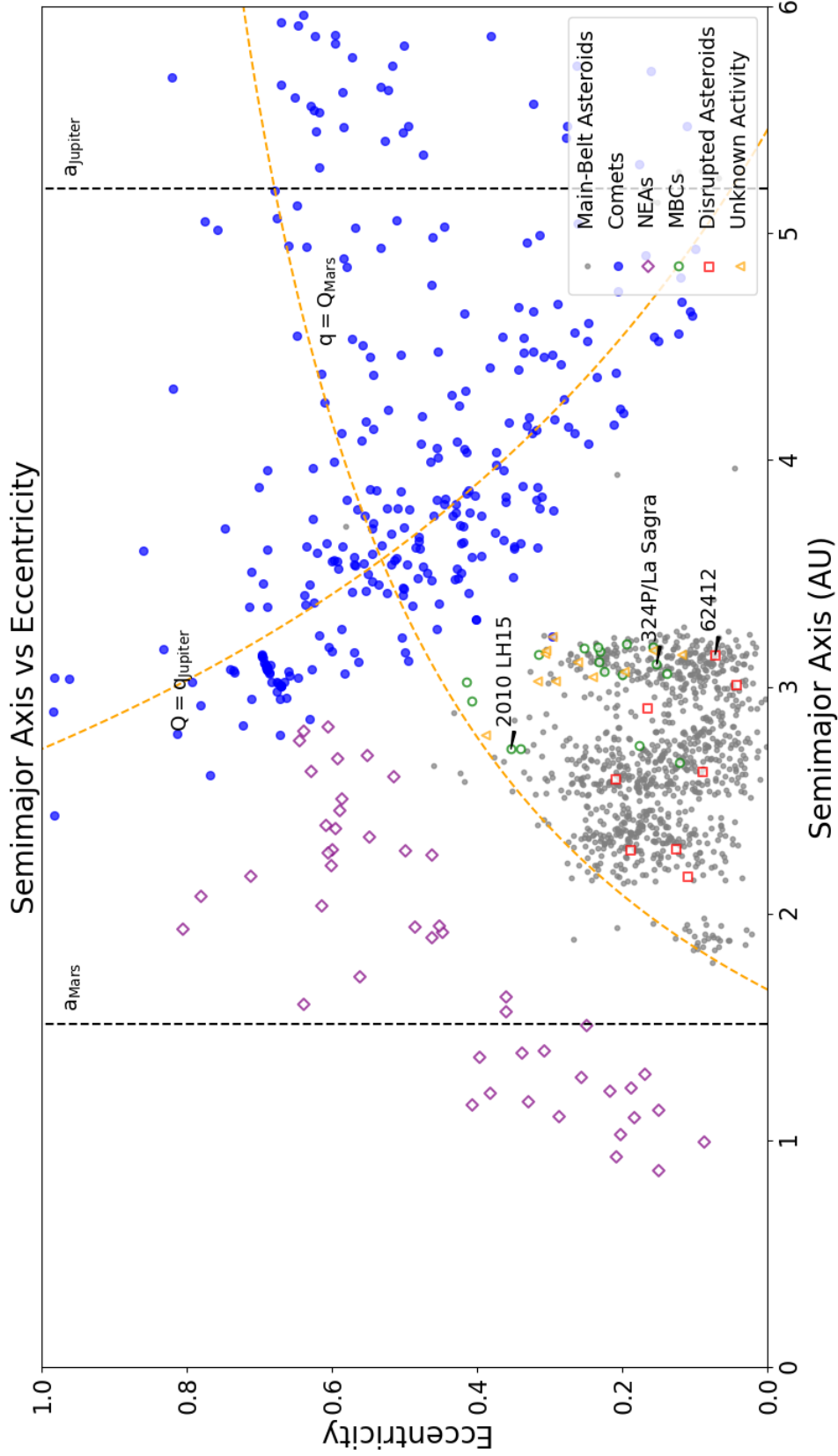


Figure 1.10: Eccentricity vs. semimajor axis for main-belt asteroids (small gray dots), comets (blue filled circles), NEAs (white diamonds with purple edges), MBCs (white circles with green edges), disrupted asteroids (white squares with red edges), and active asteroids with unknown activity mechanisms (white triangles with orange edges). Objects above the orange diagonal curves cross either the aphelion distance of Mars or the perihelion distance of Jupiter, as marked. The semimajor axes of the orbits of Mars and Jupiter are marked. The MBCs 324P/La Sagra and 2010 LH15, and the disrupted asteroid 62412, which are the focus of this thesis, are marked with arrows.

1.2.1 Activity processes

These are the processes that can activate active asteroids (Jewitt 2012):

Sublimation Sublimation occurs when volatile ices (e.g. water, carbon dioxide, carbon monoxide) within an asteroid are heated by the Sun and transition directly from a solid to a gas, creating jets of gas and dust. To start the sublimation process, the protective dusty layer must be removed, which can occur as a result of impacts.

Impact ejection Impact ejection happens when an asteroid is hit by another celestial body. The energy from the collision can eject dust and debris from the surface, creating a temporary or sustained active state.

Rotational instability When the rotation rate of an asteroid increases—potentially due to the YORP effect (Marzari et al. 2011; Jacobson & Scheeres 2011) or to collisions between asteroids—it can reach a critical speed at which it begins to shed surface material. This can lead to a breakup or significant release of dust and debris (cf. Drahus et al. 2011).

Electrostatic forces Electrostatic forces can become significant in the microgravity environments found on asteroids. Solar radiation can charge the surface particles, causing them to become like-charged (either all positively or all negatively charged). These like-charged particles repel each other, a process known as electrostatic levitation, and can lift off the surface, mobilizing dust particles and creating activity. However, there are major uncertainties about electrostatic effects, particularly concerning the tendency of small particles to stick to each other and surfaces due to Van der Waals and other contact forces. These uncertainties are critical for asteroids because, unless cohesive forces can be overcome, electrostatic levitation and ejection will not occur (Hartzell & Scheeres 2011). Despite this, features on some asteroids, such as the flat, pond-like structures seen on Eros, suggest that electrostatic ejection might play a role (Hughes et al. 2008). Additionally, the detection of ultra-faint comae in approximately 5% of main-belt asteroids (Sonnnett et al. 2011) could indicate that electrostatic forces are significant in the ejection of sub-micron grains independently of the distance of the asteroid from the Sun. Sonnnett et al. (2011) investigated nearly 1000 asteroids as part of the Thousand Asteroid Light Curve Survey (TALCS). To search for comae, they used a coma detection algorithm that fit a detailed point spread function (PSF) model to each candidate object, which included both a point-like (asteroid) and coma-like PSF component. By measuring the fractional contribution of the coma and comparing it to a control sample with null detections of similar brightness and motion, they identified ultra-faint comae in about 5% of the targets.

Thermal fracture Thermal fracture occurs when repeated cycles of heating and cooling (e.g. from day-night cycles) cause stress that surpasses the tensile strength⁶ of the material within the surface materials of an asteroid, leading to cracking and fragmentation. These small fragments can be mobilized, and small particles can be ejected. Thermal fracture can happen only in asteroids that come very close to the Sun.

Thermal dehydration Thermal dehydration refers to the process where water bound in hydrated minerals, contained in some carbonaceous chondrites (Jarosewich 1990), is released due to high temperatures. This release of water can lead to outgassing and the ejection of small grains. However, the temperatures needed for thermal dehydration are much higher than those typically found in the asteroid belt. Therefore, thermal dehydration is unlikely to play a significant role in most active asteroids, as they usually do not get close enough to the Sun to reach the necessary temperatures.

⁶Tensile strength refers to the maximum stress that a material can withstand while being stretched or pulled before breaking (Kar 2022).

Shock dehydration Shock dehydration happens when an asteroid experiences a high-energy impact. The rapid energy release can cause the release of water. This gas release might be misinterpreted as evidence of ice sublimation.

Radiation pressure sweeping Radiation pressure from sunlight can move small particles away from the surface of an asteroid. The principal limitation of radiation pressure sweeping is the contact forces that hold small particles to the surface of the asteroid. If these forces can be overcome, radiation pressure sweeping can effectively mobilize particles from asteroids that are 10 km in size or smaller.

1.3 The main-belt comet 324P/La Sagra

The MBC 324P/La Sagra (also referred to as P/2010 R2, hereafter 324P) was first identified in 2010 September (Nomen et al. 2010). It reached perihelion on 2010 June 25, 2015 November 30, and 2021 May 6 (UT). The continuous dust emission and mass loss observed during these three perihelion passages indicate that sublimation is the driving cause of its activity (Moreno et al. 2011; Hsieh et al. 2012b; Bauer et al. 2012; Hsieh & Sheppard 2015; Mastropietro et al. 2022, 2023, 2024a).

324P is located in the outer main belt with a semimajor axis of $a = 3.095$ AU, an eccentricity of $e = 0.154$ (see Fig. 1.10), an inclination with respect to the ecliptic of $i = 21.402^\circ$, a perihelion distance of $q = 2.619$ AU, an aphelion distance $Q = 3.570$ AU, an orbital period $P = 5.448$ yr, and a Tisserand parameter relative to Jupiter of $T_J = 3.100^7$. It is dynamically linked to the Alauda family, meaning that it shares similar mean orbital elements (such as semimajor axis, eccentricity, and inclination) with other members of that group of asteroids (Hsieh et al. 2018c). This suggests that 324P and the Alauda family members likely have a common origin, probably resulting from a past collisional event.

Research conducted by Hsieh et al. (2012b) revealed that the brightness of 324P increased by > 1 mag between 2010 August and December, suggesting the ongoing production of dust after perihelion. This observation supported the notion that sublimation is the primary mechanism driving the activity of 324P. Additionally, their numerical simulations indicate that 324P is dynamically stable for > 100 Myr, suggesting that it is likely native to its current location. Using the best-fit IAU phase function with 2013 March data, when 324P was inactive, Hsieh (2014) found an absolute magnitude of $H_R = (18.4 \pm 0.2)$ mag and a slope parameter of $G = 0.17 \pm 0.10$, corresponding to an effective nucleus radius of $r_N = (0.55 \pm 0.05)$ km, assuming a geometric R-band albedo of $p_R = 0.05 \pm 0.02$ for a C-type object. Hsieh et al. (2023) reported slightly different values, with $H_R = 18.38_{-0.17}^{+0.19}$ mag, corresponding to $r_N = 0.59_{-0.10}^{+0.18}$ km ($p_R = 0.05 \pm 0.02$). The classification of 324P as an MBC was reaffirmed by Hsieh & Sheppard (2015) when it reactivated between 2015 March and June. This conclusion was further supported by observations from Jewitt et al. (2016), who found mass loss consistent with sublimation-driven activity near perihelion after analyzing Hubble Space Telescope (HST) data between 2015 September and December. Additionally, Jewitt et al. (2016) noted that the rotation period of 324P is likely greater than 3.8 hours.

During periods of inactivity on 2011 December 23 (Snodgrass et al. 2018) and December 31 (UT), 324P exhibited a faint dust tail (Hsieh 2014). This faint tail is thought to consist of larger particles, which, being less influenced by solar radiation pressure, remain closer to the orbit of

⁷From JPL HORIZONS System, epoch JD 2460053.5 (2023-04-19) Barycentric Dynamical Time (TDB).

the MBC even when inactive. This behavior distinguishes it from other MBCs. Moreno et al. (2011) presented a model of the dust environment of 324P in the period from 2010 October to 2011 January. Their findings indicate that the tails are best simulated by anisotropic ejection models. These models show that dust emission is concentrated near the nucleus south pole, with the obliquity of the spin axis near 90° . This configuration implies a potential for seasonally driven behavior.

The photometry part on 324P, Sect. 3.2, is published in Mastropietro et al. (2024a), while the dust tail analysis part, Sect. 3.3, is only described in this thesis.

1.4 The main-belt comet 2010 LH15

The MBC 2010 LH15 (also referred to as 2010 TJ175, hereafter LH15) was discovered in 2023 in archival Pan-STARRS 1/GigaPixel1 (2010 September 27), Zwicky Transient Facility (ZTF) (2019 August 31) and Dark Energy Camera (DECam) (2019 September 30) data through a Citizen Science project (Chandler et al. 2023). It reached perihelion on 2010 August 13, 2015 February 23, 2019 September 8, and 2024 March 26 (UT). Activity was observed close to its perihelion passages in 2010 and 2019, indicating sublimation-driven processes (Chandler et al. 2023). The 2015 and 2024 perihelion passages were not observed.

It is located in the middle main belt with a semimajor axis of $a = 2.743$ AU, an eccentricity of $e = 0.355$ (see Fig. 1.10), an inclination with respect to the ecliptic of $i = 10.907^\circ$, a perihelion distance of $q = 1.770$ AU, an aphelion distance $Q = 3.718$ AU, an orbital period $P = 4.546$ yr, and a Tisserand parameter relative to Jupiter of $T_J = 3.230^8$. Its perihelion distance of $q = 1.77$ AU is one of the smallest among the known MBCs. It has orbital parameters that are similar to those of the MBC 259P/Garradd ($a = 2.727$ AU, $e = 0.342$, $i = 15.898^\circ$, $T_J = 3.217^9$) (Garradd et al. 2008; Jewitt et al. 2009; Hsieh et al. 2021).

In Table 1.1 are listed the perihelion distances of known MBCs.

The nucleus photometry part on LH15, Sect. 4.2, is published in Mastropietro et al. (2024b).

1.5 The disrupted asteroid 62412 (2000 SY178)

The active asteroid 62412 (2000 SY178) (hereafter 62412) was discovered on 2000 September 28 by LINEAR (Lincoln Near-Earth Asteroid Research) facility at Socorro, New Mexico¹⁰. It is the second-largest active asteroid identified, exceeded in size only by (596) Scheila (Bauer et al. 2012; Sheppard & Trujillo 2015). In 2014, 62412 exhibited a noticeable dust tail (Sheppard & Trujillo 2015), which likely formed after its 2013 perihelion passage, as no tail was observed in images taken about two months before that perihelion. It reached perihelion on 2013 March 21, 2018 October 30, and 2024 July 15 (UT). Based on the near-critical rotation period of 3.33 hours for 62412 and its elongated shape, inferred from the lightcurve amplitude, Sheppard & Trujillo (2015) proposed that the dust activity could have been triggered by either rapid rotation or an impact. The fast spin rate could have contributed to a change in the shape of the asteroid (Sheppard & Trujillo 2015).

⁸From JPL HORIZONS System, epoch 2023-09-13 TDB.

⁹From JPL HORIZONS System, epoch 2011-02-26 TDB.

¹⁰From JPL HORIZONS System, REF: 20030614/Numbers.arc.

62412 has a semimajor axis of $a = 3.153$ AU, an eccentricity of $e = 0.076$ (see Fig. 1.10), an inclination with respect to the ecliptic of $i = 4.707^\circ$, perihelion distance of $q = 2.914$ AU, an aphelion distance $Q = 3.391$ AU, an orbital period $P = 5.598$ yr, and a Tisserand parameter relative to Jupiter of $T_J = 3.198$ ¹¹. It is classified as a C-type asteroid, and located in the outer main asteroid belt as a member of the Hygiea family (Sheppard & Trujillo 2015). These characteristics increase the likelihood of sub-surface ice being present, which could have been exposed during the 2013 event, potentially leading to further sublimation during subsequent perihelion passages, regardless of the initial cause of the activity. While no studies have confirmed whether 62412 reactivated during its 2018 perihelion passage, the lack of observed activity in 2017 and 2019 (Ferrín et al. 2019) suggests that any possible activity was absent.

Table 1.1: Perihelion distances of known MBCs from JPL HORIZONS System. List of MBCs from Ferrellec et al. (2023) and Xin et al. (2024), and Chandler et al. (2023) for LH15.

Name	Perihelion distance (AU)
P/2018 P3 (PANSTARRS) (477P)	1.76
2010 LH15	1.77
233P/La Sagra	1.79
259P/Garradd	1.80
427P/ATLAS	2.18
P/2015 X6 (PANSTARRS)	2.29
P/2020 O1 (Lemmon-PANSTARRS) (457P)	2.33
238P/Read	2.37
433P (2005 QN173)	2.38
313P/Gibbs	2.39
358P/PANSTARRS	2.39
288P (2006 VW139)	2.44
P/2016 J1-A/B (PANSTARRS)	2.45
1 Ceres	2.55
176P/LINEAR	2.58
324P/La Sagra	2.62
P/2021 A5 (PANSTARRS)	2.62
133P/Elst-Pizarro	2.67

¹¹From JPL HORIZONS System, epoch JD 2460600.5 (2024-Oct-17.0) TDB.

1.6 Motivation

MBCs contain near-surface ice, which is presumed to be water ice. This presence is unexpected in these objects since, at the surface temperatures of asteroids located in the main belt, water ice is unstable against sublimation. It survives in the sub-surface, allowing MBCs to have a cometary behavior. Investigating the ice content in MBCs can provide insights into the distribution of volatiles in the early Solar System and help in understanding the formation and subsequent evolution of planetesimals. This understanding is possible through several methods:

- Analyzing the isotopic ratios of MBCs, such as the deuterium-to-hydrogen (D/H) ratio, which can help tracking the origins of their ices and volatiles (Snodgrass et al. 2017).
- Examining the spectral properties of MBCs, which can help in determining the composition of the ices and volatiles. For instance, water detection has been reported in Kelley et al. (2023).
- Developing thermal models for MBCs, which can help in understanding how the ice survives in the sub-surface and to simulate their activity (Capria et al. 2012).
- Developing dynamical models for MBCs, which can help in understanding their origin formations (Haghighipour 2009).
- Future space missions to MBCs, which could deliver direct sample analyses, yielding more details about their composition, structure, and isotopic ratios (Snodgrass et al. 2018).
- Laboratory experiments and simulations examining the behavior of dust and ice under main belt conditions, which can help validate theoretical models and enhance our understanding of their activity (Maindl & Haghighipour 2014; Maindl et al. 2016; Haghighipour et al. 2016; Poch et al. 2023).

The aim of this project is to better understand dust emission from MBCs, to understand present-day water content in the asteroid belt, and to study the strength of water emission by determining the size of the largest debris that the gas drag is able to lift. During their active phases, MBCs eject particles of varying sizes. The larger particles, being less influenced by solar radiation pressure, remain in closer proximity to the nucleus of the comet and disperse into space at a slower rate compared to their smaller counterparts. The sizes of these larger particles can provide valuable insights into the strength of gas drag and the rate of ice sublimation occurring within the comet. Investigating the ice content of MBCs contributes to our understanding of the distribution of volatiles in the early Solar System, as well as the formation and subsequent evolution of planetesimals. However, the presence of smaller particles presents a challenge when measuring larger particles, primarily due to the higher scattering cross section associated with the smaller particles. A principal observational technique for assessing the size of large particles involves analyzing the brightness profile of dust trails during the inactive phases of MBCs. During these periods, when no new dust and gas are being produced, the observation of previously ejected large particles can be conducted more clearly, facilitating more accurate measurements.

In the first part of this project, I conducted a comprehensive analysis of images of the MBC 324P over an extended period from 2010 to 2021. This long-term observational study aimed to understand the evolution of its activity and characterize the properties of the dust it emits. In the second part, I focused on dust modelling on a faint tail of 324P, observed in its inactive

period, to measure the size of the large particles ejected by 324P. This analysis was particularly feasible for 324P due to the notable gap that exists between its nucleus and tail once its activity has ceased, offering a unique opportunity to study the particle dynamics in detail. Additionally, I aimed to investigate the rotational period of 324P, which remains unknown (Hsieh 2014). To achieve this objective, I submitted a proposal for observations with the Gemini North Telescopes, with the goal of measuring its rotational lightcurve profile. While the proposal received approval, technical problems with the mirror of the telescope¹² necessitated a shift in focus. Consequently, I selected an alternate target, LH15, and conducted a study of its inactive nucleus. As a result, the study of the rotational period of 324P will have to be pursued in a future project. In addition to the studies on 324P and LH15, I also submitted a proposal to observe the disrupted asteroid 62412 using the Asiago Mount Ekar telescope. The primary objective of these observations was to investigate whether the asteroid reactivated before its perihelion passage, similar to its activity observed in 2014.

¹²<https://noirlab.edu/public/announcements/ann22030/>.

2 Concepts

2.1 Data reduction

2.1.1 Bias subtraction and flat-fielding

Bias in astronomy refers to the electronic noise and constant offset present in images captured by a camera when no light is entering the sensor. The bias is slightly different for each pixel, and can vary from night to night or during a night. A bias image is an image taken with the shutter closed and zero exposure time. By averaging these frames, a bias correction image is created that represents this constant noise. That combined image will have less random noise than the individual images. This averaged bias frame (masterbias) is then subtracted from the flat-field and science images, effectively removing the noise and allowing for more accurate measurements of the light coming from celestial objects.

The flat-field addresses variations in pixel sensitivity across the imaging sensor and optical artifacts, such as dust on the lens or vignetting¹, which can lead to uneven illumination in images. To create a flat-field image, astronomers capture images of a uniformly illuminated surface, which helps to record any pixel sensitivity variations. Flat-field frames can be twilight flats, where images are taken during the period just after sunset or just before sunrise when the sky is evenly illuminated, or dome flats, which are created by illuminating a smooth surface of the dome with a light source to produce a uniform brightness across the field. The flat-field frames are normalized, averaged, and then corrected by subtracting the masterbias to produce the masterflatfield frame. For the science images, the masterbias is subtracted from the raw images, and the result is divided by the masterflatfield. This process normalizes the pixel responses and corrects for optical imperfections, ensuring uniform brightness across the final image (Pössel 2020).

The following part is described in Mastropietro et al. (2024a).

I conducted bias subtraction and flat-fielding using the following software packages: Dragons (Labrie et al. 2023; Simpson et al. 2024) for data from the Gemini telescopes, Image Reduction and Analysis Facility (IRAF) (Tody 1986, 1993) to process data from the New Technology Telescope (NTT), and EsoRex (Freudling et al. 2013) for data from the Very Large Telescope (VLT). Data from the Panoramic Survey Telescope and Rapid Response System PanSTARRS1 (PS1) were processed by the PS1 Image Processing Pipeline (IPP) (Magnier 2006). Data from the Isaac Newton Telescope (INT) were processed by the INT Wide Field Survey pipeline (Irwin & Lewis 2001). Data from the Canada-France-Hawaii Telescope (CFHT) were processed by the Elixir pipeline (Magnier & Cuillandre 2004). Lowell Discovery Telescope (LDT) and HST data were received in a post-processed state via private communication from Matthew M. Knight and Jewitt et al. (2016), respectively.

For the infrared (IR) data processing, see Sect. 2.1.2.

¹Vignetting is a reduction of the brightness of an image toward the edges compared to the image center.

2.1.2 Photometric calibration

In astronomy, photometric calibration is the process of converting raw data from telescopes and imaging instruments into meaningful measurements of light, which is essential for ensuring that the observed brightness of celestial objects is accurate and consistent across different observations, instruments, and conditions. To establish a reliable photometric system, astronomers compare the known magnitudes of stars in star catalogs, such as PS1 catalog², with the measured brightness of these stars. These stars serve as references for calibrating the observed images.

The zeropoint magnitude represents the sensitivity of the photometric system. It is defined as the magnitude of an object that produces one count per second (Baggett et al. 2002). After observing stars, the zeropoint magnitude can be calculated using the formula:

$$z_p = m_{star} + 2.5 \log_{10}(I/T_{exp}), \quad (2.1)$$

where z_p is the zeropoint magnitude, m_{star} is the known magnitude of the star, I is the object brightness in counts, and T_{exp} is the exposure time.

For the photometric calibration for CFHT and PS1 images, I used the zeropoint magnitudes available in the headers of the images. They were computed by the Elixir and PS1 IPP pipelines, respectively. For PS1 images, I decided to use 8 mmag as an upper limit for the zeropoint errors, based on the statement that the uncertainties from the PS1 Ubercal are less than 9 mmag for the different filters (Finkbeiner et al. 2016). For the images from all other instruments, I performed photometric calibration relative to field stars from the PS1 catalog. I also applied this field star calibration method to the CFHT and PS1 data and verified that my results were consistent.

In the IR domain, data from the Wide-field Infrared Survey Explorer (WISE) were processed and photometrically calibrated by the WSDS PIPELINES (Cutri et al. 2012). To enhance the signal-to-noise ratio S/N, I combined multiple images utilizing the WISE Coadder software³. Data from the Spitzer Space Telescope were processed and calibrated by the Infrared Array Camera (IRAC) pipeline (Fazio et al. 2004; IRAC Instrument and Instrument Support Teams 2021).

In WISE images, the zeropoint magnitudes are included in the header of the images. From the photometry of Spitzer data, I only determined the flux from the object, so the zeropoint magnitude was not necessary for my calculations, as it is only needed to derive the apparent magnitude. However, since IRAF requires a zeropoint magnitude as input, I calculated it myself using (IRAC Instrument and Instrument Support Teams 2021)

$$z_{mag} = 2.5 \log_{10}(F_0/C), \quad (2.2)$$

where z_{mag} is the zeropoint magnitude, F_0 is the zero magnitude flux density in Jy, and C is the conversion factor from MJy sr⁻¹ to μ Jy pixel⁻¹, with $C = 34.983995 \mu$ Jy pixel⁻¹ for both channels. The values of F_0 are (280.9 ± 4.1) for channel 1 and (179.7 ± 2.6) for channel 2. The values I obtained for the zeropoint magnitudes are (17.26 ± 0.02) mag for channel 1, and (16.78 ± 0.02) mag for channel 2.

²<https://catalogs.mast.stsci.edu/panstarrs/>.

³<https://irsa.ipac.caltech.edu/applications/ICORE/>.

2.2 Photometry methods

The following parts are described in Mastropietro et al. (2024a).

2.2.1 Methods for visible light images

I assumed solar colors for the conversions between the different PS1 bands $r-z = 0.5$ and $r-g = -0.62$ (Tonry et al. 2012; Willmer 2018), and between the CFHT filters $r-i = 0.36$ (Gwyn 2012; Willmer 2018), and for the conversion from V-band to R-band $V-R = 0.35$ (Holmberg et al. 2006; Jewitt et al. 2016). Because of color uncertainties, I considered the different r filters (r.00000 for PS1, R for INT, r_G0303 for Gemini North, R#642 for NTT, R_SPECIAL for VLT, r.MP9601 and r.MP9602 for CFHT, R for LDT, r_G0326 for Gemini South) to be in R-band.

Using IRAF, I conducted photometry on both individual and stacked images. From this photometry, I derived instrumental magnitudes, which I then corrected for the zeropoint to calculate the apparent R-band magnitudes. After determining the weighted averages and standard deviations for these apparent magnitudes, I normalized them to unit heliocentric (r_h) and geocentric (Δ) distances using

$$m_{reduced} = m_R - 5 \log_{10}(r_h \Delta), \quad (2.3)$$

where $m_{reduced}$ is the reduced R-band magnitude, m_R is the average apparent magnitude, and r_h and Δ are measured in AU.

Next, I calculated the average absolute R-band magnitudes (H_R) using (e.g. Hsieh et al. 2010)

$$H_R = m_{reduced} + 2.5 \log_{10}[(1-G)\Phi_1(\alpha) + G\Phi_2(\alpha)], \quad (2.4)$$

where α is the solar phase angle and the term $\Phi(\alpha) = (1-G)\Phi_1(\alpha) + G\Phi_2(\alpha)$ is called the scattering phase function (Bowell et al. 1989). I utilized a value of $G = 0.15 \pm 0.12$ for 324P (and its dust), LH15 and 62412, considering them as C-type objects. The uncertainty assigned to G is the standard deviation of several G values reported by Lagerkvist & Magnusson (1990) (cf. Polishook & Brosch 2009).

There are measurements on the dust phase function for comets (Divine 1981; Schleicher 2010), however no measurements on the dust phase function for asteroids. Evidence suggests that the dust characteristics of comets differ from those of asteroids, as seen in the comparison between measurements from 67P/Churyumov-Gerasimenko and samples from Ryugu. Given these uncertainties, I opted to use the nucleus phase function (as the most logical) to approximate the unknown dust phase function, even though this is likely an oversimplification.

For HST data, I calculated the target magnitude using the relation

$$V = 20 - 2.5 \log_{10} \left[\frac{f}{n} \right], \quad (2.5)$$

obtained from the Exposure Time Calculator (ETC) for the Wide Field Camera 3 (WFC3) Ultraviolet-Visible (UVIS) channel⁴. V is the apparent magnitude in V-band, f is the count rate of the source in $e^- s^{-1}$, and n is the count rate obtained by the ETC in F350LP filter from a source with a sunlike (Kurucz G2V) spectrum renormalized to Vega magnitude 20 in Johnson/V filter.

⁴<https://etc.stsci.edu/etc/input/wfc3uvis/imaging/>.

By focusing only on data collected when the target was inactive, it is possible to derive the nucleus radius using (e.g. Hsieh et al. 2023)

$$r_N^2 = \frac{(2.24 \cdot 10^{16}) \cdot 10^{0.4(m_{\odot,R} - H_{R,inactive})}}{p_R}, \quad (2.6)$$

where $p_R = 0.05 \pm 0.02$ is the assumed geometric R-band albedo (Hsieh et al. 2009; Hsieh et al. 2023), $m_{\odot,R} = -27.15$ is the apparent R-band magnitude of the Sun⁵ (Willmer 2018), and $H_{R,inactive}$ is the absolute R-band magnitude of the inactive nucleus.

2.2.2 Methods for infrared images

Using IRAF, I measured the magnitudes of coadded WISE images, which I converted to fluxes using (Cutri et al. 2012)

$$F_\nu = F_{\nu,0} \cdot 10^{(-m_{Vega}/2.5)}, \quad (2.7)$$

where F_ν is the flux density in Jy, $F_{\nu,0}$ is the zero magnitude flux density (Wright et al. 2010; Mainzer et al. 2011; Masiero et al. 2011), and m_{Vega} is the measured WISE Vega magnitude, all at frequency ν . The values for F_ν are 306.682 Jy for W1, 170.663 Jy for W2, 29.045 Jy for W3, and 8.284 Jy for W4 (Cutri et al. 2012).

For Spitzer data, I performed photometric analysis on IRAF and obtained the Spitzer fluxes directly without the need to convert magnitudes to fluxes.

Infrared images reveal details about the thermal emission from cometary grains (Sarmecanic et al. 1997), while visual images provide insight into the reflectivity of the grains (Kolokolova et al. 2004). By combining these two types of information, the geometric albedo of the cometary grains can be determined. The geometric albedo is defined as the ratio of light scattered by the grains to the light that would be scattered at a zero phase angle by an ideal, perfectly reflective isotropic surface, also known as a Lambertian surface (Hanner et al. 1981).

The thermal component is described by (Jewitt & Meech 1988)

$$F_{IR} = \frac{\varepsilon S B_\nu(T)}{\Delta^2}, \quad (2.8)$$

where F_{IR} is the thermal flux density from the aperture in $\text{W m}^{-2} \text{Hz}^{-1}$, ε is the emissivity, here assumed to equal unity, S is the cross section of the cometary grains inside the aperture in m^2 , $B_\nu(T)$ is the Planck function evaluated at the temperature T in $\text{W m}^{-2} \text{Hz}^{-1} \text{sr}^{-1}$, and Δ is the geocentric distance in meters.

The scattered light component is expressed by (Russell 1916)

$$F_{vis} = F_\odot \frac{pj(\alpha)S}{(r_h/1\text{AU})^2 \pi \Delta^2}, \quad (2.9)$$

where F_\odot is the solar spectrum at 1 AU and at the wavelength used for the measurement of the flux from the MBC, F_{vis} , and both are in the same units. The quantities p and $j(\alpha)$ represent the geometric albedo of the dust particles and the scattering phase function, respectively, while r_h and Δ denote the heliocentric and geocentric distances in meters.

⁵<https://mips.as.arizona.edu/~cnaw/sun.html>.

2.3 Dust tail brightness profile method

To investigate the tail brightness profile, it is essential to choose images in which the target exhibits a clearly visible tail (step *Image Selection*). After making the selections, I employed the `imcombine` task in IRAF to process the images using the following steps. First, I removed the background sky flux from each individual image by subtracting the median value of the image. This establishes a more uniform base to work from. Next, I created a stellar composite by combining the images taken on each night in the World Coordinate System (WCS). During this step, I implemented the "minmax" algorithm to specify the highest and the lowest pixel values for rejection when calculating the average image. The comet moves between images taken at different times, while the stars remain fixed in the WCS. Since the comet appears at different positions in each image, its pixels vary and are effectively treated as outliers. These outliers are rejected, leaving behind the stars, which remain stationary and consistent across the frames. Furthermore, I set upper and lower thresholds for pixel values to eliminate saturated pixels—those with high-intensity values—and to discard overly negative values that represent the background noise. Lastly, I merged the images for each night within the co-moving frame of the MBC, again using the "minmax" algorithm along with the established pixel thresholds to remove the contribution from the stars. This process resulted in a single composite image that possesses a higher signal-to-noise ratio than any of the individual images (steps *Star Subtraction* and *Composite Image Creation*).

Next, I rotated the composite images to align the tail horizontally (step *Image Rotation*). I then determined the surface brightness of the tail using rectangular apertures of 24 pixels by 10 pixels, which I selected to be significantly wider than the nightly seeing to ensure that I captured all light from the tail, even in sub-optimal conditions (step *Surface Brightness Measurement*). To measure the sky background, I positioned two square 10 pixels by 10 pixels apertures above and below the central rectangular apertures (step *Sky Background Measurement*).

To subtract the background, I calculated the mean of the values from the square apertures (step *Background Subtraction*). In cases where contamination from stars occurred, I excluded the central rectangular box from consideration. If contamination was present in one of the square apertures, I relied on the opposite square to measure the mean, ensuring that I used the value from an uncontaminated aperture. The contaminated apertures are indicated in red in Fig. 2.1 (step *Final Corrections*) (Hsieh et al. 2004).

This approach is illustrated in Fig. 2.1, where I employed rectangular apertures measuring 40 pixels by 18 pixels, used exclusively for the cross section analysis (Sect. 3.3.4). These larger apertures were specifically designed to encompass a greater amount of light, providing higher S/N of the distribution and density of particles within the tail. In contrast, in the surface brightness analysis, I consistently used an aperture size of 24 pixels by 10 pixels to allow for direct comparison across all six tail images. This choice ensured that the measurements remained uniform.

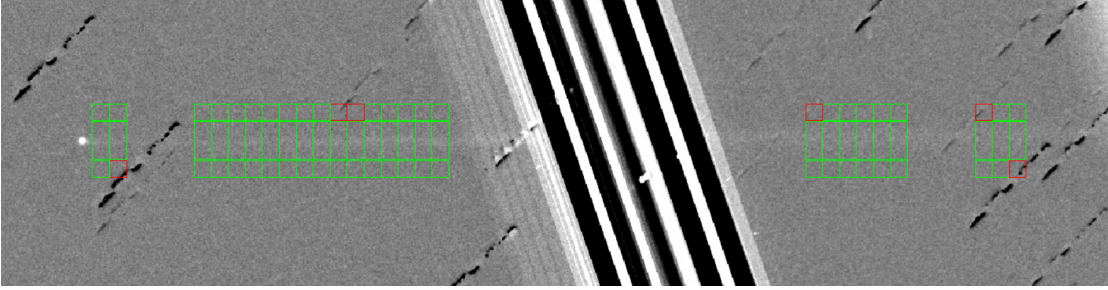


Figure 2.1: Methodology used to determine the surface brightness of the tail. In this case I used rectangular apertures of 40 pixels by 18 pixels.

To calculate the flux, I utilized the WCSTools software⁶ (Mink 1997), specifically the "sumpix" tool, to compute the mean and standard deviation within the apertures. This methodology encompassed the computation of total pixel values (measured in counts or analog-to-digital units, ADU) within the central rectangular aperture ($F_{aperture}$) and the total background pixel value (F_{bkg}), calculated by averaging the total background pixel values from the two square regions situated above and below the central rectangular region.

In this context, $F_{aperture}$ and F_{bkg} represent the mean flux per pixel for the main aperture and background regions, respectively. Since the following steps require the total flux rather than the mean, I employ $P_{aperture} = F_{aperture} \cdot N_{aperture}$ and $P_{bkg} = F_{bkg} \cdot N_{bkg}$, where $N_{aperture}$ and N_{bkg} denote the total number of pixels in the aperture and background regions, respectively.

The average background value per pixel was then computed as $\frac{P_{bkg}}{N_{bkg}}$. To account for the background contribution in the rectangular aperture, I multiplied the average background value by $N_{aperture}$ to get the total background contribution expressed as $\frac{P_{bkg}}{N_{bkg}} \cdot N_{aperture}$. Subsequently, the background-subtracted flux in the rectangular aperture was calculated as $P_{corrected} = P_{aperture} - \frac{P_{bkg}}{N_{bkg}} \cdot N_{aperture}$.

Next, I calculated the area of the rectangular aperture in arcseconds squared, given by $A_{arcsec} = N_{aperture} \cdot (px)^2$, where px is the pixel scale (in arcseconds per pixel). Using this area, I converted the corrected pixel value to flux per arcsecond squared using $F_{arcsec} = \frac{P_{corrected}}{A_{arcsec}}$. This conversion yields the flux in units of counts/arcsec².

To transform the flux to apparent magnitude, I applied

$$m_R = z_p - 2.5 \cdot \log_{10} \left(\frac{F_{arcsec}}{T_{exp}} \right), \quad (2.10)$$

where m_R indicates the apparent R-band magnitude per arcsec² for the central aperture, z_p is the zeropoint magnitude (calculated using flux in counts or ADU), and T_{exp} is the exposure time of the measurement. Finally, I transformed the apparent magnitude to absolute magnitude using Eq. (2.4) where in this instance $m_{reduced} = m_R - 5 \log_{10}(r_h)$ accounts solely for the heliocentric distance, it is independent on geocentric distance. As the geocentric distance to an object increases, the number of particles in a given area of the sky increases proportional to Δ^2 , while the light from each particle decreases proportional to Δ^{-2} due to the inverse-square law. These two effects cancel each other out, making the surface brightness independent of geocentric distance.

⁶<http://tdc-www.harvard.edu/wcstools/>.

After calculating the tail surface brightness, I plotted it against the distance from the nucleus, measured in arcseconds of mean anomaly (MA), which is a measure of time along an orbit (Sect. 3.3.1). The mean anomaly relates to the fraction of the orbital period that has passed since perihelion, but it is not a physically meaningful angle in terms of where the body actually is in its orbit. True anomaly, by contrast, is the actual physical angle that describes the position of an object along its orbit at any given time, but its rate of change varies because of Kepler's laws, i.e. objects move faster at perihelion and slower at aphelion. I chose to plot brightness versus mean anomaly because if two dust particles are ejected from the comet and follow slightly different orbits, the difference in their mean anomalies to the first order will remain constant over time, while their true anomalies will change at different rates due to their varying speeds at different points in the orbit. Plotting surface brightness versus mean anomaly reveals how the dust disperses over time, providing insights into the dust dynamics within the tail.

The semimajor axes of the comet and the Earth, together with their respective perihelion dates and the observation time t_{obs} (the six dates in Fig. 3.14), are required to calculate the mean anomaly for both the comet and the Earth at t_{obs} . The mean anomaly of the Earth is needed to calculate its position in space, which is then used to determine the position of the comet relative to the Earth by subtracting the coordinates of the Earth from the coordinates of the comet. This relative position is crucial for accurately calculating the angular extent of the tail of the comet as observed from Earth. To compute the mean anomaly, the following equation is applied, which relates the elapsed time since perihelion to the position of the body in its orbit

$$MA = \sqrt{\frac{GM_{\odot}}{a^3}}(t_{obs} - t_{perihelion}), \quad (2.11)$$

where $GM_{\odot} = 2.9593 \cdot 10^{-4} \text{ AU}^3 \text{ days}^{-2}$ is the gravitational parameter with $G = 6.67 \cdot 10^{-11} \text{ m}^3 \text{ kg}^{-1} \text{ s}^{-2}$ being the gravitational constant and $M_{\odot} = 1.989 \cdot 10^{30} \text{ kg}$ being the mass of the Sun, and $(t_{obs} - t_{perihelion})$ is the time difference from perihelion.

Once the mean anomaly is calculated, the orbital elements of both the comet and the Earth are converted into their corresponding cartesian coordinates (X, Y, Z) at t_{obs} . The orbital elements include the semimajor axis (a), eccentricity (e), inclination (i), longitude of the ascending node (Ω), and argument of perihelion (ω) (Sect. 1.1.3). This step provides their positions in space. For the conversion, first the Kepler's equation is applied to calculate the eccentric anomaly (E) (Montenbruck & Gill 2000)

$$MA = E - e \cdot \sin E. \quad (2.12)$$

The eccentric anomaly, represented in Fig. 2.2, is the angle between the perihelion (P), the center of the ellipse, and the point B', which is located by drawing a perpendicular to the major axis of the ellipse passing through the position of the comet at a certain point B and intersecting a circle of diameter equal to the major axis of the ellipse. Then, the heliocentric distance is calculated as (Montenbruck & Gill 2000)

$$r = a(1 - e \cdot \cos E). \quad (2.13)$$

Next, the true anomaly (ν) is obtained as (Klioner 2016)

$$\nu = 2 \arctan \left(\sqrt{\frac{1+e}{1-e}} \tan \left(\frac{E}{2} \right) \right). \quad (2.14)$$

Finally, the cartesian coordinates are calculated using (Montenbruck & Gill 2000)

$$\begin{pmatrix} X \\ Y \\ Z \end{pmatrix} = r \begin{pmatrix} \cos u \cos \Omega - \sin u \cos i \sin \Omega \\ \cos u \sin \Omega + \sin u \cos i \cos \Omega \\ \sin u \sin i \end{pmatrix}, \quad (2.15)$$

with $u = \omega + \nu$ as the angle between r and the line of nodes (Fig. 1.8).

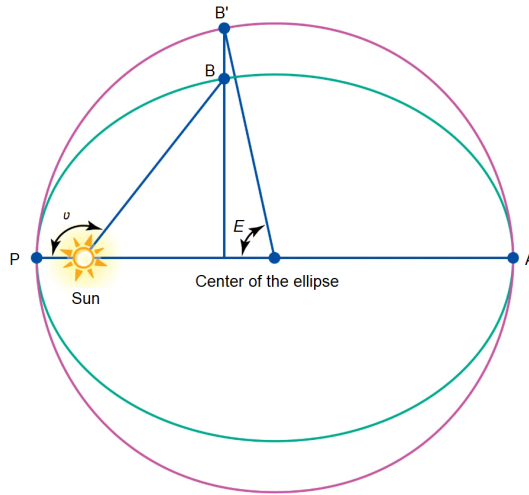


Figure 2.2: True anomaly and eccentric anomaly. Points A and P represent the aphelion and perihelion of the comet, respectively, while point B marks the position of the comet at a specific moment in its orbit and B' is its projection of a circle concentric to the ellipse. The angles ν and E denote the true and eccentric anomalies, respectively. Modified image from: Encyclopædia Britannica.

I used a C program (by Jessica Agarwal, calling the routines written by A.V. Krivov, 1996) to carry out the steps described. In the last step, the main goal is to calculate the angular extent of the dust tail of the comet as seen from Earth. The program first calculates the position of the comet relative to Earth at t_{obs} , represented by the position vector l_2 . This vector is obtained by subtracting the cartesian coordinates of the Earth from the cartesian coordinates of the comet at t_{obs} . Next, the program adjusts the mean anomaly of the comet by subtracting a small value, $\Delta_{MA} = 0.1^\circ$. This adjustment simulates where the tail of the comet would be located if we considered material ejected at an earlier time in its orbit. After adjusting the mean anomaly, the cartesian coordinates of this new position relative to Earth, represented by the vector l_1 , are computed using the same method. To determine the angular extent of the tail of the comet, the program calculates the Euclidean distances from Earth to the positions l_1 and l_2 . Then it finds the angle between these two position vectors using the dot product formula. This angle represents the angular extent of the tail of the comet that corresponds to a change in mean anomaly of $\Delta_{MA} = 0.1^\circ$. Using this information, I can determine how many arcseconds in mean anomaly correspond to one arcsecond in the projected sky. The conversion factor is $\Delta_{MA}/\text{arcsec}$. Since the distances from the nucleus to various parts of the tail are initially measured in pixels, I first convert these distances into arcseconds. By multiplying the resulting values by the conversion factor $\Delta_{MA}/\text{arcsec}$, I obtain the corresponding distances from the nucleus in arcseconds of mean anomaly. This allows me to express the position of different tail segments in terms of their orbital distance, or mean anomaly.

2.4 Dust tail modelling

2.4.1 The Finson and Probstein model

The Finson and Probstein (FP) model (Finson & Probstein 1968) determines the trajectories of dust particles by considering the influences of gravitational force (F_{grav}) and solar radiation pressure (F_{rad}). The β parameter represents the ratio of these two forces, defined as (Burns et al. 1979)

$$\beta = \frac{F_{rad}}{F_{grav}} = \frac{KQ_{pr}}{\rho r}, \quad (2.16)$$

where $K = 5.7 \cdot 10^{-4} \text{ kg m}^{-2}$ is a constant in the solar gravitational and radiation field, $Q_{pr} = 1$ (Ishiguro 2008) is the radiation pressure coefficient, ρ_d is the mass density of the particle in kg m^{-3} , and r is the particle radius in meters. The β parameter is inversely related to the particle size, indicating that smaller particles (with higher β values) experience a greater influence from solar radiation and therefore follow more elongated trajectories. In contrast, larger particles (with lower β values), being less influenced by solar radiation, stay close to the nucleus. Generally, the model described in Finson & Probstein (1968) considers a non-zero relative velocity between the comet and dust particles.

2.4.2 The syndynes and synchrones model

In my simplified case, I assumed the relative velocity between the comet and the dust particles to be zero. I implemented an FP model in Python using the `solve_ivp` module. The program processes a range of β values, simulating the motion of dust particles over a specified time period, and generates a series of curves (known as syndynes) that indicate the positions of the grains. Each syndyne represents dust with a specific β value that has been continuously released from a given point in the past up to the moment represented in the image. Synchrones instead connect particles released simultaneously but with different β values. An example of the model can be found in Fig. 2.3. The aim of the model is to accurately represent the tail of the object to understand the size of the particles ejected and when they were ejected. This is achieved by trying different combinations of β and the time when the particles were emitted (T_{emiss}).

This code is designed to generate syndyne-synchrone plots for any MBCs. It is capable of functioning effectively down to a minimum beta value of $\beta = 10^{-7}$. I also cross-referenced my findings with the Comet-toolbox⁷ developed by J.-B. Vincent (Vincent 2014), and I found that the outcomes were consistent in all cases. This corroboration lends further credibility to the results obtained from my analysis.

⁷<https://www.comet-toolbox.com/FP.html>.

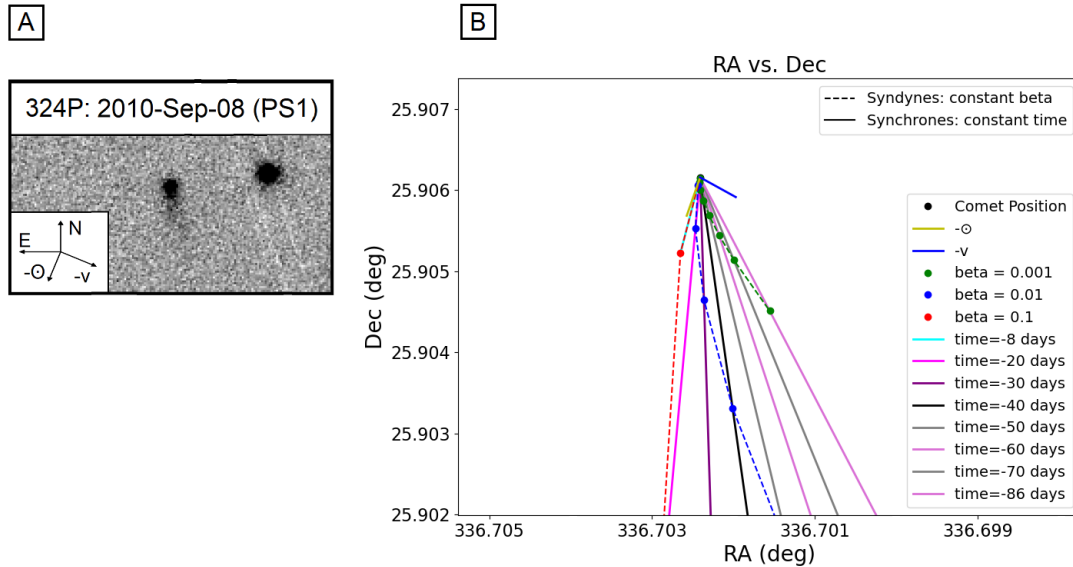


Figure 2.3: Panel A: visual image of 324P (at the center of the panel) on 2010 September 8 taken with the PS1 telescope. Dates and directions on sky are labeled as in Fig. 3.2. Panel B: right ascension vs. declination plot showing the result of the syndyne-synchrone model on the image on the right side. Dashed lines indicate syndynes, while solid lines represent synchrones. The black dot marks the position of the comet on 2010 September 8, the yellow line represents the antisolar direction, and the blue line indicates the negative heliocentric velocity vector. The legend also defines the combinations of beta values and emission times used to generate the results.

2.4.3 Implementation

For the implementation of the syndyne-synchrone code, I utilized Python and created several files, each serving a distinct purpose in the overall simulation of cometary dynamics and related observational calculations.

The `comet.py` file defines the characteristics of the comet, including the identification of the comet and the observation date of the image of the tail. This script retrieves the position, velocity, and orbital elements of the comet from the Jet Propulsion Laboratory (JPL) Horizons System. The position and velocity are calculated relative to the Sun and in the reference frame aligned with equatorial plane of the Earth. The motion of the comet is modeled using Newton's gravitational law, defining the differential equations of motion under the gravitational force of the Sun. It is important to note that the model assumes the orbit of the comet is primarily influenced by the gravity of the Sun, thus neglecting perturbations caused by other celestial bodies. To solve the system of ordinary differential equations (ODEs) over a time span of 5.448 yr, corresponding to the orbital period of 324P, the `solve_ivp` function, which is designed for solving initial value problems for ODEs, is employed. A time step of 100 seconds is used to ensure an accurate numerical solution of the system over the specified orbital period. To test the accuracy, smaller time steps were initially tested, with a time step of 1 second taking a significantly long time to compute, and 10 seconds still requiring considerable computational effort. However, the results obtained with a time step of 100 seconds were virtually identical to those from the smaller time steps, demonstrating that 100 seconds is sufficient for accurate

simulation while being computationally much more efficient. The solution is computed using the DOP853 method, a Runge-Kutta method of order 8.

Complementary to the motion of the comet, the `earth.py` file is dedicated to simulating the position of the Earth and its orbit. This file utilizes a similar approach as the one used in `comet.py`.

The `LST.py` script is designed to calculate the Local Sidereal Time (LST) based on the geographical location of the observer, specifically the location of the telescope used to capture the astronomical image. In this case, the coordinates correspond to the Mauna Kea Observatory in Hawaii, where the Gemini North Telescopes was used to observe the object 324P on 2011 December 31. The Mauna Kea Observatory is situated at a latitude of $19^\circ 49' 34''$ N, a longitude of $155^\circ 28' 20''$ W, and an elevation (height above sea level) of $A = 4205$ meters⁸. The LST represents the right ascension (RA) of a celestial object that are at the meridian of the observer, at a given time and location. To compute the LST, the script uses the `sidereal_time()` method from the `Astropy` library.

The `particle.py` file simulates the motion of dust particles ejected from the comet under the influence of both the gravity of the Sun and the solar radiation pressure, represented by the parameter β . This file builds upon the position data obtained from `comet.py` and simulates the trajectory of the comet backward in time to determine when the particles were ejected. It then simulates the forward motion of the particles from the ejection point to the observation time. The gravitational acceleration acting on the particles is modified by a factor of $(1 - \beta)$ to incorporate the effects of radiation pressure.

Finally, the `main.py` file serves as the integration point for all components, orchestrating the calculations and visualizations of the position of the comet and the trajectories of the particles on the celestial sphere presented in terms of RA and declination (Dec).

First, the geocentric equatorial cartesian coordinates of the observing location are calculated using⁹

$$\begin{cases} r_g = \left[\left(\frac{\cos(\delta)}{R_E} \right)^2 + \left(\frac{\sin(\delta)}{R_P} \right)^2 \right]^{-\frac{1}{2}} + A \\ a_g = r_g \cdot \cos(\alpha) \cos(\delta) \\ b_g = r_g \cdot \sin(\alpha) \cos(\delta) \\ c_g = r_g \cdot \sin(\delta) \end{cases} \quad (2.17)$$

where r_g is the distance from the center of the Earth to the observing location, $R_E = 6378.135$ km is the equatorial radius of the Earth, $R_P = 6356.752$ km is the polar radius of the Earth and A in kilometers is the elevation of the observing location. The values of δ and α are the latitude¹⁰ and the LST¹¹, respectively.

Then the topocentric cartesian coordinates of the comet are derived using

$$\begin{cases} x_s = x_g - a_g \\ y_s = y_g - b_g \\ z_s = z_g - c_g \end{cases} \quad (2.18)$$

⁸https://www.eso.org/gen-fac/pubs/astclim/espas/espas_reports/.

⁹http://www.castor2.ca/04_Propagation/10_Geo_Cart/index.html.

¹⁰The latitude of the observer on the Earth is nearly the same as the declination of the same location as viewed from the center of the Earth.

¹¹The geocentric RA of the observing location is its LST.

where (x_g, y_g, z_g) represent the geocentric cartesian coordinates within the Earth-centered reference frame. The conversion from the heliocentric reference frame to the Earth-centered reference frame involves calculating the vector differences between the positions of the comet and Earth, defined by

$$\begin{cases} x_g = x_c - x_e \\ y_g = y_c - y_e \\ z_g = z_c - z_e \end{cases} \quad (2.19)$$

where (x_c, y_c, z_c) and (x_e, y_e, z_e) are the position of the comet and Earth in the heliocentric reference frame, respectively.

Finally, the topocentric equatorial coordinates of the comet are derived as seen from the observing location on the Earth using

$$\begin{cases} \alpha = \tan^{-1}[y_s/x_s] \text{ for } y_s > 0 \text{ and } x_s > 0 \\ \alpha = 180^\circ + \tan^{-1}[y_s/x_s] \text{ for } x_s < 0 \\ \alpha = 360^\circ + \tan^{-1}[y_s/x_s] \text{ for } y_s < 0 \text{ and } x_s > 0 \\ r = [x_s^2 + y_s^2 + z_s^2]^{\frac{1}{2}} \rightarrow \delta = \sin^{-1}[z_s/r] \end{cases} \quad (2.20)$$

Following the same methodology employed for the comet, the topocentric coordinates of the dust particles were derived using the established procedures. Both the comet and the particles are then plotted on a RA-Dec plot. The angles between the particle trajectories and the x-axis are computed and recorded, along with the angular separation between the comet and each particle, expressed in degrees. These measurements are essential for comparison with the values obtained from image analysis, as discussed in Sect. 3.3.2, to ensure accurate results. The simulation explores a range of radiation pressure coefficients (β) and various emission times to gain a comprehensive understanding of particle dynamics.

3 Analysis of 324P/La Sagra

3.1 Dataset

3.1.1 Telescopes

Archival visible light images of 324P were obtained with the following telescopes and instruments:

- the GPC1 instrument on the 1.8-meter PS1 telescope at Haleakalā Observatory in Hawaii, USA ($0.25'' \text{ pixel}^{-1}$);
- the WFC instrument on the 2.54-meter INT telescope at the Roque de los Muchachos Observatory in La Palma, Spain ($0.33'' \text{ pixel}^{-1}$);
- the Gemini Multi-Object Spectrograph North (GMOS-N) instrument on the 8-meter Gemini North Telescopes on Mauna Kea in Hawaii, USA ($0.14'' \text{ pixel}^{-1}$);
- the ESO Faint Object Spectrograph and Camera (EFOSC) instrument on the 3.6-meter NTT telescope at the La Silla Observatory in Chile ($0.24'' \text{ pixel}^{-1}$);
- the FOcal Reducer and low dispersion Spectrograph 2 (FOR2) instrument on the 8-meter VLT telescope at the Paranal Observatory in Chile ($0.25'' \text{ pixel}^{-1}$);
- the MegaPrime instrument on the 3.6-meter CFHT telescope on Mauna Kea in Hawaii, USA ($0.18'' \text{ pixel}^{-1}$);
- the Large Monolithic Images (LMI) instrument on the 4.3-meter LDT telescope at the Lowell Observatory in Arizona, USA ($0.24'' \text{ pixel}^{-1}$);
- the Gemini Multi-Object Spectrograph South (GMOS-S) instrument on the 8-meter Gemini South Telescopes on Cerro Pachón in Chile ($0.16'' \text{ pixel}^{-1}$);
- the WFC3 instrument on the HST telescope ($0.04'' \text{ pixel}^{-1}$).

Infrared images (IR) of 324P were taken:

- with the WISE telescope with a 0.4-meter diameter primary mirror ($2.75''$ per pixel in W1 band at $3.4 \mu\text{m}$, W2 band at $4.6 \mu\text{m}$ and W3 band at $12 \mu\text{m}$, $5.5''$ per pixel in W4 band at $22 \mu\text{m}$);
- and with the IRAC instrument on the Spitzer telescope with a 0.85-meter diameter primary mirror ($1.22'' \text{ pixel}^{-1}$ in channels 1 ($3.6 \mu\text{m}$) and 2 ($4.5 \mu\text{m}$)).

3.1.2 Observations

The following part is described in Mastropietro et al. (2024a).

I examined archival data of 324P collected between 2010 and 2020. Additionally, in collaboration with Henry Hsieh, I analyzed its recent perihelion passage in 2021 (Program ID: GN-2021A-LP-104, GN-2021B-LP-104 and GS-2021B-LP-104, PI: Hsieh) (Fig. 3.1).

In Table 3.1 are the heliocentric and geocentric distances, the phase angles and true anomalies of the date of observations.

Images captured at both optical and infrared wavelengths were identified using the Canadian Astronomy Data Centre (CADC) website¹ (Gwyn et al. 2012) and from the Infrared Science Archive (IRSA) website².

All visible light images used in this study (Fig. 3.2) were obtained in R-band, except for the PS1 image dated 2010 June 26 (which is in z-band), 4 PS1 images from 2010 September 08 (g-band), and HST images in F350LP filter which has the pivot wavelength (Marinelli & Dressel 2024) at 587.39 nm, similar to V-band. VLT images on 2019 April 12 have $S/N < 8$, hence I excluded them from further analysis. I did not detect 324P in ZTF images from 2019 April 09, 2019 April 12, 2019 April 19, and 2019 April 28. IR images of 324P (Fig. 3.3) were taken on 2010 June 9 – 11 (true anomaly of $\nu = -3.9^\circ$, in the active phase) with the WISE telescope and on 2016 January 8 ($\nu = 9.8^\circ$, also in the active phase) with the Spitzer telescope.

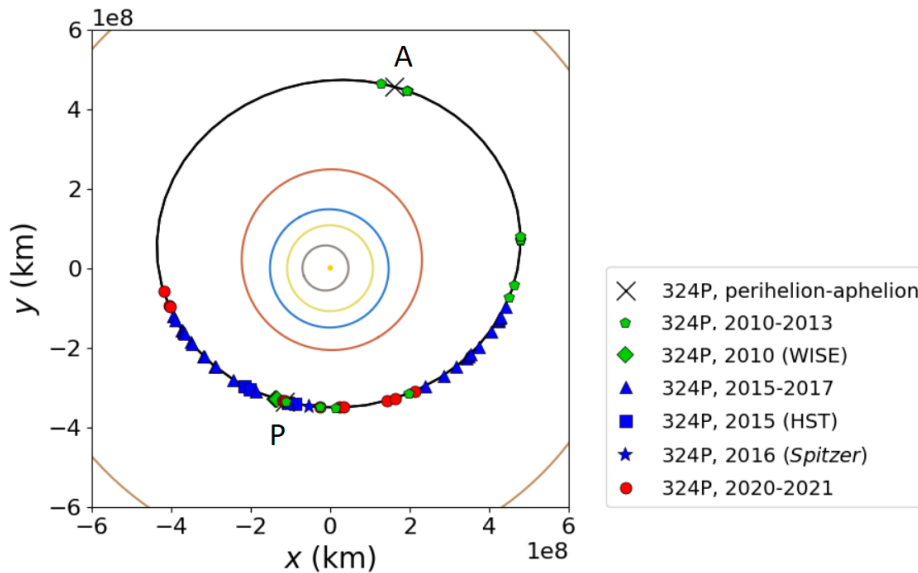


Figure 3.1: The heliocentric ecliptic coordinate system is used to represent this orbital plot. The origin is the center of the Sun, the plane of reference is the ecliptic plane, and the direction of the x-axis points toward the vernal equinox. The plot shows the positions of 324P at the epochs of my observations with the orbits of Mercury, Venus, Earth, Mars, 324P, and Jupiter. X-dots represent perihelion (P) and aphelion (A) positions. Pentagonal, triangular, square and circular dots are visual data, while diamond and starred dots are IR data. Plot generated using the poliastro Python library (Juan Luis Cano Rodríguez & Jorge Martínez Garrido 2022). Credit: Mastropietro et al. (2024a), Figure 1.

¹<https://www.cadc-ccda.hia-ihp.nrc-cnrc.gc.ca/en/ssois/index.html>.

²<https://irsa.ipac.caltech.edu/frontpage/>.

Table 3.1: Observations of the MBC 324P. Credit: Mastrogiro et al. (2024a), Table A.1 (adapted).

UT Date	Telescope ^a	N ^b	r_h^c	Δ^d	α^e	ν^f	m_R^g	H_R^h	M_d (x 10 ⁶) ⁱ
2010 Jun 25	<i>Perihelion</i>	–	2.623	2.239	22.4	0.0	–	–	–
2010 Jun 26	PS1	1	2.623	2.228	22.3	0.0	20.7 ± 0.5	15.8 ± 0.5	14 ± 9
2010 Aug 16*	PS1	4	2.631	1.795	15.1	12.8	19.19 ± 0.02	15.0 ± 0.1	32 ± 13
2010 Sep 08*	PS1	1	2.641	1.739	12.0	18.4	19.14 ± 0.05	15.1 ± 0.1	28 ± 12
2010 Sep 08	PS1	4	2.641	1.739	12.0	18.4	18.9 ± 0.1	14.9 ± 0.2	35 ± 15
2010 Dec 31*	INT	11	2.732	2.782	20.5	45.7	20.8 ± 0.1	15.4 ± 0.2	21 ± 9
2011 Aug 31*	GN	6	3.072	3.238	18.2	95.9	24.4 ± 0.1	18.5 ± 0.2	-0.1 ± 0.7
2011 Sep 25**	GN	9	3.110	2.929	18.8	100.4	23.8 ± 0.1	18.0 ± 0.2	0.6 ± 0.8
2011 Dec 22	NTT	8	3.236	2.257	1.9	115.5	23.0 ± 0.2	18.4 ± 0.2	0.0 ± 0.7
2011 Dec 23	NTT	10	3.238	2.260	2.2	115.7	22.9 ± 0.2	18.3 ± 0.2	0.1 ± 0.7
2011 Dec 31**	GN	9	3.249	2.295	5.0	117.0	23.0 ± 0.1	18.2 ± 0.1	0.3 ± 0.7
2013 Feb 11	NTT	27	3.568	2.643	6.4	176.0	24.0 ± 0.2	18.6 ± 0.2	-0.2 ± 0.7
2013 Feb 12	NTT	10	3.568	2.643	6.4	176.2	23.7 ± 0.2	18.3 ± 0.2	0.1 ± 0.7
2013 Feb 13	NTT	9	3.568	2.643	6.4	176.3	23.9 ± 0.1	18.5 ± 0.1	-0.1 ± 0.7
2013 Mar 12	<i>Aphelion</i>	–	3.569	2.750	10.3	180.0	–	–	–
2013 Apr 08**	GN	8	3.568	3.017	14.6	183.6	24.2 ± 0.2	18.2 ± 0.2	0.3 ± 0.7
2015 Apr 18	VLT	15	2.773	2.559	21.2	305.7	23.3 ± 0.3	18.0 ± 0.3	0.6 ± 0.9
2015 Apr 19	VLT	18	2.772	2.544	21.2	306.0	23.1 ± 0.1	17.8 ± 0.2	1.0 ± 0.9
2015 May 22	VLT	16	2.734	2.088	18.8	313.4	22.6 ± 0.1	17.8 ± 0.2	1.0 ± 0.9
2015 Jun 10	VLT	18	2.713	1.878	14.7	317.8	22.2 ± 0.1	17.8 ± 0.2	1.0 ± 0.9
2015 Jun 10***	CFHT	3	2.713	1.878	14.7	317.8	21.959 ± 0.002	17.6 ± 0.1	1.5 ± 1.0
2015 Jun 13***	CFHT	9	2.710	1.850	13.8	318.5	22.2 ± 0.2	17.9 ± 0.2	0.8 ± 0.8
2015 Jul 10	VLT	5	2.685	1.693	6.0	324.9	21.7 ± 0.1	17.9 ± 0.1	0.8 ± 0.8
2015 Jul 12	CFHT	3	2.683	1.688	5.6	325.4	21.38 ± 0.04	17.6 ± 0.1	1.4 ± 0.9
2015 Aug 04	VLT	9	2.665	1.715	9.6	330.9	22.0 ± 0.3	18.1 ± 0.3	0.4 ± 0.8
2015 Aug 05	VLT	14	2.664	1.719	9.9	331.1	21.8 ± 0.1	17.8 ± 0.1	1.0 ± 0.8

Continued on next page

Table 3.1: (continued)

UT Date	Telescope ^a	N ^b	r_h^c	Δ^d	α^e	ν^f	m_R^g	H_R^h	M_d ($\times 10^6$) ⁱ
2015 Sep 09	VLT	4	2.642	1.990	19.3	339.6	22.4 ± 0.1	17.8 ± 0.2	1.0 ± 0.9
2015 Oct 18	CFHT	2	2.626	2.443	22.3	349.3	22.6 ± 0.1	17.5 ± 0.2	1.8 ± 1.1
2015 Nov 30	<i>Perihelion</i>	–	–	2.620	2.946	19.3	0.0	–	–
2015 Dec 08	LDT	10	2.620	3.029	18.3	2.0	22.2 ± 0.1	16.8 ± 0.2	4.8 ± 2.3
2016 Jul 08	CFHT	6	2.768	3.067	19.2	53.2	22.8 ± 0.1	17.2 ± 0.2	2.8 ± 1.5
2016 Aug 10	GN	4	2.810	2.724	21.0	60.5	23.1 ± 0.1	17.6 ± 0.2	1.5 ± 1.0
2016 Sep 05	GN	4	2.845	2.436	20.2	66.0	23.3 ± 0.1	18.1 ± 0.2	0.4 ± 0.8
2016 Sep 27	GN	5	2.876	2.214	17.2	70.7	23.0 ± 0.1	18.0 ± 0.2	0.6 ± 0.7
2016 Oct 02	CFHT	5	2.883	2.171	16.2	71.7	22.7 ± 0.1	17.8 ± 0.2	1.0 ± 0.9
2016 Oct 07	CFHT	8	2.890	2.131	15.0	72.7	22.9 ± 0.2	18.1 ± 0.2	0.4 ± 0.8
2016 Oct 25	CFHT	5	2.917	2.026	10.4	76.4	22.5 ± 0.1	18.0 ± 0.1	0.6 ± 0.7
2016 Oct 25	GN	4	2.917	2.026	10.4	76.4	22.54 ± 0.04	18.0 ± 0.1	0.6 ± 0.7
2016 Nov 29	GN	3	2.969	2.054	8.5	83.3	22.7 ± 0.1	18.2 ± 0.1	0.4 ± 0.7
2016 Dec 22	GN	4	3.004	2.250	13.9	87.7	23.1 ± 0.1	18.2 ± 0.2	0.3 ± 0.7
2016 Dec 23	CFHT	5	3.006	2.261	14.2	87.9	23.0 ± 0.1	18.0 ± 0.2	0.6 ± 0.8
2016 Dec 28	CFHT	9	3.013	2.320	15.2	88.9	23.1 ± 0.3	18.0 ± 0.3	0.6 ± 0.9
2016 Dec 29	CFHT	5	3.015	2.332	15.3	89.1	23.2 ± 0.1	18.1 ± 0.2	0.4 ± 0.8
2017 Jan 20	GN	5	3.048	2.636	18.1	93.2	23.9 ± 0.1	18.4 ± 0.2	0.0 ± 0.7
2018 Aug 19	<i>Aphelion</i>	–	–	3.571	4.544	180.0	–	–	–
2020 Aug 13	GN	4	2.826	2.390	20.3	296.7	23.2 ± 0.2	18.0 ± 0.2	0.6 ± 0.8
2020 Sep 08	GN	3	2.792	2.705	21.0	302.4	23.7 ± 0.2	18.3 ± 0.2	0.1 ± 0.7
2020 Sep 10	GN	4	2.789	2.729	21.0	302.8	23.7 ± 0.1	18.3 ± 0.2	0.1 ± 0.7
2021 May 06	<i>Perihelion</i>	–	–	2.618	2.972	19.5	0.0	–	–
2021 May 10	GN	3	2.619	2.931	20.0	1.0	23.35 ± 0.05	17.9 ± 0.2	0.8 ± 0.8
2021 May 12	GN	3	2.619	2.910	20.2	1.5	23.38 ± 0.03	18.0 ± 0.2	0.7 ± 0.8
2021 Jul 04	GN	3	2.630	2.330	22.6	14.7	22.29 ± 0.06	17.3 ± 0.2	2.6 ± 1.4

Continued on next page

Table 3.1: (continued)

UT Date	Telescope ^a	N ^b	r_h^c	Δ^d	α^e	ν^f	m_R^g	H_R^h	M_d (x 10 ⁶) ⁱ
2021 Aug 03	GN	3	2.645	2.033	20.1	22.2	21.57 ± 0.05	16.9 ± 0.2	4.2 ± 2.0
2021 Aug 08	GN	3	2.648	1.991	19.4	23.4	21.51 ± 0.01	16.9 ± 0.2	4.1 ± 1.9
2021 Oct 14	GN	3	2.701	1.839	13.0	39.5	20.82 ± 0.04	16.6 ± 0.1	6.1 ± 2.7
2021 Oct 27	GN	3	2.714	1.920	15.0	42.5	21.00 ± 0.07	16.6 ± 0.2	6.1 ± 2.7
2021 Nov 29	GS	4	2.750	2.253	19.7	50.1	21.86 ± 0.04	16.9 ± 0.2	4.2 ± 2.0
2024 Jan 24	<i>Aphelion</i>	–	3.570	2.750	10.0	180.0	–	–	–
2026 Oct 14	<i>Perihelion</i>	–	2.625	2.232	21.8	0.0	–	–	–
2010 June 9 – 11	WISE	19, 18	2.623	2.410	22.8	356.1	–	–	–
2016 Jan 08	Spitzer	70, 71	2.625	1.964	19.8	9.8	–	–	–
2015 Sep 28	HST	4	2.633	2.202	21.6	344.3	22.0 ± 0.1	17.1 ± 0.2	–
2015 Oct 08	HST	4	2.629	2.321	22.2	346.8	22.4 ± 0.1	17.4 ± 0.2	–
2015 Dec 07	HST	4	2.620	3.019	18.4	1.8	22.2 ± 0.1	16.8 ± 0.2	–
2015 Dec 18	HST	4	2.621	3.127	16.9	4.5	21.9 ± 0.1	16.4 ± 0.2	–

^aTelescope. ^bNumber of exposures taken. ^cHeliocentric distance in AU. ^dGeocentric distance in AU. ^eSolar phase angle (Sun-Target-Observer) in degrees. ^fTrue anomaly in degrees. ^gApparent R-band magnitude measured with a 2300 km physical radius. ^hAbsolute R-band magnitude assuming IAU H-G phase function where $G = 0.15 \pm 0.12$. ⁱEstimated dust mass in kg assuming $\rho_d \sim 2500 \text{ kg m}^{-3}$.

Note 1: Data presented in the last three columns are the results of my photometric analysis. Data from dates marked with asterisks were previously published in Hsieh et al. (2012b) (*), Hsieh (2014) (**), and Hsieh & Sheppard (2015) (***). The HST dataset has been previously analyzed in Jewitt et al. (2016). Note 2: For WISE, 19 images were obtained in W1 and W2 bands, and 18 in W3 and W4 bands. For Spitzer, 70 images were taken in ch1 and 71 in ch2. Note 3: For HST, the apparent V-band magnitude was measured inside a 3000 km physical radius, and the absolute V-band magnitude was derived assuming an IAU H-G phase function with $G = 0.15 \pm 0.12$.



Figure 3.2: Mosaic of the visual R-band images (exceptions: 2010 June 26 (PS1) in z-band; 2010 September 08 (PS1) in g-band) of 324P (at the center of each panel). All panels have north (N), east (E), the antisolar direction ($-O$) and the negative heliocentric velocity vector ($-v$), as projected on the sky, marked. Panels are labeled with dates of observation in UT YYYY-MM-DD format, and employed telescope (PS1: Panoramic Survey Telescope and Rapid Response System PanSTARRS1 (PS1); INT: Isaac Newton Telescope; GN: Gemini North Telescopes; NTT: New Technology Telescope; VLT: Very Large Telescope; CFHT: Canada-France-Hawaii Telescope; LDT: Lowell Discovery Telescope; GS: Gemini South Telescopes). Credit: Mastropietro et al. (2024a), Figure A.1.

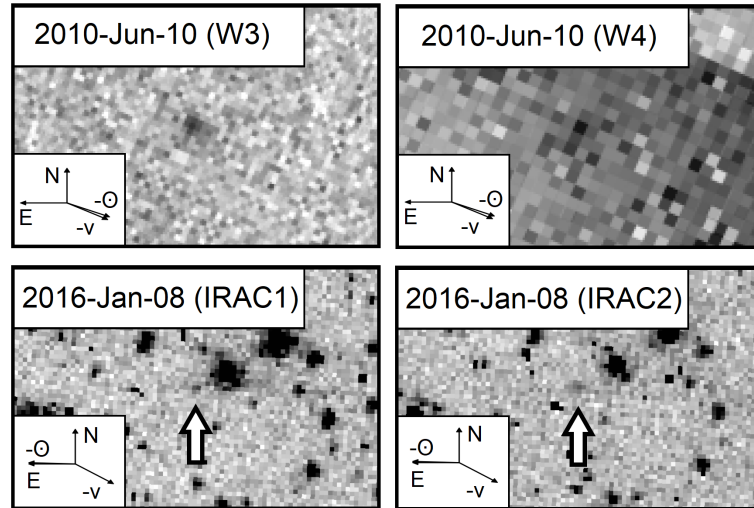


Figure 3.3: IR images of 324P (at the center of each panel). W3 and W4: WISE telescope at 12 μm and 22 μm , respectively; IRAC1 and IRAC2: Spitzer Space Telescope at 3.6 μm and 4.5 μm , respectively. Dates and directions on sky are labeled as in Fig. 3.2. Credit: Mastropietro et al. (2024a), Figure 2.

3.2 Photometry

The following parts are described in Mastropietro et al. (2024a).

3.2.1 Photometry in visible light

For the visible light images analysis, I conducted bias subtraction and flat-fielding, followed by photometric calibration as described in Sect. 2.1.

Using IRAF, I conducted photometry on individual images of 324P utilizing a circular aperture with a fixed physical radius of 2300 km at the comet. I chose to maintain a constant physical radius instead of a constant angular size to ensure that the same volume surrounding the nucleus was sampled in each measurement. Afterwards, for each dataset, I computed the weighted average of the apparent magnitudes obtained from the individual exposures, yielding one measurement point for each epoch and telescope (Table 3.1). For photometry on HST images instead, I carried out circular aperture photometry on stacked images (Jewitt et al. 2016) with a fixed physical radius of 3000 km at the comet to maintain consistency in the comparative analysis with the Spitzer data.

As result of the photometry, as in Sect. 2.2.1, I determined the apparent R-band magnitudes for the individual images, as well as for the stacked images in the case of HST data. For the HST data, to calculate the apparent magnitude I used Eq. (2.5), where the count rate is from ETC Request IDs: WFC3UVIS.im.1845086, WFC3UVIS.im.1845087, WFC3UVIS.im.1845088, WFC3UVIS.im.1845089.

The average apparent and absolute R-band magnitudes are listed in Tables 3.1 and 3.2. The graphics of the absolute R-band magnitudes as a function of true anomaly are in Figs. 3.4 and 3.5.

In Fig. 3.5, I present a comparison of my photometric measurements with previously published data. The pentagonal data points outlined in black were obtained using an aperture angular radius of $5''$, as opposed to 2300 km, which allows for a direct comparison with the results of Hsieh et al. (2012b) (the green x-shaped data points in Fig. 3.5 and Table 3.2). The observed discrepancy of approximately 1 mag may be due to advancements in all-sky photometric catalogs since the initial study was conducted. Additionally, Table 3.2 includes measurements from a $2''$ aperture across five epochs in 2015, allowing for comparison with the work of Hsieh & Sheppard (2015), who employed the same aperture size but utilized a different IAU phase function G parameter, specifically $G = 0.17 \pm 0.10$, as in Hsieh (2014). In this scenario, my findings are consistent with theirs. Furthermore, Fig. 3.5 also presents HST data from Jewitt et al. (2016) along with my results for the same datasets. These results were converted from V-band to R-band using a $V - R = 0.35$ conversion, and they show good agreement.

Table 3.2: Measurements on the MBC 324P with apertures different from my standard 2300 km radius, for comparison with published values (see text). The measurements listed here were obtained with a 5'' aperture for data in 2010 and 2011 and with a 2'' aperture for data in 2015. Credit: Mastroietro et al. (2024a), Table 2.

UT Date	Telescope ^a	N ^b	r _h ^c	Δ^d	α^e	ν^f	m_R^g	H_R^h	M_d (x 10 ⁶) ⁱ
2010 Aug 16	PS1	4	2.631	1.795	15.1	12.8	18.7 ± 0.1	14.5 ± 0.2	50 ± 22
2010 Sep 08	PS1	3	2.641	1.739	12.0	18.4	18.40 ± 0.05	14.4 ± 0.1	56 ± 23
2010 Dec 31	INT	11	2.732	2.782	20.5	45.7	19.2 ± 0.1	13.8 ± 0.2	96 ± 42
2011 Aug 31	GN	6	3.072	3.238	18.2	95.9	24.3 ± 0.2	18.4 ± 0.2	0.0 ± 0.7
2015 Apr 26	CFHT	2	2.764	2.442	21.1	307.5	22.6 ± 0.2	17.4 ± 0.2	2.1 ± 1.2
2015 May 16	CFHT	4	2.740	2.165	19.6	312.0	22.5 ± 0.1	17.6 ± 0.2	1.5 ± 1.0
2015 May 17	CFHT	2	2.739	2.152	19.5	312.3	22.4 ± 0.1	17.6 ± 0.2	1.5 ± 1.0
2015 May 21	CFHT	3	2.735	2.101	18.0	313.2	22.3 ± 0.1	17.5 ± 0.2	1.8 ± 1.1
2015 May 23	CFHT	3	2.732	2.076	18.6	313.6	22.2 ± 0.1	17.5 ± 0.2	1.8 ± 1.1

^aTelescope. ^bNumber of exposures taken. ^cHeliocentric distance in AU. ^dGeocentric distance in AU. ^eSolar phase angle (Sun-Target-Observer) in degrees. ^fTrue anomaly in degrees. ^gApparent R-band magnitude measured with a 5'' aperture (2010 and 2011 data) and a 2'' aperture (2015 data). ^hAbsolute R-band magnitude assuming IAU H-G phase function where $G = 0.15 \pm 0.12$. ⁱEstimated dust mass in kg assuming $\rho_d \sim 2500 \text{ kg m}^{-3}$. Note: Data presented in this table represent the results of my own measurements. 2010 and 2011 datasets were previously published in Hsieh et al. (2012b), and 2015 datasets in Hsieh & Sheppard (2015).

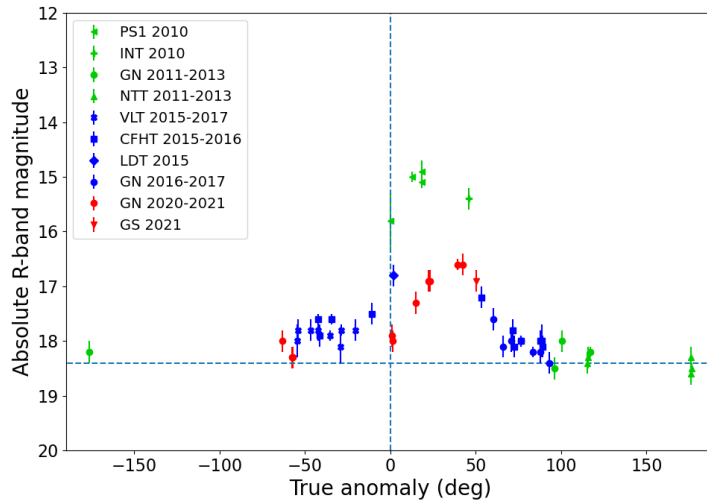


Figure 3.4: Measured absolute R-band magnitudes of 324P in a 2300 km radius aperture plotted as a function of the true anomaly. The different symbols correspond to the different telescopes and instruments, and colors mark the perihelion passages: green for 2010, blue for 2015, and red for 2021. The vertical dashed line indicates perihelion. The horizontal dashed line corresponds to the absolute magnitude of the inactive nucleus (18.4 mag). Credit: Mastropietro et al. (2024a), Figure 6.

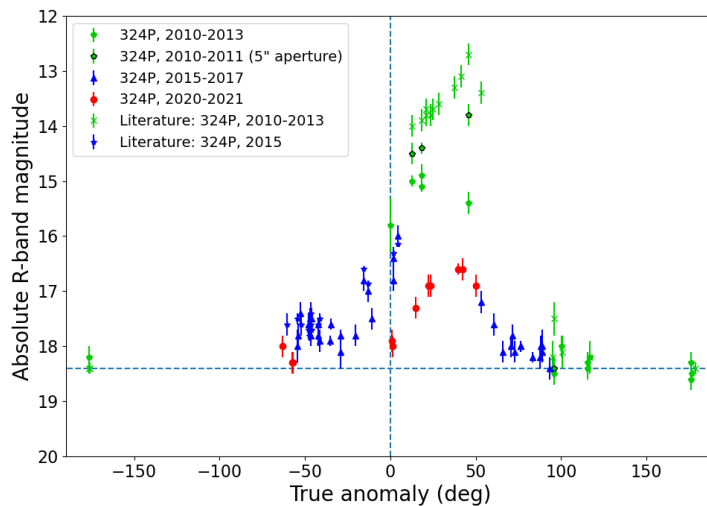


Figure 3.5: Same as Fig. 3.4, augmented by values from the literature (2010-2013: Hsieh et al. (2012b); Hsieh (2014), 2015: Hsieh & Sheppard (2015); Jewitt et al. (2016)). Symbols now distinguish between my analysis of archival data and data from the literature (see legend). Pentagonal data points with black edges were measured by us using a 5'' aperture for comparison with Hsieh et al. (2012b) (green x-symbols). Credit: Mastropietro et al. (2024a), Figure 7.

3.2.2 Photometry in infrared

In my analysis of the IR images, I measured the dust brightness within apertures of angular radii $11''$ (equivalent to 19230 km) for the W1, W2, and W3 bands, and $22''$ (38460 km) for the W4 band (Bauer et al. 2012). I selected aperture sizes that are significantly larger than the PSF full width at half maximum (FWHM) for each band. For the W1 and W2 bands, I was only able to establish upper limits.

To evaluate the detectability of coma dust in Spitzer data, I measured the FWHM of the PSF for 324P and isolated stars. The results showed that the FWHM falls between 1.5 and 2 pixels for both 324P and the stars, suggesting that any coma dust present is unresolved. The Spitzer images (Fig. 3.3) feature a densely populated field of stars. Consequently, I opted not to stack the images. Instead, I conducted circular aperture photometry on individual images with a fixed physical radius of 3000 km at the comet. To reduce the uncertainty in the measured flux, I chose small aperture sizes and carefully selected images where 324P did not overlap with nearby stars.

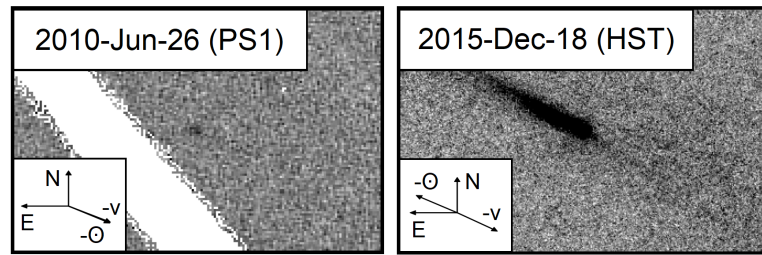


Figure 3.6: Visual light images (PS1 in z-band and HST in V-band) of 324P (at the center of each panel). Dates and directions on sky are labeled as in Fig. 3.2. These are the visual images obtained closest in time to the respective IR images shown in Fig. 3.3. Credit: Mastropietro et al. (2024a), Figure 3.

To determine the dust geometric albedo, I also calculated the brightness of 324P at visible wavelengths (Fig. 3.6) during the times of the two infrared observations (Table 3.1).

For the closest temporal reference to the WISE observations from 2010 June 9 to 11, I identified a z-band PS1 image taken on 2010 June 26. As this was the only available measurement, I used it to calculate the expected apparent magnitude of 324P during the WISE observations, based on the corresponding observing geometry. The absolute magnitude calculated from this PS1 image within a $3''$ (4847 km) aperture corresponds to an apparent z-band magnitude of (20.4 ± 1.4) mag, which equates to a flux of $0.02^{+0.04}_{-0.01}$ mJy at the time of the WISE observation. For this conversion of magnitude to flux, I first converted the Vega magnitude of the MBC (m_{Vega}) to AB magnitude (m_{AB}) using (e.g. Libanore & Kovetz 2024)

$$m_{AB} = m_{Vega} + AB_{Vega}, \quad (3.1)$$

where AB_{Vega} in z-band is 0.494 mag (Willmer 2018). Then I converted the m_{AB} to flux in Jy using

$$F = 10^{\frac{8.9 - m_{AB}}{2.5}}. \quad (3.2)$$

The closest visible light temporal reference data for the Spitzer epoch consist of four HST images taken in the F350LP filter. To account for the increasing brightness of the coma between

the individual HST observations, I extrapolated the absolute magnitudes to 2016 January 8, the date of the Spitzer measurement (Fig. 3.7), using a linear fit to the absolute magnitudes listed in Table 3.1. From this, I calculated the corresponding apparent magnitude at position of Spitzer, resulting in a value of (20.9 ± 1.2) mag. I then converted this to a flux of $0.02^{+0.03}_{-0.01}$ mJy using

$$F = 3.622 \cdot 10^{-5} \cdot 10^{\frac{20-V}{2.5}}, \quad (3.3)$$

where F represents the flux of the source in Jy, $3.622 \cdot 10^{-5}$ is the flux³ associated with a Vega magnitude of 20 in the Johnson/V filter, and V is the measured magnitude in the F350LP filter.

Tables 3.3 and 3.4 present the fluxes for the combinations of HST/Spitzer and PS1/WISE, respectively. From Table 3.4, it is also evident the fluxes for all four WISE bands are consistent with those reported by Bauer et al. (2012), who found values of < 0.01 mJy for W1, < 0.03 mJy for W2, (1.33 ± 0.07) mJy for W3, and (5.2 ± 0.5) mJy for W4.

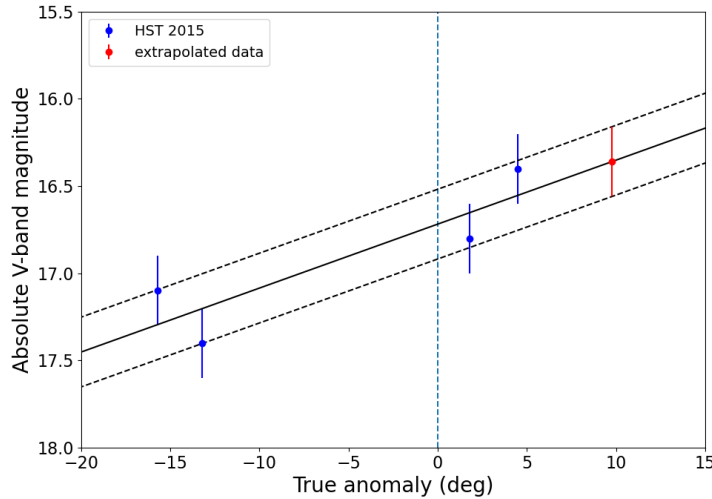


Figure 3.7: Absolute V-band magnitudes of 324P plotted as a function of the true anomaly and linear fit for extrapolation. The blue dots are HST measurements, the red one is the extrapolated value for 2016 January 8. The central solid line is the fit to the data, while the dashed lines parallel to the solid line represent the uncertainty of the linear fit. Credit: Mastropietro et al. (2024a), Figure 4.

Table 3.3: Telescope and band of observation for the HST/Spitzer combination for 2016 January 8, using 3000 km apertures throughout. Credit: Mastropietro et al. (2024a), Table 4.

Telescope:	HST	Spitzer	Spitzer
Wavelength:	0.58 μm	3.6 μm	4.5 μm
Flux (mJy):	$0.02^{+0.03}_{-0.01}$	0.0047 ± 0.0003	0.0084 ± 0.0004

³ETC Request IDs: WFC3UVIS.im.1843958, WFC3UVIS.im.1843962.

Table 3.4: Telescope and band of observation for the PS1/WISE combination for 2010 June 10, using apertures of 19230 km (W3), 38460 km (W4) and 4847 km for PS1. Credit: Mastropietro et al. (2024a), Table 5.

Telescope:	PS1	WISE	WISE	WISE	WISE
Wavelength:	0.87 μm	3.4 μm	4.6 μm	12 μm	22 μm
Flux (mJy):	$0.02^{+0.04}_{-0.01}$	< 0.02	< 0.05	1.0 ± 0.1	$4.2^{+0.7}_{-0.6}$

3.2.3 Nucleus magnitude

To determine the absolute magnitude of the bare nucleus of 324P, I focused solely on data collected in 2013, during which no activity was observed. The reduced magnitude is affected by both the solar phase angle and the rotational phase of the nucleus at the time of observation. Since the rotation rate of the 324P nucleus is unknown and the available observations are too temporally scattered to provide a constraint, I fitted the 2013 reduced magnitudes using an IAU H-G phase function. Due to a lack of adequate phase angle coverage, I assumed a default C-type value of $G = 0.15 \pm 0.12$ (Bowell et al. 1989). This fitting resulted in $H_R = (18.4 \pm 0.5)$ mag, which aligns with the value of $H_R = (18.4 \pm 0.2)$ mag reported by Hsieh (2014). The best-fit phase function is shown in Fig. 3.8. By applying Eq. (2.6), I calculated the effective radius of the nucleus, obtaining $r_N = (0.52 \pm 0.16)$ km. This result is consistent with the effective nucleus radius of $r_N = 0.59^{+0.18}_{-0.10}$ km reported in Hsieh et al. (2023), who assumed the same V-band albedo of $p_V = 0.05 \pm 0.02$.

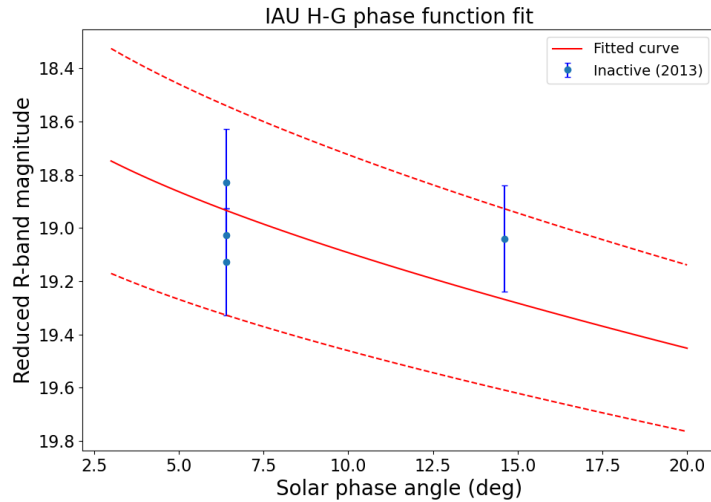


Figure 3.8: Best-fit IAU phase function (solid red line) for 324P, where dashed red lines represent the uncertainty of the fit. The blue points are 2013 data, when the nucleus was inactive, used for the fit. Credit: Mastropietro et al. (2024a), Figure 5.

Table 3.5: $Af\rho$ parameter (A’Hearn et al. 1984) for the epochs described by the first four lines of Table 3.2 from two different aperture sizes. Credit: Mastropietro et al. (2024a), Table 3.

UT Date	Telescope ^a	$Af\rho$ (for 2300 km) ^b	$Af\rho$ (for 5'') ^c
2010 Aug 16	PS1	25.3 ± 0.5	14.0 ± 1.3
2010 Sep 08	PS1	31.2 ± 2.9	18.0 ± 0.8
2010 Dec 31	INT	14.8 ± 1.4	14.8 ± 1.4
2011 Aug 31	GN	0.9 ± 0.1	0.20 ± 0.04

^aTelescope. ^b $Af\rho$ in cm measured for a 2300 km physical radius. ^c $Af\rho$ in cm measured for a 5'' angular size.

3.2.4 Aperture size dependence of dust absolute magnitudes and $Af\rho$

I compared the time evolution of the magnitudes measured in apertures of different sizes (Fig. 3.5). At $\nu = 45.7^\circ$, the brightness in the larger aperture (5'', black pentagonal symbols) has increased compared to earlier measurements, whereas the brightness in the smaller aperture (2300 km, green pentagons) has decreased. One potential explanation for this discrepancy could be the variation in geocentric distance, which influences the physical volume enclosed within a fixed-angular size aperture. At $\Delta = 1.74$ AU ($\nu = 18^\circ$), the 5'' aperture encompasses less volume than at 2.78 AU ($\nu = 45^\circ$), suggesting that the absolute magnitude of dust in a fixed-angular size aperture should decrease as the distance from the observer increases. To gain further insights into how the enclosed dust cross section depends on aperture size and time, I calculate the $Af\rho$ parameter (Table 3.5 and Fig. 3.9), which, under steady-state conditions in a spherically symmetric coma, should remain independent of aperture size. The $Af\rho$ parameter is defined as the product of the albedo A (the total light reflected by the cometary grains divided by the total light received), the filling factor f of the grains within the field of view, and ρ , the physical radius of the field of view (Fink & Rubin 2012). I used the methodology outlined by (A’Hearn et al. 1984)

$$Af\rho = \frac{(2r_h\Delta)^2}{\rho} 10^{0.4(m_{\odot,R}-m_R)}, \quad (3.4)$$

where r_h is the heliocentric distance in AU, Δ is the geocentric distance in cm, ρ is the physical radius in cm at the distance of the MBC, $m_{\odot,R} = -27.15$ is the apparent R-band magnitude of the Sun, and m_R is the measured apparent R-band magnitude of the MBC.

In panel A of Fig. 3.9, when plotting $Af\rho$ against true anomaly, it is observed that at $\nu = 45.7^\circ$, the values of $Af\rho$ are comparable for both apertures (5'' and 2300 km). This behavior is consistent with the one expected from a steady-state coma. The difference of over 1 mag shown in Fig. 3.5 can be attributed to the spatially extended nature of the dust coma, with larger apertures capturing a greater amount of dust.

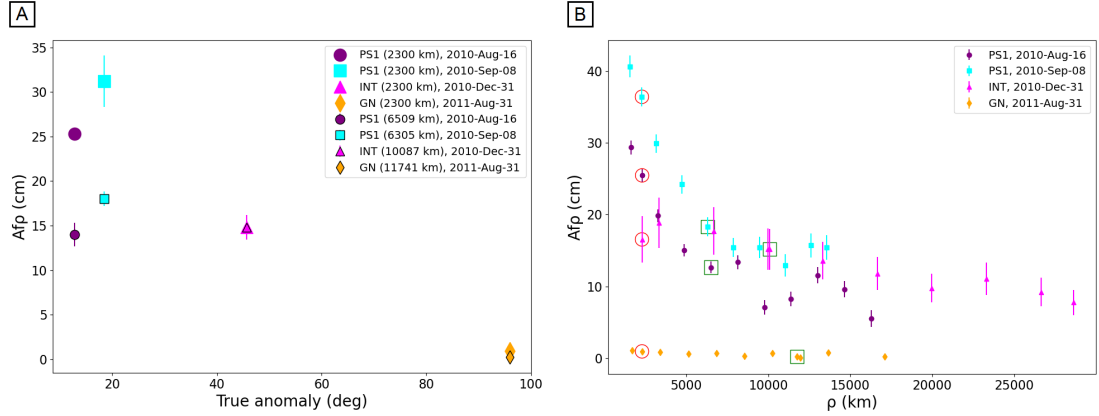


Figure 3.9: Panel A: $Af\rho$ versus true anomaly for 324P evaluated using circular apertures with physical radius of 2300 km (symbols without borders) and circular apertures with angular radius $5''$ (symbols with black borders). Panel B: $Af\rho$ versus aperture radius ρ . Data surrounded by red circles correspond to the borderless symbols of panel A ($\rho = 2300$ km), while data surrounded by green squares correspond to the black-bordered data points of panel A (angular radius of $5''$). Credit: Mastropietro et al. (2024a), Figure 8.

At true anomalies of 12.8° and 18.4° , $Af\rho$ increases as the aperture size decreases, suggesting that the dust density decreases more steeply with increasing distance from the nucleus than would be expected in a steady state. This behavior may indicate that, during this initial phase of activity, the dust production rate was still increasing with time, causing freshly emitted dust near the nucleus to be relatively more abundant compared to older dust that had traveled farther by the time of observation. Consequently, the $Af\rho$ calculated from the smaller aperture would be greater.

However, the $Af\rho$ parameter comes with certain limitations: it assumes there is no dust production or destruction (such as due to fragmentation or the sublimation of embedded ice) once the dust particles have left the nucleus; it presumes a constant outflow velocity for the dust; and it becomes ineffective at the turnaround distance (Fink & Rubin 2012). In panel B of Fig. 3.9, I present $Af\rho$ plotted against aperture radius ρ across four different epochs. The plot demonstrates a decrease in $Af\rho$ with increasing aperture size during the active phase of 324P in August and September 2010. By the end of December 2010, the profile is noticeably shallower, and in August, it appears flat with values close to zero.

The flattening of the $Af\rho$ profile at sufficiently large aperture radii during the initial two epochs may indicate that, at an even earlier time, the coma was closer to a steady-state regime than during the observed periods. This aligns with Fig. 3.4, which displays a flat profile of absolute coma magnitudes up to a true anomaly of approximately 20° , followed by a steep increase thereafter.

In panel B of Fig. 3.9, the $Af\rho$ parameter shows strong fluctuations at larger values of ρ , which are likely caused by a more variable background flux as the aperture size increases. However, these fluctuations occur only beyond aperture radii of $5''$, so they are not expected to have a significant impact on the interpretation of panel A of Fig. 3.9.

3.2.5 Dust mass estimates and onset of activity

I calculated the dust mass within the aperture following the methodology outlined by (e.g. Hsieh & Sheppard 2015).

$$M_d = \frac{4}{3}\pi r_N^2 a \rho_d \left(\frac{1 - 10^{0.4(H_R - H_{R,inactive})}}{10^{0.4(H_R - H_{R,inactive})}} \right), \quad (3.5)$$

where $r_N = 0.52$ km is the estimated effective nucleus radius for 324P (Sect. 3.2.3), $a = 0.5$ mm⁴ is the assumed effective mean dust grain radius, $\rho_d = 2500$ kg m⁻³ is the assumed dust grain density (C-type objects), and $H_{R,inactive} = (18.4 \pm 0.5)$ mag is the absolute magnitude of the inactive nucleus of 324P in R-band (Sect. 3.2.3). I present the estimated dust masses as a function of the true anomaly in Fig. 3.10. The figure indicates that the MBC becomes active around the perihelion, implying that this activity is likely a result of sublimation. The outcomes of the photometric analysis are summarized in Table 3.1. Three of the dust mass values are negative, yet they remain consistent with zero when considering the associated uncertainties.

By employing a linear fit to the absolute magnitude over time, Hsieh & Sheppard (2015) determined that the average net dust production rate (\dot{M}_d) for 324P in 2015 was $\lesssim 0.1$ kg s⁻¹ ($-60.4^\circ < \nu < -41.4^\circ$). This rate is nearly two orders of magnitude lower than the net dust production rate of approximately 30 kg s⁻¹ ($12.9^\circ < \nu < 45.9^\circ$) recorded in 2010 by Hsieh (2014). These dust production rates documented in the literature were obtained at different orbital positions and measured with rectangular apertures to capture the total visible flux, including contributions from the coma and tail.

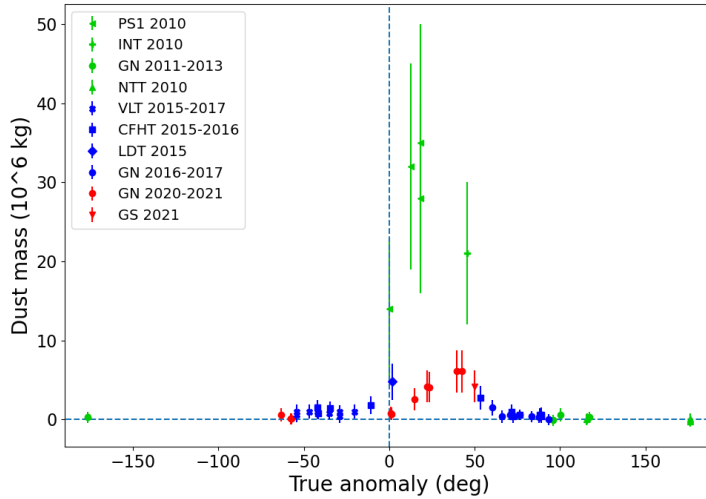


Figure 3.10: Estimated dust masses for 324P plotted as a function of the true anomaly. The different symbols correspond to the different telescopes and instruments used, and the different colors correspond to the three different perihelion passages: green for 2010, blue for 2015, and red for 2021. The horizontal dashed line corresponds to zero dust mass (the MBC was not active). Credit: Mastropietro et al. (2024a), Figure 9.

In this study, the linear fitting method was not suitable because the dust measurements showed nearly constant values (Fig. 3.11). Assuming that dust particles are ejected from 324P at a speed

⁴In Mastropietro et al. (2024a), a dust grain radius of $a = 1$ mm was used. Here, I chose $a = 0.5$ mm to align with Sect. 3.3.2, where the large dust particles ejected from 324P were calculated to range from 0.2 mm to 0.8 mm. The mean value of 0.5 mm was selected as a representative estimate for this analysis.

close to the gravitational escape speed of the nucleus, which is $v_{escape} = 0.61 \text{ m s}^{-1}$ (calculated based on the estimated nucleus size and assumed bulk density), these particles would exit the 2300 km aperture after approximately 43 days. The gravitational escape speed of the nucleus is calculated using (Dalarsson et al. 2011)

$$v_{escape} = \sqrt{\frac{2GM_{nucleus}}{r}}, \quad (3.6)$$

where $G = 6.67 \cdot 10^{-11} \text{ m}^3 \text{ kg}^{-1} \text{ s}^{-2}$ is the gravitational constant, the mass of the nucleus is given by $M_{nucleus} = \rho * V$ in kg, considering its density as $\rho = 2500 \text{ kg m}^{-3}$ and its volume as $V = (4/3)\pi r^3$ in m^3 , and $r = 0.52 \text{ km}$ is the nucleus radius (Sect. 3.2.3).

The data points shown in Fig. 3.11 were collected over several hundred days, indicating that the earliest ejected dust has likely already left the measurement aperture during most observation periods. As a result, the nearly stable dust mass implies that the rate of dust production from 324P may be approximately equal to the rate of dust loss from the aperture.

For the 2015 perihelion, I deduced that the activity began earlier than 173 days before perihelion, as the image in Fig. 3.2 reveals a visible tail on 2015 June 10 (marked in Fig. 3.11). However, using the same criteria, I was unable to determine the onset time for the 2021 perihelion passage because the 2020 data in Fig. 3.2 do not show any visible tail.

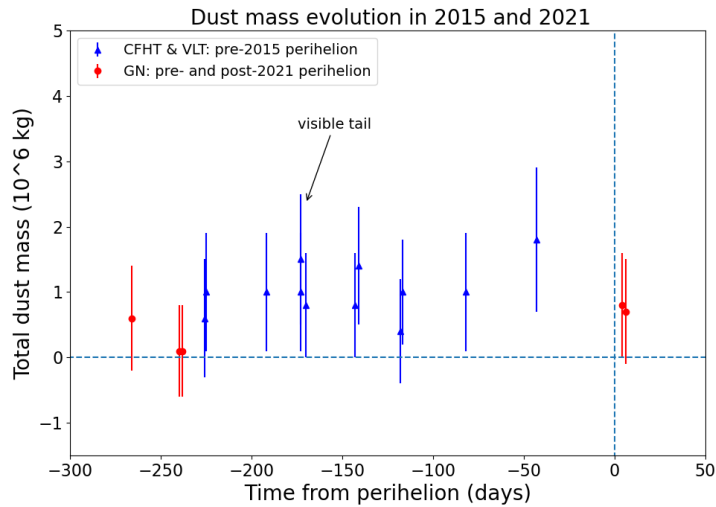


Figure 3.11: Estimated dust masses around 324P plotted versus time from perihelion. Pre-perihelion data in 2015 (blue) and pre- and post-perihelion data in 2021 (red). Marked in the plot is the epoch when the tail starts to become visible. Credit: Mastropietro et al. (2024a), Figure 10.

In Fig. 3.5, around $\nu = 120^\circ$, the absolute magnitude stabilizes at approximately 18.4 mag in the R-band, which aligns with the calculated magnitude for the inactive nucleus (Sect. 3.2.3). This stabilization suggests that dust production has stopped and that the dust has dispersed from the vicinity of the nucleus as a result of solar radiation pressure (in 2011).

Fig. 3.5 shows a steep increase in brightness around perihelion and shortly thereafter. To identify the onset of this steepening, I applied a linear fit to the post-perihelion dust masses. I determined the onset times of the profile steepening as follows: 34 to 81 days before perihelion in 2010, with a mass loss rate of $(2.8 \pm 0.7) \text{ kg s}^{-1}$ ($0.0^\circ < \nu < 18.4^\circ$); 6 days before perihelion in 2015, with a mass loss rate of $(5.3 \pm 2.3) \text{ kg s}^{-1}$ ($1.8^\circ < \nu < 4.5^\circ$); and between 24 days

before perihelion and 8 days after perihelion in 2021, with a mass loss rate of $(0.4 \pm 0.2) \text{ kg s}^{-1}$ ($1.0^\circ < \nu < 23.4^\circ$) (Fig. 3.12). This pronounced increase in activity is likely reflected in the $Af\rho$ profiles, as discussed in Sect. 3.2.4. It may be attributed to the thermal wave reaching the sub-surface layer rich in ice, or the seasonal exposure of the ice reservoir that was not accessible to sunlight before perihelion.

In the study conducted by Hui & Jewitt (2017), data collected from 2010 to 2015 showed that 324P exhibited nongravitational accelerations attributed to recoil forces resulting from anisotropic mass loss, with dynamically inferred mass loss rates of $(36 \pm 3) \text{ kg s}^{-1}$. This value is consistent with the results obtained by Hsieh (2014) in 2010, who used a dust grain radius of $a = 1 \text{ mm}$ in the dust mass calculations. However, my analysis of the 2010 data indicates mass loss rates that are one order of magnitude smaller, a discrepancy discussed in Sect. 3.2.1 that may be due to advancements in all-sky photometric catalogs. Furthermore, my calculated mass loss rate is in agreement with the findings of Moreno et al. (2011), who reported a rate of $3 - 4 \text{ kg s}^{-1}$ between October 2010 and January 2011 ($26.5^\circ < \nu < 47.8^\circ$).

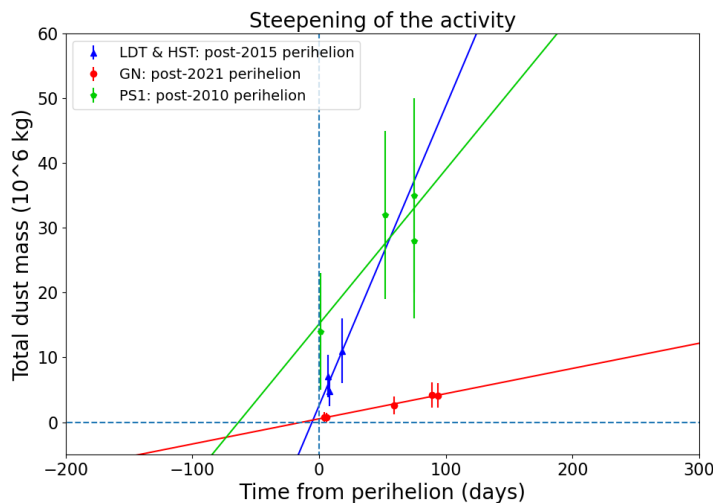


Figure 3.12: Estimated dust masses around 324P plotted versus time from perihelion. The dashed lines show linear fits to post-perihelion data from 2010 (green), 2015 (blue) and 2021 (red), that were used to calculate the onset time of the steepening of the activity. Credit: Mastropietro et al. (2024a), Figure 11.

Figs. 3.5 and 3.10 provide visual evidence that the activity of 324P during the 2015 perihelion passage was significantly lower than during the previous passage in 2010. Additionally, the activity observed in 2021 has declined further compared to 2015. One potential explanation for the sharp reduction in activity observed in 2015, relative to 2010, followed by a gradual decrease in 2021, could be the accumulation of a dry mantle and/or volatile depletion. However, further data from future perihelion passages will be necessary to support this hypothesis.

3.2.6 Spectral energy distribution

The spectral energy distribution (SED) (Williams et al. 1997; Kolokolova et al. 2004; Yang et al. 2009) is formed from the combination of scattered sunlight and thermal emission from the dust. By analyzing the shape of the thermal SED, the dust temperature can first be determined, followed by the product of the dust cross section and emissivity. Lastly, the scattered light component provides the product of the geometric albedo and phase function divided by the emissivity at the time when the cometary grains are observed.

I derived the dust color temperature by equating the flux ratio in WISE W4/W3 bands to the ratio of the Planck function at these wavelengths, $B_\nu(22 \mu\text{m}, T) / B_\nu(12 \mu\text{m}, T)$, treating the temperature T_{col} as a free parameter. This resulted in $T_{col,WISE} = 167^{+13}_{-11}$ K. This temperature range comprises the equilibrium temperature of a fast-rotating sphere with isothermal surface, which is $T_{eq} = 172$ K, measured at the heliocentric distance of $r_h = 2.623$ AU during the WISE observation, calculated using (e.g. Agarwal et al. 2010)

$$T_{eq}(r_h, A_B, \varepsilon) = 278.8 \left(\frac{1 - A_B}{\varepsilon} \right)^{\frac{1}{4}} \frac{1}{\sqrt{r_h}}, \quad (3.7)$$

where A_B is the Bond albedo, assumed to be 0, ε is the emissivity, assumed to be 1, and r_h is the heliocentric distance in AU.

This same approach was ineffective for the Spitzer data. By calculating the dust color temperature from the flux ratio in Spitzer channels 2 and 1, and equating it to the ratio of the Planck function at these wavelengths, $B_\nu(4.5 \mu\text{m}, T) / B_\nu(3.6 \mu\text{m}, T)$ as a function of temperature, I obtained $T_{col,Spitzer} = 624.5^{+62.5}_{-47.0}$ K. This result is likely influenced by the residual scattered light at shorter wavelengths. Consequently, I decided to adopt the temperature $T_{col} = T_{col,WISE}$ for both analyses.

There is no strong evidence of dust superheating⁵ at mid-infrared (mid-IR) wavelengths, suggesting that the dust comprises compact or large particles, or a combination of both (Gehrz & Ney 1992). However, color temperatures reaching up to 8% above T_{eq} are still consistent with the WISE measurements.

To fit the combined SED of scattered light and thermal emission to the PS1 and WISE data, I scaled the Planck function, B_ν , using a freely variable factor f_{IR} , and the solar spectrum⁶ with another freely variable factor f_{vis} . This approach ensures that the sum of these components aligns with the measured fluxes.

From Eq. (2.8), the scaling factor (in units of sr) f_{IR} is equal to

$$f_{IR}(T_{col}) = \frac{\varepsilon S(T_{col})}{\Delta^2}. \quad (3.8)$$

The parameter S is implicitly dependent on the color temperature for a specific measured flux F_{IR} due to the temperature dependence of $B_\nu(T)$ in Eq. (2.8). From Eq. (2.9), the dimensionless scaling factor for the scattering component is equal to

$$f_{vis} = \frac{p j(\alpha) S}{(r_h/1\text{AU})^2 \pi \Delta^2}, \quad (3.9)$$

⁵Dust is significantly hotter than its equilibrium temperature.

⁶<https://www.nrel.gov/grid/solar-resource/spectra.html>, F_\odot , the Thekaekara Spectrum.

such that

$$\frac{pj(\alpha)}{\varepsilon} = \pi(r_h/1\text{AU})^2 \frac{f_{vis}}{f_{IR}}, \quad (3.10)$$

assuming that the quantity of dust observed in paired images is the same, regardless of variations in the PSF, aperture sizes, or observation dates.

The maximum scaling factor, f_{IR}^{max} corresponds to the minimum possible color temperature, while the opposite is true for the minimum scaling factor. The minimum and maximum values for f_{vis} are determined by fitting the solar spectrum to the lower and upper bounds of the PS1 measurement error bars. Substituting these values into Eq. (3.10), I obtain $pj(\alpha) = 0.03^{+0.12}_{-0.02}$. This corresponds to a range of $3\% < p < 45\%$ for a C-type asteroid ($G = 0.15 \pm 0.12$), and $2\% < p < 40\%$ for an S-type ($G = 0.25 \pm 0.12$). Since this range comprises all typical values observed for both C- and S-types, there is no meaningful constraint on the geometric albedo or the spectral type of the dust. The large uncertainties in the albedo calculations arise from the wide temperatures range of the mid-IR data, alongside the large uncertainties in optical wavelength photometry.

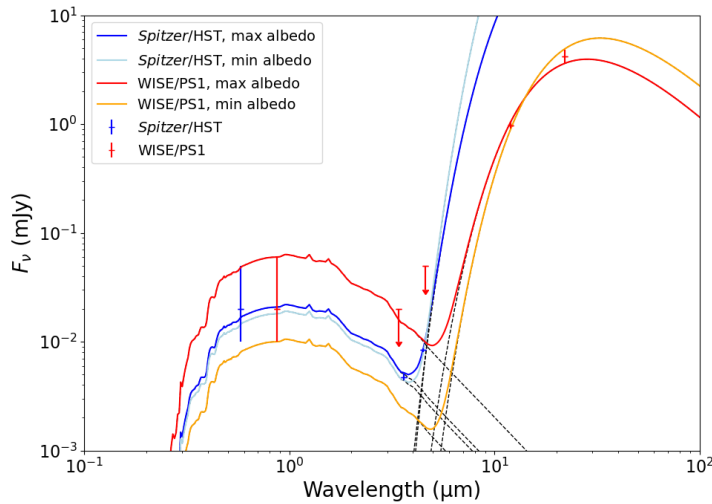


Figure 3.13: SEDs corresponding to the maximum (red) and minimum (yellow) derived geometric albedo values from both the WISE/PS1 (red) and Spitzer/HST (blue) combination. Even though taken during different perihelion passages and from different observer distances, I plot the measurements and resulting fits into a single graph. Dashed lines indicate the pure blackbody and solar spectra composing the overall SED. Credit: Mastropietro et al. (2024a), Figure 12 (adapted).

Fig. 3.13 displays the minimum and maximum geometric albedo SEDs derived from the WISE/PS1 dataset, along with these measurements, as well as the Spitzer and the extrapolated HST data (with flux values listed in Tables 3.3 and 3.4). The Spitzer/HST data were obtained during a different perihelion passage, at a time when the overall dust brightness was lower than in 2010 (cf. Fig. 3.5), and from a different observer distance, but at very similar heliocentric distance, phase angle and true anomaly. All six data points are presented in a single graph for several reasons: (1) The comparable visible light fluxes from PS1 and HST suggest that the overall amount of dust, adjusted for Δ^2 , was very similar during both observations; (2) The similar heliocentric distances imply that the range of color temperatures during both measurements

was likely similar; (3) The comparison with the WISE SEDs can provide valuable insights for interpreting the Spitzer data.

The plot indicates that the longer of the two IRAC wavelengths falls within the overlapping region where both scattered light and thermal emission can play a substantial role in the total flux. In contrast, the flux recorded at the shorter wavelength is likely dominated by scattered light, making it impossible to obtain an independent measurement of the color temperature from the IRAC data. Given that the heliocentric distances during both measurements were similar, I therefore assume that the range of color temperatures derived from the WISE dataset is also applicable to the Spitzer data.

The visible light scaling factor f_{vis} is primarily determined by the Spitzer 3.6 μm channel, and the result aligns with the extrapolated HST measurement. Next, I calculate the infrared scaling factor by fitting the 4.5 μm data point to the sum of the scaled solar spectrum and the scaled blackbody spectrum, expressed as $f_{vis}F_{\odot} + f_{IR}B_{\nu}(T)_{col}$. In this process, I again combine the highest color temperature blackbody spectrum (which corresponds to the lowest dust cross section) with the brightest visible spectrum to derive the upper limit for geometric albedo, and vice versa. This fitting yields $0.0002 < p_j(\alpha) < 0.003$, which is inconsistent measurements obtained from WISE/PS1.

Since the amount of scattered light and the phase angle were nearly identical during both observations, it is reasonable to assume that the dust cross section at those times was also similar. Additionally, with the heliocentric distances being very comparable, the assumption of similar color temperatures appears to be justified.

The dust brightness observed in the 4.5 μm IRAC measurement is inconsistent with the simplistic approach of modeling thermal emission using a single blackbody function. One potential explanation for the elevated flux at 4.5 μm could be superheating, since small or porous dust particles may not be able to efficiently radiate thermally at shorter wavelengths. Additionally, the excess brightness in the IRAC 4.5 μm band has been interpreted as a possible indicator of CO or CO₂ vapor presence (Ootsubo et al. 2011), which cannot be completely ruled out. However, the measured ratio of $F(4.5 \mu\text{m} / 3.6 \mu\text{m}) = 1.8$ at $r_h = 2.625$ AU is close to the lower limit reported for 23 comets by Reach et al. (2013), where a low ratio value correlates with a lack of PSF broadening due to a spatially extended gas coma. There is also no indication of an extended coma in my analysis, which further weakens the interpretation of the excess flux at 4.5 μm as being due to CO or CO₂ emission. Additionally, depletion of CO₂ relative to water was also observed in the MBC 238P by JWST (Kelley et al. 2023).

3.3 Dust tail analysis

3.3.1 Dust tail brightness profile

Here are the results from the steps described in Sect. 2.3. The selected images for the *Image Selection* and *Composite Image Creation* steps are displayed in Fig. 3.14, where the clearly visible tails can be observed. In Table 3.6 I specify the exposure time and number of images combined.

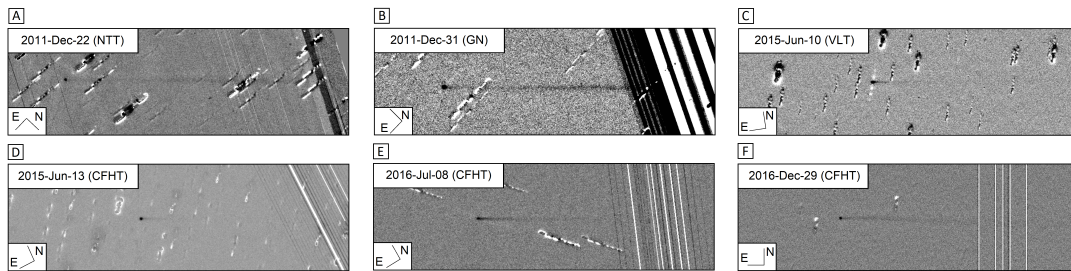


Figure 3.14: Mosaic of the composite R-band images of the tail of 324P. All panels have north (*N*) and east (*E*) direction, as projected on the sky, marked. Panels are labeled with dates of observation in UT YYYY-MM-DD format, and employed telescope.

Table 3.6: Tail combined images of the MBC 324P.

UT Date	Telescope ^a	Exposure ^b	N ^c
2011 Dec 22	NTT	500	4
2011 Dec 31	GN	180	9
2015 Jun 10	VLT	50	18
2015 Jun 13	CFHT	180	9
2016 Jul 08	CFHT	180	6
2016 Dec 29	CFHT	180	5

^aTelescope. ^bExposure time in seconds.

^cNumber of images combined.

Below are the surface brightness profiles that I derived using the equations outlined in Sect. 2.3.

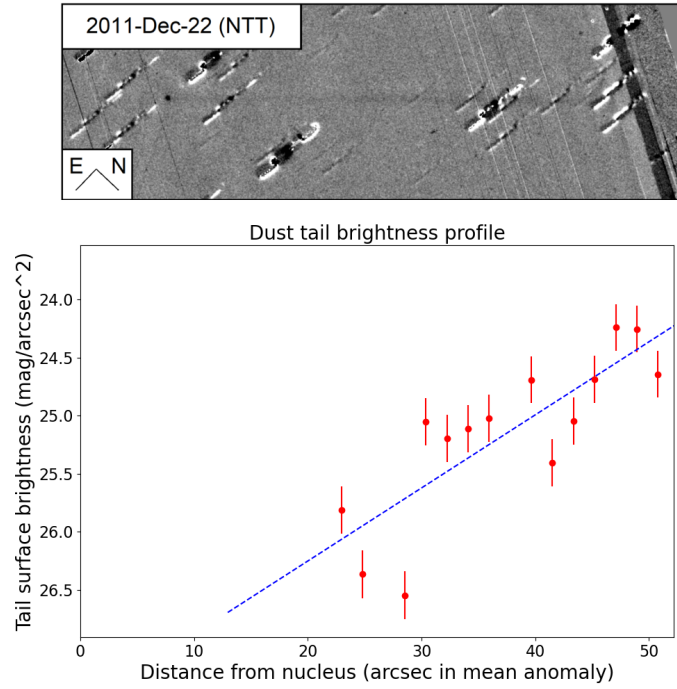


Figure 3.15: Panel A of Fig. 3.14 and the corresponding dust tail brightness profile.

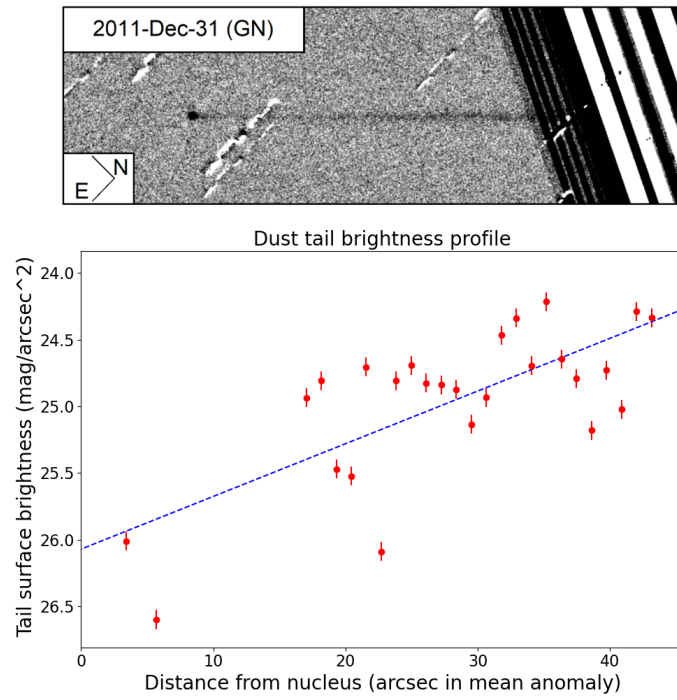


Figure 3.16: Panel B of Fig. 3.14 and the corresponding dust tail brightness profile.

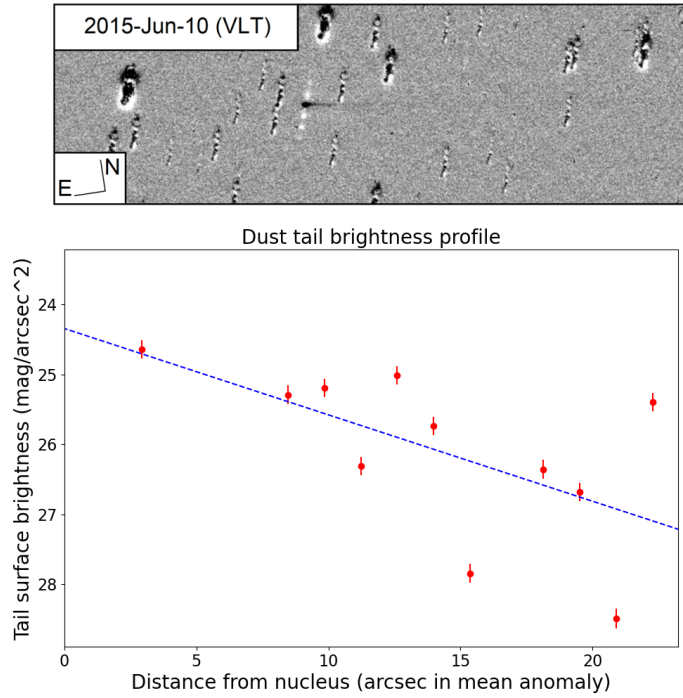


Figure 3.17: Panel C of Fig. 3.14 and the corresponding dust tail brightness profile.

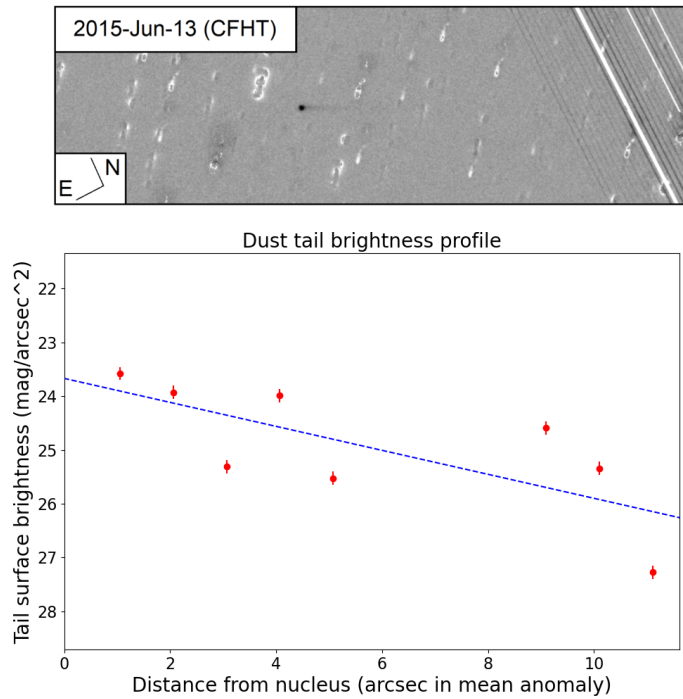


Figure 3.18: Panel D of Fig. 3.14 and the corresponding dust tail brightness profile.

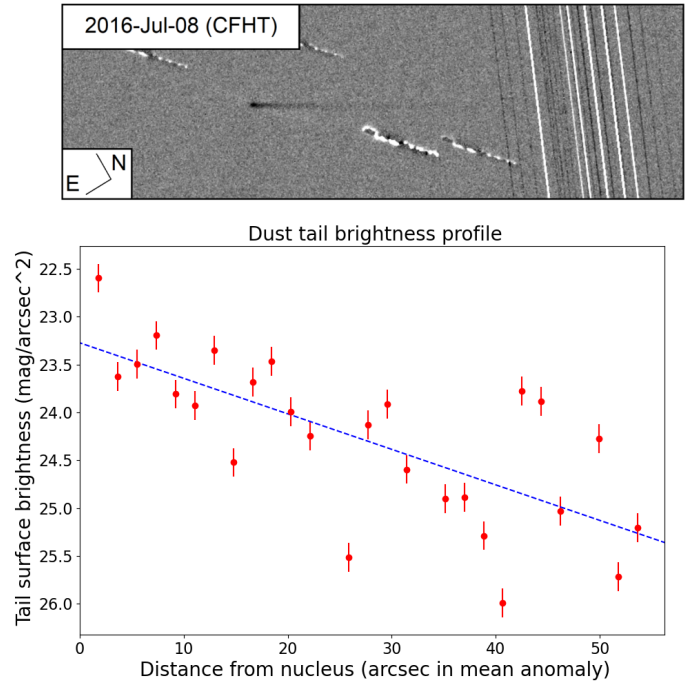


Figure 3.19: Panel E of Fig. 3.14 and the corresponding dust tail brightness profile.

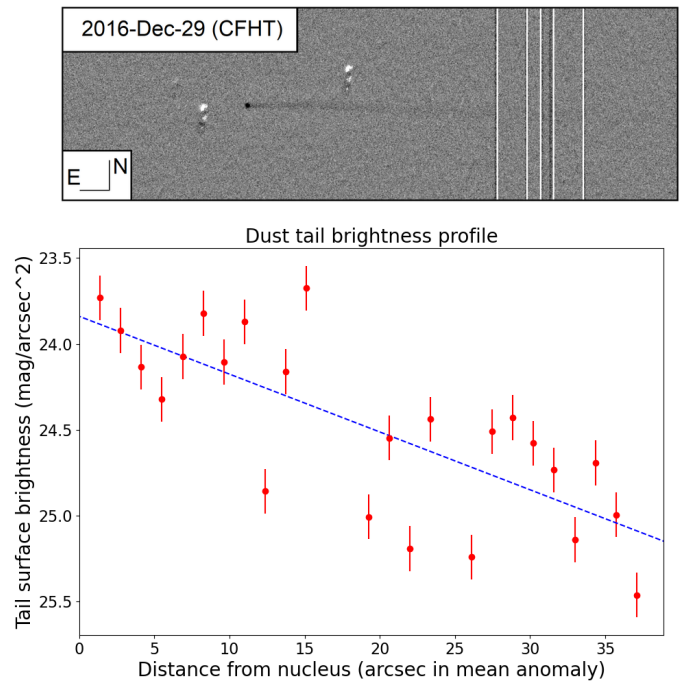


Figure 3.20: Panel F of Fig. 3.14 and the corresponding dust tail brightness profile.

This study examines the brightness profiles of the tail of 324P during different activity phases, specifically contrasting observations from 2011 (panels A and B of Fig. 3.14) with those from 2015 and 2016 (panels C – F of Fig. 3.14). In the first scenario, observed in 2011, the plots in Figs. 3.15, and 3.16 show a negative slope in the brightness profile—indicating that the tail is brighter at greater distances from the nucleus. This behavior can be attributed to the MBC being in an inactive state, during which dust production has ceased. In this scenario, smaller dust grains are more significantly influenced by solar radiation pressure, causing them to be pushed away from the vicinity of the nucleus and leading to higher brightness at greater distances from the nucleus. Conversely, larger dust particles, released during the previous active phases of the MBC, are less affected by solar radiation pressure and tend to remain closer to the nucleus. This results in lower brightness in the immediate vicinity of the nucleus due to a reduced presence of smaller dust particles with large total cross section. In the second case instead, recorded in 2015 and 2016, the brightness of the tail decreases with distance from the nucleus, indicating a positive slope in the magnitude profile (Figs. 3.17, 3.18, 3.19, and 3.20). This phenomenon is characteristic of active phases, where a sustained production of dust particles contributes to large dust cross section near the nucleus.

Fig. 3.21 illustrates the temporal evolution of the dust brightness profile, plotting the slope of the brightness profile against true anomaly and depicting the characteristics of dust distribution. In 2011, the negative slope confirms the inactivity of 324P, while a marked transition to positive slope values is evident in 2015 and 2016, paralleling the period of increased activity.

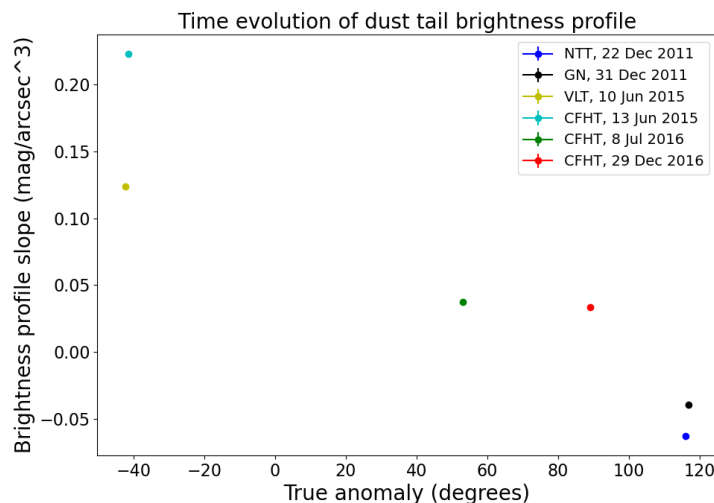


Figure 3.21: Time evolution of dust tail brightness profile illustrating the slopes of the six different tail analyses vs. the true anomaly.

3.3.2 Comparison of the synchrones ages

I employed the syndyne-synchrone model (Sect. 2.4.2) to analyze the image from 2011 December 31, which exhibited a noticeable gap in the dust tail (panel B of Fig. 3.14). To facilitate a comparison between the observational data and model predictions, I quantified the length of the gap as 0.006° and the angular extents of the dust tail relative to the x-axis, which were 18.4° (minimum), 19.2° (middle), and 20.0° (maximum) (illustrated in Fig. 3.22). To derive the ejection times and particle sizes, I used the output of the model for the particle positions. I manually examined the simulations of the model and identified the synchrones at the three specific angles of interest. From this, I determined the corresponding ejection times, as each synchrone is associated with a specific emission time. Regarding particle size, I inferred that smaller particles, which follow more elongated orbits, would be located farther from the nucleus, while larger particles, which follow more circular orbits, would be closer to the nucleus. This relationship between particle size and distance from the nucleus allowed me to determine the size of the particles at each given location along the dust tail. Specifically, for the three synchrones identified earlier, I selected the particles with the corresponding β parameters that were located 0.006° from the nucleus, at the end of the gap. From the value of β , and using Eq. 2.16, was able to calculate the particle size.

The model simulations indicated that large dust particles, with sizes ranging from 0.2 mm to 0.8 mm, were ejected over a three-month timeframe. Specifically, during the emission events (measured in days before the observation on 2011 December 31), the following parameters were noted: At $T_{emiss,1} = 204$ days (2011 June 10, $\nu_1 = 80.3^\circ$ and $r_{h,1} = 2.948$ AU), a particle size of 0.2 mm was associated with a parameter $\beta_1 = 0.0011$; at $T_{emiss,2} = 240$ days (2011 May 5, $\nu_2 = 73.0^\circ$ and $r_{h,2} = 2.894$ AU), the model indicated a particle size of 0.4 mm corresponded to $\beta_2 = 0.0006$; and at $T_{emiss,3} = 295$ days (2011 March 11, $\nu_3 = 61.4^\circ$ and $r_{h,3} = 2.818$ AU), a size of 0.8 mm was linked to $\beta_3 = 0.0003$ (Fig. 3.23).

I conducted a comparative analysis of the three synchrone ages in relation to the activity profile of 324P (Fig. 3.24). The results of this comparison indicate that the observed particles were not released during the peak activity phase immediately following perihelion. Instead, it appears that these particles were likely emitted in the post-perihelion period, corresponding to a time when the activity of the MBC had substantially diminished.

324P showed a gap in the tail also in the 2011 December 22 image (panel A of Fig. 3.14) and 23 (omitted here due to contamination from background stars). However in the night between December 22 and 23, the orbit plane angle shifted from negative to positive. This caused all the synchrones to overlap, leading to a degenerate situation where the syndyne-synchrone model produced unclear or confusing results. By contrast, on December 31, the orbit plane angle had increased to 1.3° , offering a clearer perspective. Therefore, I chose to concentrate exclusively on the December 31 image for the syndyne-synchrone analysis.

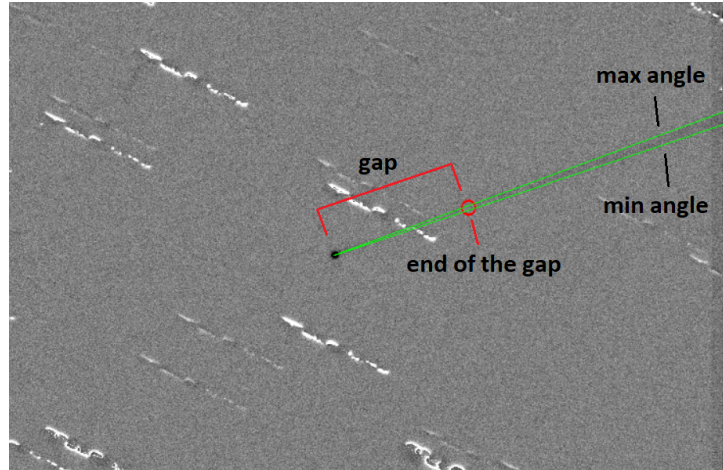


Figure 3.22: Image of 324P on 2011 December 31, showing the length of the gap, its end, and the minimum and maximum angular extents of the dust tail relative to the x-axis.

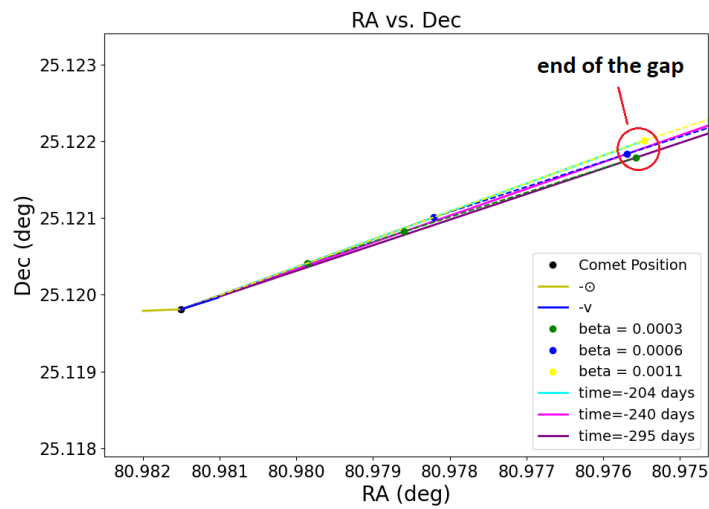


Figure 3.23: Right ascension vs. declination plot showing the result of the syndyne-synchrone model on the 2011 December 31 image. The legend follows the format of Fig. 2.3. Marked is the end of the gap, as in Fig. 3.22.

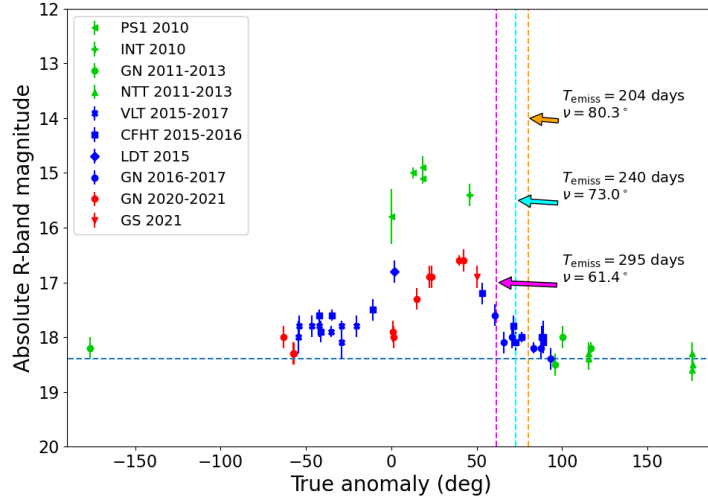


Figure 3.24: Synchronic ages with the respective true anomalies, and the activity profile of 324P, as in Fig. 3.4.

3.3.3 Gas production rate

Using the Small Source Approximation (SSA)⁷ as described in Jewitt et al. (2014b), I estimated the gas mass loss rate by knowing the size of the largest particles that the gas drag could effectively lift, which was derived from the results of the syndyne-synchronic model.

Before diving into the energy balance equation, let us first define the important quantities involved:

- A_B is the bolometric Bond albedo assumed to be 0;
- I_{eff} is the effective irradiation equal to $\frac{1361}{r_h^2}$ in W m^{-2} at heliocentric distances $r_{h,1} = 2.948$ AU and $r_{h,2} = 2.894$ AU (the heliocentric distances 324P would have had at $\nu_1 = 80.3^\circ$ and $\nu_3 = 61.4^\circ$, Fig. 3.24 in Sect. 3.3.2);
- ϵ is the emissivity, assumed to be one;
- $\sigma = 5.67 \cdot 10^{-8} \text{ W m}^{-2} \text{ K}^{-4}$ is the Stefan-Boltzmann constant;
- $T_1 = 162 \text{ K}$ and $T_2 = 166 \text{ K}$ are the surface temperatures at $r_{h,1}$ and $r_{h,2}$, calculated using Eq. (3.7);
- F_s is the equilibrium sublimation mass flux in $\text{kg m}^{-2} \text{ s}^{-1}$, which represents the amount of ice transitioning to vapor on the surface of the comet under equilibrium conditions;
- $H = 2.84 \cdot 10^6 \text{ W s kg}^{-1}$ is the latent sublimation heat of H_2O (Huebner et al. 2006).

Now, assuming a simple energy balance between the absorbed solar energy and the energy used for sublimation and radiative cooling, we can write the following equation (Skorov et al.

⁷The SSA is a simplified modeling approach used to describe the outgassing of materials from the nucleus of a comet. The approximation treats the nucleus as a small point source of gas emission, simplifying the complex details of the surface of the nucleus and internal structure.

2020)

$$(1 - A_B)I_{eff} = \epsilon\sigma T^4 + F_s H, \quad (3.11)$$

where the left-hand side represents the absorbed solar energy and the right-hand side accounts for the thermal radiation emitted by the surface of the comet and the energy required for sublimation of water ice. From this, I found the $F_s = 4 \cdot 10^{-5} \text{ kg m}^{-2} \text{ s}^{-1}$ using both T_1 and T_2 .

Next, I calculated the radius of sublimating surface (r_s) in meters from the following equation (Jewitt et al. 2014b)

$$a_c = \frac{9C_D V_g F_s r_s}{32\pi G \rho_n \rho r_n^2}, \quad (3.12)$$

where a_c represents the maximum liftable particle size found from the syndyne-synchrone model results (Sect. 3.3.2) in meters, the dimensionless gas drag coefficient $C_D = 1$ reflects the nature and shape of the dust grains, $V_g = 500 \text{ m s}^{-1}$ is the thermal speed of gas molecules (Jewitt et al. 2014b), F_s is the equilibrium sublimation mass flux previously calculated, $G = 6.67 \cdot 10^{-11} \text{ m}^3 \text{ kg}^{-1} \text{ s}^{-2}$ is the gravitational constant, ρ_n and ρ are the densities of the nucleus and of the dust particles, respectively, assumed to be both equal to 2500 kg m^{-3} , and $r_n = 520 \text{ m}$ is the nucleus radius (Sect. 3.2.3).

Finally, I calculated the gas mass loss rate ($\frac{dM_g}{dt}$) from (Jewitt et al. 2014b)

$$\pi r_s^2 = \frac{1}{F_s} \frac{dM_g}{dt}. \quad (3.13)$$

This analysis, conducted with a_c values ranging from 0.2 mm to 0.8 mm, produced gas mass loss rate $\frac{dM_g}{dt}$ between 0.02 kg s^{-1} and 0.32 kg s^{-1} . These rates correspond to estimated gas production rates for 324P of approximately $6.7 \cdot 10^{23} \text{ molecules s}^{-1}$ and $1.1 \cdot 10^{25} \text{ molecules s}^{-1}$. The conversion process involved converting the mass loss rates to grams per second, calculating the mass flow in moles per second using the molar mass of water (18 g/mol), and multiplying by Avogadro's number ($N_A = 6.022 \cdot 10^{23} \text{ mol}^{-1}$) to determine the number of molecules per second (Flowers et al. 2019).

These findings for 324P, at true anomalies between 61° and 80° , are consistent with the gas production rates observed in other MBCs, as detailed in Table 3.7.

I chose to not include the error bars for both the nucleus radius and temperature due to uncertainties in all the other variables involved in the analysis. Since each of these variables carries its own uncertainties, including error bars for the radius and temperature could be misleading and may not accurately reflect the overall uncertainty in the calculations. The key sources of uncertainty in this analysis are as follows:

- Thermal speed of gas molecules (V_g) and densities (ρ_n, ρ): These values are assumed rather than directly measured, and their assumed nature introduces considerable uncertainty into the results. Variations in these parameters significantly affect the derived gas mass loss rates, making them among the largest contributors to the overall error.
- Nucleus radius (r_n): Although its uncertainty (0.16 m) is relatively small, the radius directly impacts the calculations, and this error propagates into the final results.
- Maximum liftable particle size (a_c): This value is derived from measurements of angles in the image and is reflected in the syndyne-synchrone model output. The accuracy of a_c is therefore dependent on the precision of these manually measured angles. Any errors in identifying or interpreting these angles will propagate into the determination of a_c , further affecting the results.

- Drag coefficient (C_D): This is a standard value (assumed to be 1) for compact and spherical particles, it is unmeasured and might impact on the overall uncertainty.
- Sublimation flux (F_s): Although F_s is sensitive to temperature, the flux did not vary significantly with the temperatures calculated at the two heliocentric distances used. Since F_s is related to the heliocentric distance, and 324P was at a specific heliocentric distance during the observation, this parameter introduces less uncertainty relative to the others.

Table 3.7: Gas production rates for different MBCs.

MBC ^a	ν^b	$Q_{\text{H}_2\text{O}}^c$	Reference ^d
324P/La Sagra	30°	$< 10^{26}$	(Hsieh et al. 2012b)
288P (2006 VW139)	40°	$< 10^{26}$	(Hsieh et al. 2012a)
133P/Elst-Pizarro	0°	$< 1.3 \cdot 10^{24}$	(Licandro et al. 2011)
259P/Garradd	30°	$< 1.4 \cdot 10^{26}$	(Jewitt et al. 2009)
176P/LINEAR	0°	$< 4 \cdot 10^{25}$	(de Val-Borro et al. 2012)
176P/LINEAR	20°	$< 2.3 \cdot 10^{24}$	(Hsieh et al. 2011)
238P/Read	28.3°	$(9.9 \pm 1.0) \cdot 10^{24}$	(Kelley et al. 2023)

^aMBCs. ^bTrue anomaly in degrees. ^cGas production rates in molecules per seconds.

^dReferences.

3.3.4 Size distribution of particles

To further understand the behavior of the dust in 324P, I focused on the image taken on 2011 December 31 and performed flux measurements once more using rectangular apertures measuring 40 pixels by 18 pixels, as outlined in Sect. 2.3. I calculated the dust cross section in each box, using (e.g. Jewitt et al. 2014b)

$$C_d = \frac{2.25 \cdot 10^{22} \pi r_h^2 \Delta^2 10^{0.4(m_{\odot,R} - m_R)}}{p_R \Phi(\alpha)}, \quad (3.14)$$

where $r_h = 3.249$ AU and $\Delta = 2.295$ AU denote the heliocentric and geocentric distances on 2011 December 31 (Table 3.1), respectively, $m_{\odot,R} = -27.15$ and m_R are the apparent magnitude of the Sun and of the box, respectively, $p_R = 0.05 \pm 0.02$ is the assumed geometric R-band albedo (Hsieh et al. 2009; Hsieh et al. 2023), and $\Phi(\alpha)$ is the scattering phase function (Sect. 2.2.1) at $\alpha = 5^\circ$ (solar phase angle on 2011 December 31, Table 3.1). I determined the total dust cross section to be (0.22 ± 0.02) km².

The dust cross section profile for image 2011 December 31 is presented in Fig. 3.25 where the filling factor on the y-axis is simply the cross section divided by the area of the rectangular box. The dust cross section is influenced by the size of the particle. In general, larger particles take up more space individually, whereas smaller particles can collectively cover a larger area. This results in smaller cross section values for larger particles compared to those of smaller particles. However, this expected trend was not evident in the second segment of the tail, which may be attributed to image noise.

The total cross sectional area represents the overall space in which the dust particles are distributed. By measuring this total area and the average size of the particles, we can estimate the

total number of particles, which in turn allows us to calculate their mass in each box using (e.g. Hsieh et al. 2004)

$$M_d = (4/3)\pi\rho_d a_d^3 N_d, \quad (3.15)$$

where $\rho_d = 2500 \text{ kg m}^{-3}$ is the density of the dust particles, a_d is their size and $N_d = C_d / (\pi a_d^2)$ is the number of particles.

I utilized this method to analyze both the minimum and maximum synchrones (Sect. 3.3.2), as illustrated in Fig. 3.26. This analysis yielded the following total masses: $M_{d,min} = 1 \cdot 10^5 \text{ kg}$ and $M_{d,max} = 4 \cdot 10^5 \text{ kg}$. These total masses correspond to dust mass loss rate of $\dot{M}_{d,min} = \frac{M_{d,min}}{90 \text{ days}} = 0.01 \text{ kg s}^{-1}$ and $\dot{M}_{d,max} = \frac{M_{d,max}}{90 \text{ days}} = 0.05 \text{ kg s}^{-1}$ over a three-month period.

A power-law distribution is defined as $P(x) \propto x^{-\alpha}$, where the index α corresponds to the differential power-law distribution. For the cumulative power-law distribution, the index is $\alpha_c = \alpha - 1$. In differential power-law the data is binned, with sizes grouped into specific ranges. In contrast, a cumulative power-law does not involve binning (Newman 2005).

Fig. 3.26 shows the particle size distribution derived from the 204-day (yellow) and 295-day (purple) synchrones, plotted as the number of particles vs. particle radius in meters. The power-law behavior is evident from the linear trend in log-log space. In such a plot, the slope of the fitted line corresponds to $\alpha - 1$. My measured power-law index of $\alpha_c = 2.24 \pm 0.08$ corresponds to a differential power-law of $\alpha = 3.24 \pm 0.08$. This value, falling within the range of 3 to 4, indicates that small particles dominate in number and cross section, while larger particles contribute significantly to the mass (Levasseur-Regourd et al. 2018). For comparison, Hainaut et al. (2012) reported a power-law index of $\alpha = 3.44 \pm 0.08$ for the MBC P/2010 A2 (LINEAR), a value consistent with other studies of dust ejected from comets (Fulle 2004) in agreement with other findings in the literature (Moreno et al. 2010; Snodgrass et al. 2010; Jewitt et al. 2011; Agarwal et al. 2023).

3.3.5 Dust-to-gas ratio

Based on the dust mass loss rate, which ranges from 0.01 kg s^{-1} to 0.05 kg s^{-1} , and the gas mass loss rate, which varies between 0.02 kg s^{-1} and 0.32 kg s^{-1} , I calculated the dust-to-gas ratio. This analysis yielded a range for the dust-to-gas (f_{dg}) ratio of approximately 0.03 to 2.5. This ratio is significantly lower than the $f_{dg} = 10$ value commonly adopted for active asteroids (Fulle et al. 2016; Reach et al. 2000). Additionally, typical dust-to-gas mass ratios for comets and active asteroids, noted by Choukroun et al. (2020), range between 1 and 10, indicating that my upper limit of 2.5 is still below these reported values. Specifically, the dust-to-gas ratio for the comet 67P is $0.73_{-0.70}^{+1.30}$ (Marschall et al. 2020). My ratio is lower than most values reported in the literature, but it still aligns with the observations made for 67P, suggesting possible similarities in emission dynamics or physical characteristics. Additionally, the uncertainties in both the dust and gas mass loss rates, as well as their associated measurements, could further contribute to the observed discrepancies.

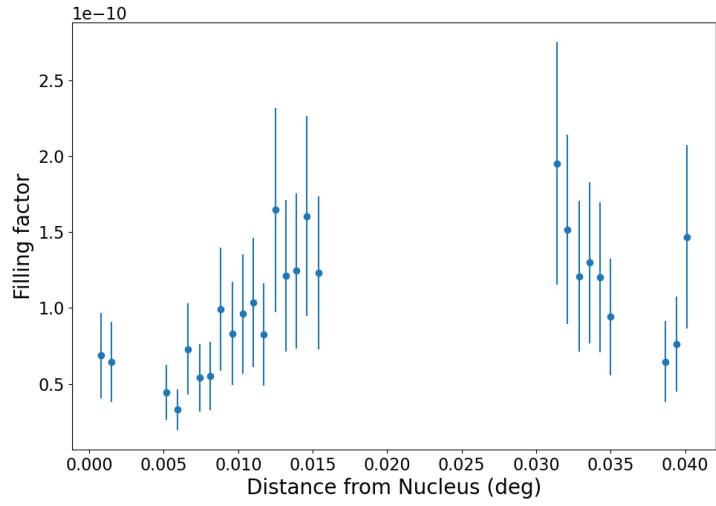


Figure 3.25: Filling factor vs. distance from the nucleus. Analysis done on the 2011 December 31 image.

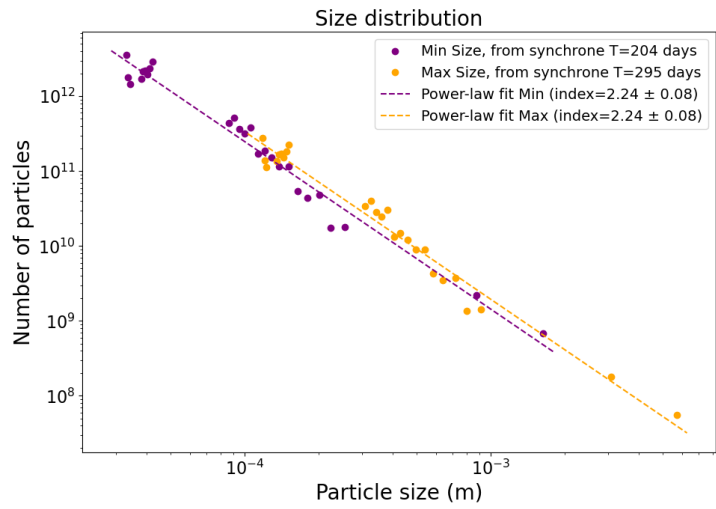


Figure 3.26: Particle size distribution, showing the number of particles in each rectangular box vs. their size in meters. The analysis is based on the 204-day (yellow) and 295-day (purple) synchrotrons. The dashed lines indicate the power-law fit.

3.3.6 Particle velocities

I calculated the FWHM of 324P on two images taken on 2011 December 22 and 31 using the SAOImageDS9 astronomical imaging and data visualization application (Smithsonian Astrophysical Observatory 2000; Joye 2006). Gaussian smoothing was applied to reduce noise and enhance the visibility of larger-scale structures in the tail of the image, facilitating more accurate FWHM measurements. This technique uses a Gaussian kernel to smooth the image by averaging pixel values with their neighboring pixels, weighted according to their distance from the central pixel. The process effectively reduces high-frequency noise while preserving the overall structure of the image. In this analysis, Gaussian smoothing was performed with a kernel radius $r = 3$ and a standard deviation $\sigma = 2$. A kernel is a square matrix used to apply the smoothing effect; in this case, the radius of 3 pixels means that the kernel covers a 7×7 pixel area centered on each pixel (since the kernel size is $2r + 1$). The value of σ defines the spread of the Gaussian function, which controls how neighbouring pixels contribute to the smoothing. Pixels closer to the center of the kernel are assigned higher weights, while those farther away contribute less to the smoothed value.

To begin, I carefully defined regions along the tail, focusing on the not contaminated areas. Once these regions were established, I generated intensity profiles. The resulting plots illustrated the tail intensity along the vertical axis and the distance along the tail on the horizontal axis. From each profile, I identified the peak intensity, which corresponded to the brightest point of the tail. To calculate the FWHM, I found half of the peak intensity value. I then examined the profile to identify the points where the intensity crossed this half-maximum level on either side of the peak. By measuring the distance between these two points, I determined the FWHM of the tail. In Fig. 3.27, I present the FWHM of the tail plotted against the distance from the nucleus for the two images. It is possible that the seeing conditions were poorer on December 22, which may account for the slightly different results observed.

Next, I calculated the ejection velocity of the particles by dividing the FWHM of the tail by the emission times $T_{emiss,1}$ and $T_{emiss,3}$ determined from the syndyne-synchrone model (Sect. 3.3.2). As mentioned earlier, each distance from the nucleus is associated with a specific particle size, meaning that each FWHM—and, consequently, each calculated velocity—corresponds to a particular particle size. This method provides an estimate of the ejection velocity in the direction perpendicular to the tail, representing how quickly the particles have spread out relative to the motion of the MBC. In Fig. 3.28, it is noted that larger particles in both cases have an ejection velocity of $v_{ejection} = 0.10 \text{ m s}^{-1}$. In contrast, smaller particles located farther from the nucleus exhibit slightly different ejection velocities: 0.30 m s^{-1} for the December 22 image and 0.20 m s^{-1} for the December 31 image. This variation can be attributed to the poorer seeing conditions on December 22. The observed ejection velocities of particles are comparable to the escape velocity of 324P of $v_{escape} = 0.61 \text{ m s}^{-1}$ (Sect. 3.2.5). This indicates that particles larger than those observed are not being ejected, as they would require lower ejection velocities to escape. Consequently, this reinforces the conclusion that the particles located nearest to the gap are, in fact, the largest ones that have been emitted.

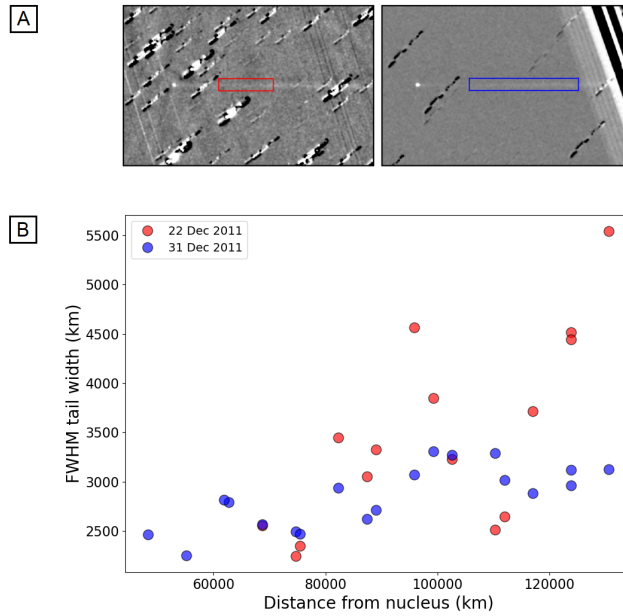


Figure 3.27: Panel A: the tail of 324P on 2011 December 22 (on the left side) and on 2011 December 31 (on the right side). The red and blue rectangles are the region where the width analysis was performed. Panel B: FWHM tail width vs. distance from the nucleus plot. Analysis done for the December 22 (red) and 31 (blue) images in panel A.

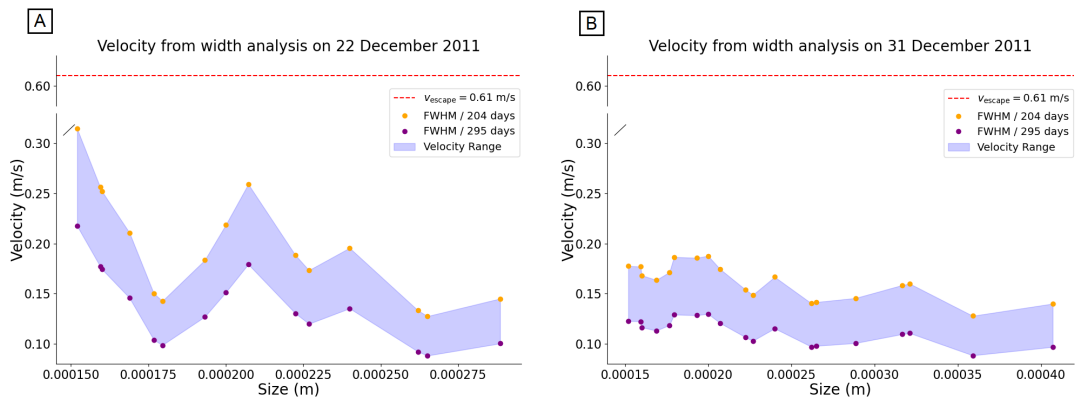


Figure 3.28: Velocity derived from tail width analysis for the December 22 (panel A) and 31 (panel B) images plotted against particle size. The analysis is based on the 204-day (yellow) and 295-day (purple) synchrones. Shaded blue region represents the range of velocities. The red dashed line indicates the escape velocity.

4 Photometry on the nucleus of 2010 LH15

The following parts are described in Mastropietro et al. (2024b).

4.1 Dataset

4.1.1 Telescopes

Visible light images of LH15 were obtained with the GMOS-N instrument on the 8-meter Gemini North Telescopes ($0.16'' \text{ pixel}^{-1}$). The pixel scale changed due to the update of the GMOS-N detectors in February-March 2017 (Gimeno et al. 2019).

4.1.2 Observations

I obtained the necessary images of LH15 to characterize its nucleus in its inactive phase (Program ID: GN-2022B-Q-125, PI: Mastropietro). LH15 was observed on 2023 July 7, 8, and 17, using the GMOS-N instrument in the R-band filter (Figs. 4.1 and 4.2).

During these days the MBC was at heliocentric distances (r_h) of 2.525 AU, 2.521 AU and 2.485 AU, geocentric distances (Δ) of 1.842 AU, 1.849 AU and 1.919 AU, phase angles (α) of 20.1° , 20.4° and 22.3° , and true anomalies (ν) of 261.8° , 262.1° and 264.3° , respectively.

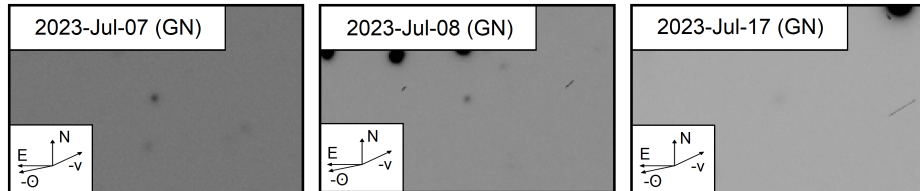


Figure 4.1: Mosaic of the visual R-band images of LH15 (at the center of each panel). Dates and directions on sky are labeled as in Fig. 3.2.

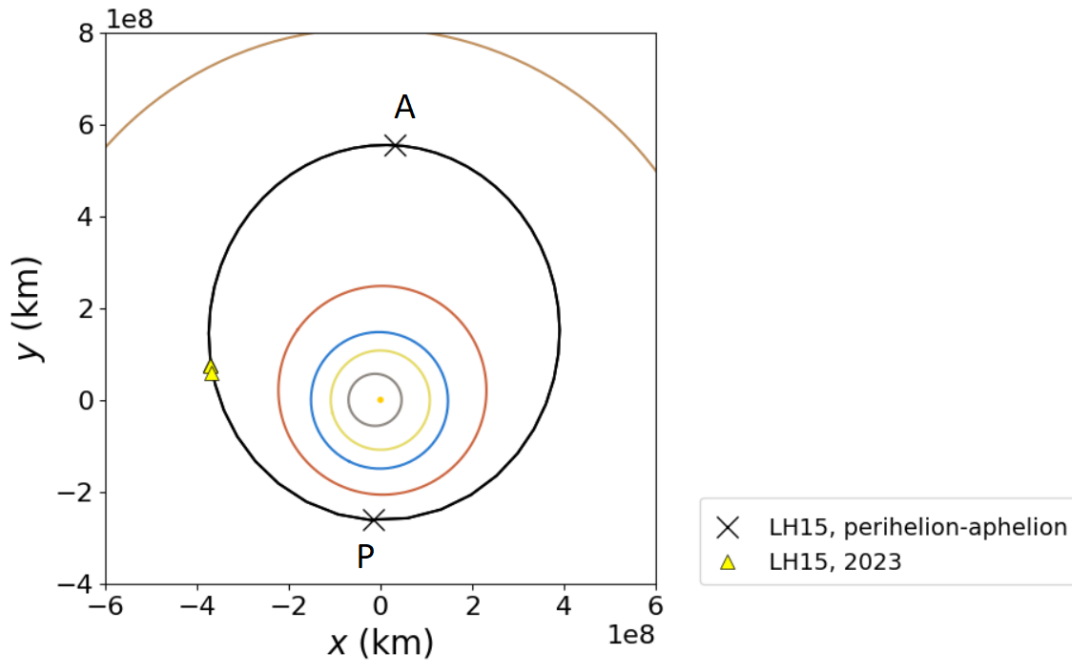


Figure 4.2: Same coordinate system as Fig 3.1. The plot shows the positions of LH15 at the epochs of my observations with the orbits of Mercury, Venus, Earth, Mars, LH15, and Jupiter. X-dots represent perihelion (P) and aphelion (A) positions. Triangular dots are visual data. Plot generated using the poliastro Python library (Juan Luis Cano Rodríguez & Jorge Martínez Garrido 2022).

4.2 Photometry

I performed bias subtraction and flat-fielding, with photometric calibration carried out by a student I co-supervised during their Praktikum, as detailed in Sect. 2.1.

Using IRAF, photometry on individual images of LH15 was carried out using a circular aperture with a radius of 7 pixels ($1.13''$), ensuring that all the flux from the target was captured, even with variable seeing conditions.

As result of the photometry, as in Sect. 2.2.1, I determined the apparent R-band magnitudes for the individual images. On the three different nights, I obtained the following average apparent R-band magnitudes of LH15: (22.8 ± 0.1) mag on 2023 July 7 (derived from 25 images); (22.6 ± 0.1) mag on 2023 July 8 (derived from 14 images); and (23.2 ± 0.1) mag on 2023 July 17 (derived from 1 image). Finally, I calculated the absolute magnitudes for the single images. In Table 4.1 are the results.

Additionally, I also performed the calculation assuming an S-type composition with $G = 0.25 \pm 0.12$, given the unknown composition of LH15. This resulted in a magnitude difference of 0.2 mag.

Table 4.1: Observations of LH15.

UT Date ^a	m_R^b	H_R^c
2023 Jul 7 06:09:50	22.8 ± 0.4	18.5 ± 0.5
2023 Jul 7 06:15:24	22.6 ± 0.9	18.3 ± 0.9
2023 Jul 7 06:20:59	22.6 ± 0.5	18.3 ± 0.5
2023 Jul 7 06:26:33	22.8 ± 0.5	18.4 ± 0.6
2023 Jul 7 06:32:07	22.7 ± 0.4	18.4 ± 0.5
2023 Jul 7 06:37:41	22.7 ± 0.4	18.4 ± 0.4
2023 Jul 7 06:43:16	22.7 ± 0.5	18.3 ± 0.5
2023 Jul 7 06:48:50	22.6 ± 0.7	18.2 ± 0.7
2023 Jul 7 06:54:24	22.9 ± 0.4	18.6 ± 0.5
2023 Jul 7 06:59:58	22.8 ± 0.4	18.5 ± 0.5
2023 Jul 7 07:05:33	22.8 ± 0.4	18.4 ± 0.5
2023 Jul 7 07:11:08	22.7 ± 0.5	18.3 ± 0.5
2023 Jul 7 07:16:42	22.7 ± 0.5	18.4 ± 0.5
2023 Jul 7 07:22:17	22.8 ± 0.4	18.5 ± 0.4
2023 Jul 7 07:27:52	22.9 ± 0.4	18.6 ± 0.4
2023 Jul 7 07:33:26	22.8 ± 0.4	18.5 ± 0.4
2023 Jul 7 07:39:00	23.0 ± 0.7	18.6 ± 0.7
2023 Jul 7 07:44:34	23.0 ± 0.6	18.7 ± 0.6
2023 Jul 7 07:50:08	22.8 ± 0.4	18.5 ± 0.4
2023 Jul 7 07:55:43	22.7 ± 0.4	18.4 ± 0.4
2023 Jul 7 08:01:18	22.6 ± 0.4	18.2 ± 0.4
2023 Jul 7 08:06:52	22.8 ± 0.5	18.4 ± 0.6
2023 Jul 7 08:12:27	23.1 ± 0.6	18.8 ± 0.6
2023 Jul 7 08:18:02	22.9 ± 0.4	18.6 ± 0.4
2023 Jul 7 08:23:36	22.8 ± 0.8	18.5 ± 0.8
2023 Jul 8 07:40:42	22.6 ± 0.5	18.3 ± 0.5
2023 Jul 8 07:46:15	22.6 ± 0.6	18.3 ± 0.6
2023 Jul 8 07:51:48	22.6 ± 0.5	18.2 ± 0.6
2023 Jul 8 07:57:21	22.5 ± 0.5	18.2 ± 0.5
2023 Jul 8 08:02:54	22.7 ± 0.6	18.3 ± 0.6
2023 Jul 8 08:08:27	22.6 ± 0.5	18.3 ± 0.6
2023 Jul 8 08:14:00	22.7 ± 0.6	18.3 ± 0.6
2023 Jul 8 08:19:33	22.7 ± 0.6	18.3 ± 0.6
2023 Jul 8 08:25:06	22.5 ± 0.7	18.2 ± 0.7
2023 Jul 8 08:41:45	22.6 ± 0.5	18.2 ± 0.5
2023 Jul 8 08:47:18	22.5 ± 0.5	18.1 ± 0.5
2023 Jul 8 08:52:51	22.6 ± 0.5	18.3 ± 0.5
2023 Jul 8 08:58:24	22.3 ± 0.9	17.9 ± 0.9
2023 Jul 8 09:03:58	22.6 ± 0.6	18.2 ± 0.6
2023 Jul 17 06:54:56	23.2 ± 0.1	18.7 ± 0.2

^aDate and hour of the exposure. ^bApparent R-band magnitude measured using an aperture angular radius of 1.13". ^cAbsolute R-band magnitude assuming IAU H-G phase function where $G = 0.15 \pm 0.12$.

4.3 Lightcurve measurements and rotational period

I calculated the weighted average and standard deviation of the absolute R-band magnitudes measured on three different nights to be (18.4 ± 0.2) mag. Fig. 4.3 presents the absolute magnitudes measured from individual images of LH15. Photometry was not possible between 08:25 and 08:41 on 2023 July 8 due to the presence of bright stars.

During these observations at $\nu = 262^\circ$, the MBC showed no signs of activity. This is also evident from the radial profile of the nucleus (Fig. 4.4), which displays a stellar appearance, implying absence of detectable dust near the nucleus. This suggests that LH15 was inactive and any variations in brightness could be linked to its rotational period.

The lightcurve profile presented an indistinct pattern, preventing the determination of an accurate rotational period. However, based on Fig. 4.3, there is no definitive evidence supporting a rotational period of less than 2 hours.

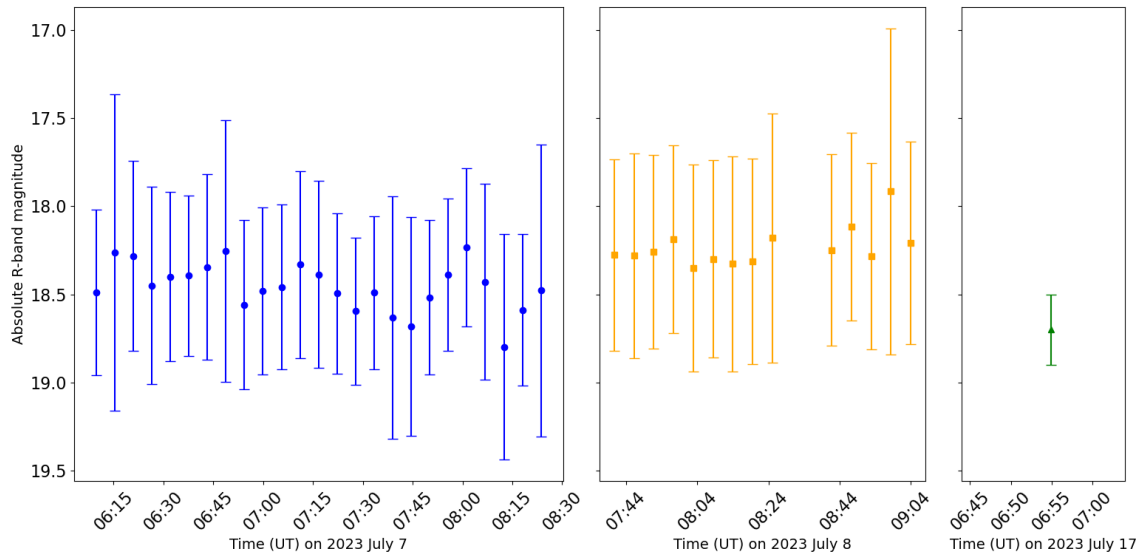


Figure 4.3: Lightcurve profiles of LH15 on 2023 July 7, 8, and 17. Credit: Mastropietro et al. (2024b), Figure 1.

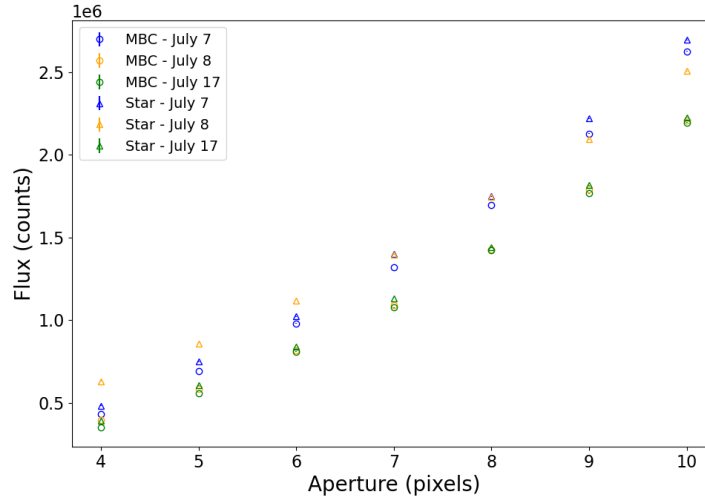


Figure 4.4: Radial profile of LH15 and a star on the three different dates and with aperture size between 4 and 10 pixels.

4.4 Nucleus radius

Using Eq. (2.6), from the averaged absolute magnitude, I determined the nucleus radius of LH15 to be $r_N = (0.5 \pm 0.1)$ km, assuming a C-type classification, a spherical shape, and a geometric R-band albedo of $p_R = 0.05 \pm 0.02$ (Hsieh et al. 2009; Hsieh et al. 2023).

In the literature, there exists a geometric albedo for LH15 of $p_V = 0.243 \pm 0.101$. It was found by a combination of infrared data from NEOWISE (Near-Earth Object Wide-field Infrared Survey Explorer) and visible light data in V-band (Masiero et al. 2011; Mainzer et al. 2019). However, I did not use this geometric albedo in the calculation of the nucleus size. This decision was based on the possibility that this albedo might predominantly reflect coma dust rather than surface characteristics, given the variability in the activity levels of the two sets of observations:

- the NEOWISE measurement was obtained at $\nu = -33.1^\circ$, falling within the range of true anomalies ($-70^\circ < \nu < 140^\circ$) where other MBCs have shown activity (Hsieh et al. 2011; Hsieh et al. 2018b; Hsieh et al. 2018; Hsieh et al. 2023);
- the scattered visible light brightness may have been obtained during a different level of activity compared to the NEOWISE data (priv. comm. with Masiero¹).

This uncertainty in activity levels introduces considerable uncertainty into the albedo estimation (Masiero et al. 2021). Therefore, considering that LH15 is an MBC, I opted to use a generic C-type albedo value instead.

¹Masiero et al. (2011) used the published magnitude values for all asteroids, available from the Minor Planet Center (MPC), as optical data. When combined with NEOWISE measurements, this data provides the albedo for all analyzed asteroids. In Mainzer et al. (2019), the NEOWISE epoch used in Masiero et al. (2011) is specified, but the epoch of the optical data is not. I searched the MPC database for this information, but could not locate it, as they do not maintain an archive for past epochs (I confirmed this via email with their helpdesk). Consequently, I reached out to Masiero via email and received this response.

5 Investigating the activity of the disrupted asteroid 62412 (2000 SY178)

5.1 Dataset

5.1.1 Telescopes

Visible light images of 62412 were obtained with the Copernico 1.82 m Reflector Telescope ($0.25'' \text{ pixel}^{-1}$) in Asiago Mount Ekar, Italy, equipped with the AFOSC + Andor iKon-L DZ936N-BEX2-DD-9HF instruments. Archival visible light images were obtained with the MegaPrime instrument on the 3.6-meter CFHT ($0.18'' \text{ pixel}^{-1}$).

5.1.2 Observations

I obtained images of 62412 with the goal of investigating whether sublimation-driven activity, similar to what was observed in 2014, had reoccurred in its 2024 pre-perihelion passage (Observations collected at Asiago Mount Ekar, PI: Mastropietro). 62412 was observed on 2023 November 7 - 8, 2024 January 3 - 4, 2024 January 30, and 2024 February 14, using the AFOSC + Andor iKon-L DZ936N-BEX2-DD-9HF instruments in the R-band filter (Figs. 5.1 and 5.2). Using the CADC website, I identified also CFHT images taken with different filters: the r.MP9601 filter on 2012 January 24–27, the i.MP9702 filter on 2013 January 4, the wide filter gri.MP9605 filter on 2018 December 9 - 13. In Table 5.1 are the heliocentric and geocentric distances, the phase angles and true anomalies of the dates of observation.

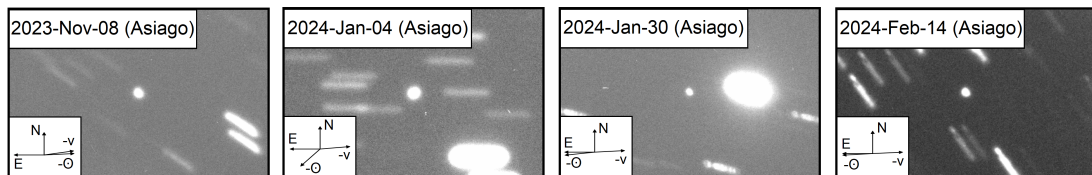


Figure 5.1: Mosaic of the composite R-band images of 62412 (at the center of each panel). Dates and directions on sky are labeled as in Fig. 3.2.

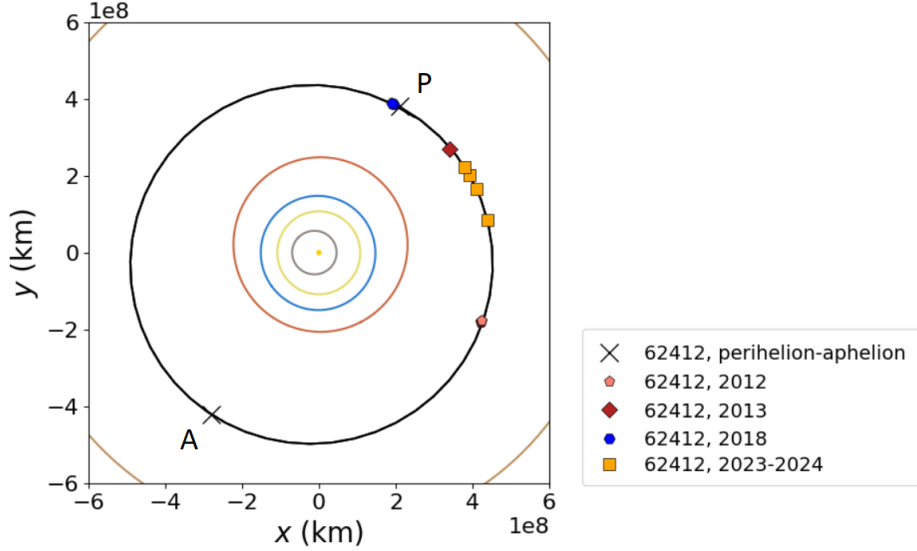


Figure 5.2: Same coordinate system as Fig 3.1. The plot shows the positions of 62412 at the epochs of my observations with the orbits of Mercury, Venus, Earth, Mars, 62412, and Jupiter. X-dots represent perihelion (P) and aphelion (A) positions. Pentagon, diamond, hexagon, and square dots are visual data. Plot generated using the poliastro Python library (Juan Luis Cano Rodríguez & Jorge Martínez Garrido 2022).

Table 5.1: Observations of the disrupted asteroid 62412.

UT Date	Telescope ^a	N ^b	r_h^b	Δ^d	α^e	ν^f	m_R^g	H_R^h
2010 Jun 2	<i>Aphelion</i>	–	3.427	3.062	16.8	180.0	–	–
2012 Jan 24	CFHT	2	3.103	3.010	18.4	277.1	19.5 ± 0.2	13.7 ± 0.2
2012 Jan 25	CFHT	1	3.102	3.024	18.4	277.3	19.86 ± 0.02	14.0 ± 0.1
2012 Jan 26	CFHT	1	3.102	3.037	18.4	277.4	18.95 ± 0.01	13.1 ± 0.1
2012 Jan 27	CFHT	1	3.101	3.051	18.4	277.6	19.82 ± 0.02	14.0 ± 0.1
2013 Jan 04	CFHT	4	2.900	1.952	6.3	344.3	18.2 ± 0.1	13.9 ± 0.1
2013 Mar 21	<i>Perihelion</i>	–	2.892	2.357	18.5	0.0	–	–
2018 Oct 30	<i>Perihelion</i>	–	2.896	3.161	18.2	0.0	–	–
2018 Dec 09	CFHT	2	2.898	2.623	19.8	8.4	19.5 ± 0.1	14.1 ± 0.2
2018 Dec 13	CFHT	1	2.899	2.568	19.6	9.2	19.10 ± 0.01	13.8 ± 0.2
2021 Aug 27	<i>Aphelion</i>	–	3.408	2.481	7.9	180.0	–	–
2023 Nov 8	Copernico	46	2.990	2.368	16.7	309.9	18.9 ± 0.2	13.8 ± 0.2
2024 Jan 4	Copernico	16	2.961	1.983	2.4	321.0	17.9 ± 0.2	13.8 ± 0.2
2024 Jan 30	Copernico	17	2.950	2.098	11.4	326.2	18.3 ± 0.1	13.6 ± 0.1
2024 Feb 14	Copernico	40	2.944	2.236	15.4	329.2	18.7 ± 0.2	13.8 ± 0.2
2024 Jul 15	<i>Perihelion</i>	–	2.914	3.855	6.6	0.0	–	–

^aTelescope. ^bNumber of images taken. ^cHeliocentric distance in AU. ^dGeocentric distance in AU. ^eSolar phase angle (Sun-Target-Observer) in degrees. ^fTrue anomaly in degrees. ^gApparent R-band magnitude measured using a circular aperture with a radius of 15 pixels. ^hAbsolute R-band magnitude assuming IAU H-G phase function where $G = 0.15 \pm 0.12$.

5.2 Photometry

I performed bias subtraction, flat-fielding, and photometric calibration, as detailed in Sect. 2.1.

Using IRAF, photometry on individual images of 62412 was carried out using a circular aperture with a radius of 15 pixels ($3.8''$), ensuring that all the flux from the target was captured.

As result of the photometry, as in Sect. 2.2.1, I determined the apparent R-band magnitudes for the individual images and the corresponding absolute R-band magnitudes to plot the lightcurve graphics (Fig. 5.3). In Table 5.1 are the average apparent and absolute R-band magnitudes for each night.

5.3 Lightcurve measurements and rotational period

Fig. 5.3 presents the absolute magnitudes measured from individual images of 62412. Photometry was not possible in some hours due to the presence of bright stars. The lightcurve profiles presented a clear pattern. From Fig. 5.4, I found a rotational period between 3.32 hours and 3.41 hours, consistent or slightly larger than the period reported by Sheppard & Trujillo (2015) of 3.33 hours.

5.4 Nucleus radius size

I calculated the average absolute R-band magnitude of 62412 across the four nights of observation to be (13.7 ± 0.1) mag. Using this magnitude in Eq. (2.6), I obtained a nucleus radius of $r_N = (4.0 \pm 0.4)$ km, assuming a C-type classification, a spherical shape, and a geometric R-band albedo of $p_R = 0.065 \pm 0.010$ (Masiero et al. 2011). This value is consistent with the value in the literature of (3.9 ± 0.3) km, found by Sheppard & Trujillo (2015), who also used an albedo of $p_R = 0.065 \pm 0.010$ and an absolute R-band magnitude of (13.82 ± 0.23) mag measured on 2014 May 2. Other values from the literature are (5.2 ± 0.3) km from Masiero et al. (2011), who used the same albedo of $p_R = 0.065 \pm 0.010$ and an absolute R-band magnitude of (13.15 ± 0.20) mag measured in 2010¹, and a slightly larger radius of (5.4 ± 0.6) km by Ferrín et al. (2019), who used a lower albedo of $p_R = 0.042$ and an absolute R-band magnitude of (13.55 ± 0.05) mag measured in 2017-2019. If the same albedo of $p_R = 0.065 \pm 0.010$ had been applied in their calculations, the radius would have been (4.2 ± 0.3) km, aligning with the findings of Sheppard & Trujillo (2015) and my results. This supports the hypothesis that the 2013 event may have caused changes in the size of the asteroid.

5.5 Comparison with the literature

The composite R-band images in Fig. 3.2 show no signs of a tail, indicating that the asteroid was inactive during its 2024 pre-perihelion passage. This contrasts with the dust emission and tail observed in 2014 following its perihelion, as noted by Sheppard & Trujillo (2015). If 62412 were an MBC, sublimation-driven activity would be seen near perihelion. If confirmed, the

¹A mean V-band absolute magnitude of 13.5 was derived from observations conducted between 2010 July and August by the J75 – OAM Observatory, La Sagra. These observations are archived in the IAU Minor Planet Center (MPC): https://www.minorplanetcenter.net/db_search.

absence of reactivation during later perihelion passages could be due to a lack of exposed ice or low surface temperatures resulting from its high perihelion distance of 2.9 AU.

In Fig. 5.5, I present a comparison with the literature. In 2014, Sheppard & Trujillo (2015) measured an absolute magnitude in the R-band of (13.82 ± 0.23) mag, 0.7 mag fainter than the (13.15 ± 0.2) mag reported by Masiero et al. (2011) in 2010. This measurement was taken close to aphelion and therefore I considered it to represent the brightness of the inactive nucleus in Fig. 5.5. In 2010 and 2012, 62412 displayed a lightcurve amplitude of 1 mag and a higher brightness. After the 2013 event, the brightness decreased, and the lightcurve amplitude reduced to 0.45 mag, indicating a possible change in shape (Sheppard & Trujillo 2015). A higher amplitude typically corresponds to a more elongated shape, which is generally more susceptible to disruption from rapid rotation than a more spherical object. By 2023–2024, however, the observed amplitude was larger, of order 0.7 mag, which could be explained by geometric viewing effects.

The magnitude of 62412 remained consistent between different epochs in 2014, 2017, 2019 and 2023–2024. This implies that any dust emission—potentially responsible for the asteroid appearing dimmer in 2014 compared to earlier epochs before the 2013 event—was either not ongoing or not significant enough to affect its brightness during subsequent perihelion passages. This would suggest that the dust emission seen in 2014 could have been an isolated event, potentially triggered by rotational destabilization, consistent with the classification of 62412 as a fast rotator.

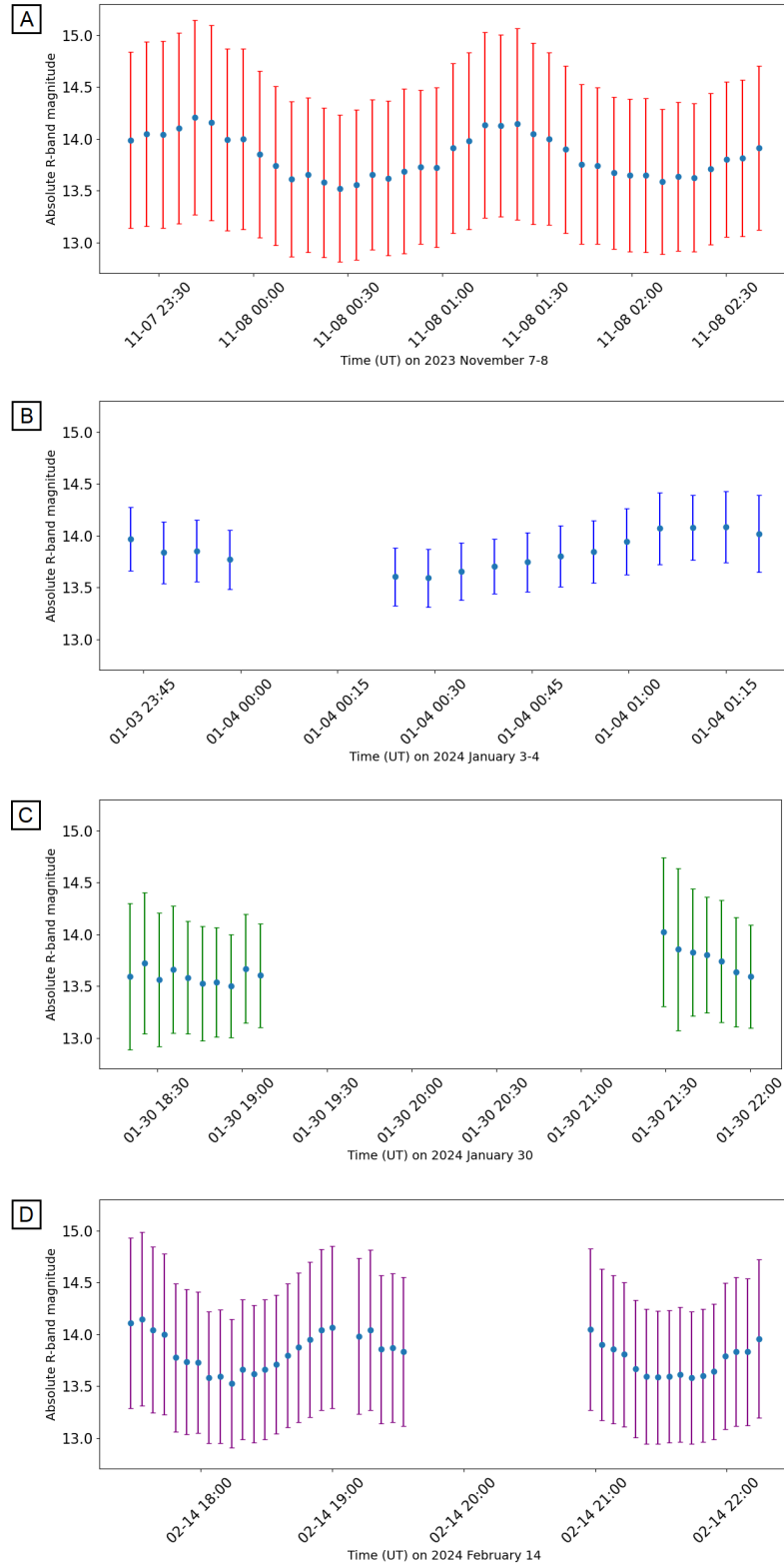


Figure 5.3: Lightcurve profiles of 62412.

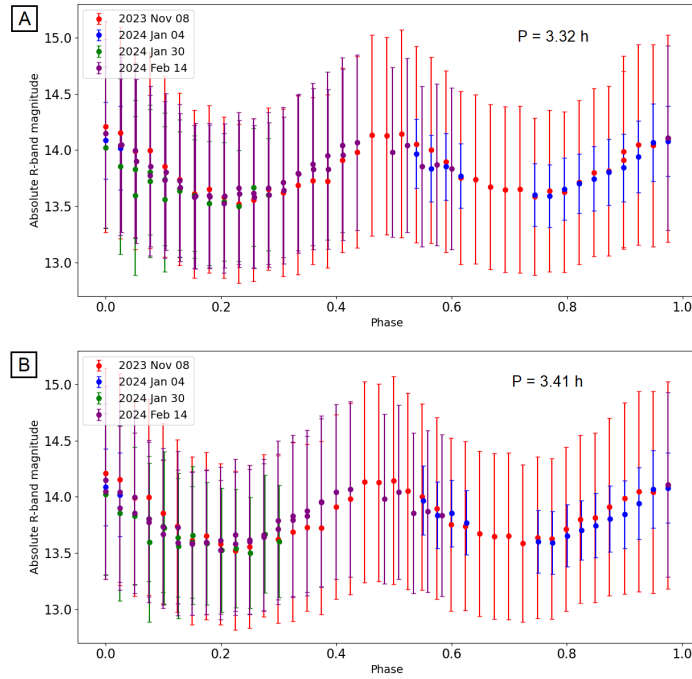


Figure 5.4: The phased period for 62412 of 3.32 hours (panel A) and 3.41 hours (panel B).

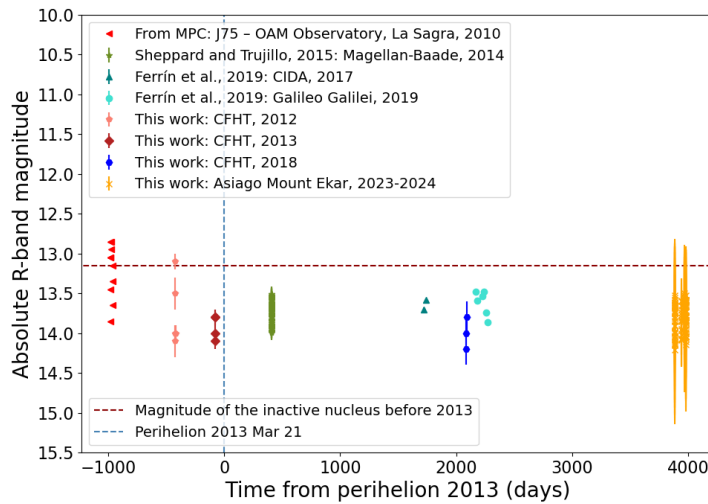


Figure 5.5: Measure absolute R-band magnitudes of 62412 plotted as a function of the time from the 2013 perihelion, augmented by values from the literature (2010: Masiero et al. (2011), 2014: Sheppard & Trujillo (2015), 2017-2019: (Ferrín et al. 2019)), see legend. The vertical dashed line indicates the 2013 perihelion. The horizontal dashed line corresponds to the absolute magnitude of the inactive nucleus (13.15 mag) before 2013.

6 Summary, discussions and outlook

This chapter synthesizes the findings from the analysis of the MBCs 324P and LH15, along with the disrupted asteroid 62412, offering a comparative perspective on their nucleus properties and activity characteristics. While 324P and LH15 show sublimation-driven activity, a typical behavior of MBCs, 62412 stands apart as a disrupted asteroid, where its transient activity is attributed to non-sublimation mechanisms, such as rotational destabilization. This distinction provides an opportunity to contrast the drivers of activity in these objects.

6.1 324P/La Sagra: Temporal activity and dust emission

The nucleus radius of $r_N = (0.52 \pm 0.16)$ km I derived for 324P in its inactive period (from optical data obtained in 2013) is consistent with values reported in the literature (Hsieh et al. 2023), and this agreement reinforces the analysis of the long-term activity of this MBC. The activity of 324P across three observed perihelion passages (2010, 2015, and 2021) provided valuable data on the long-term evolution of its cometary outgassing and dust emission. The decline in activity over time, as indicated by aperture photometry, suggests progressive surface mantling and/or volatile depletion. The diminishing outgassing supports the hypothesis that near-surface ices are being depleted, leading to reduced cometary activity with each perihelion passage. This trend is consistent with other MBCs, which exhibit similar decreases in activity as they undergo repeated solar heating cycles (Hsieh et al. 2018a).

The $Af\rho$ profile analysis revealed a key transition in the dust coma from a lower-activity phase before perihelion to a higher-activity state after perihelion, suggesting that thermal waves penetrate the surface and trigger sublimation of deeper ice layers after the closest solar approach. This delayed response in activity is a key finding, consistent with observations of other MBCs such as 238P (Hsieh et al. 2011), 358P/PANSTARRS (Hsieh et al. 2018), 259P/Garradd (Hsieh et al. 2021), 313P/Gibbs (Hsieh et al. 2015). These results reveal the intricate nature of heat transfer processes within them (Hsieh 2015) and demonstrate the importance of the importance of continuous monitoring of MBCs throughout their orbit to better understand these dynamic processes.

From the analysis of the SEDs of 324P, the dust color temperature was derived by fitting thermal emission data from WISE and Spitzer observations. This approach allowed the separation of the thermal and scattered light components of the dust, providing insights into its properties, such as temperature, cross section, emissivity, and geometric albedo. Geometric albedo was estimated to range from 2% to 45%, which spans typical values for both C-type and S-type asteroids. This broad range indicates that the available data are insufficient to tightly constrain the spectral type of the dust surrounding 324P. Notably, the Spitzer 4.5 μm data reveal evidence of dust superheating, likely caused by small or porous particles that cannot efficiently radiate thermally at shorter wavelengths. A comparison with the results from Bauer et al. (2012), who used the same WISE images to derive the albedo of 324P, highlights some key differences in the analysis and findings. Bauer et al. (2012) determined an effective temperature of $T_{eff} = 204$ K and calculated a geometric albedo $p_V = 0.01 \pm 0.01$. Their higher temperature estimate is notably different from the color temperature I derived from the WISE bands. This discrepancy likely arises from differences in the method used to estimate the effective temperature. While

Bauer et al. (2012) adopted a single temperature to fit the thermal emission, I treated the dust color temperature as a free parameter and directly fitted it to the observed flux ratios, resulting in a lower temperature. The lower temperature I derived suggests the presence of larger or more compact dust particles, which radiate more efficiently than the smaller, hotter particles inferred by Bauer et al. (2012). It is also important to note that Bauer et al. (2012) remarked that "the temperature may be cooler than expected, and it may be cool enough to be explained by the presence of isothermal dust grains". This aligns with my findings, as the lower temperature derived in my analysis supports the presence of larger or isothermal dust grains, which radiate efficiently and do not become significantly superheated. Regarding the geometric albedo, their low value is consistent with the lower limit of my albedo estimates. A higher effective temperature typically leads to a smaller inferred grain cross section—and, through modeling, to a higher geometric albedo. However, Bauer et al. (2012) derived a very low albedo, likely due to differences in their assumptions about the thermal emission model and dust properties.

In addition to the temporal evolution of its activity, the syndyne-synchrone modeling provided insights into the particle size distribution and dynamics of dust particles ejected from 324P. The image of 324P, captured on 2011 December 31, provided clear evidence of a gap between the nucleus and the tail. The length of this gap serves as a critical diagnostic indicator of the largest particle size present in the tail. This methodology mirrors that employed in previous studies, such as those conducted on comet 249P/LINEAR (Fernández et al. 2017). The particle size distribution helps to reveal how many small versus large particles are being ejected. The analysis showed that small particles dominate in number and have a higher scattering cross section, meaning they contribute more to the brightness of the tail. However, despite their larger contribution to brightness, small particles do not carry much mass. Larger particles, though fewer in number, play a significant role in the total mass loss of the comet. These particles are less affected by solar radiation pressure, so they tend to stay closer to the nucleus for longer periods of time and contribute more mass per particle. The large particle size estimates for 324P range from 0.2 mm to 0.8 mm and the corresponded gas production rates further align with those observed in other MBCs, such as 238P, offering a consistent picture of the sublimation-driven processes at play in these objects. As a comparison an analysis done by Jewitt et al. (2016) when 324P was active in 2015 September, October and December shows that the small particle sizes are between 50 μm and 200 μm , with no evidence of large particle. My syndyne-synchrone analysis reveals that large particles (ranging from 0.2 mm to 0.8 mm) are ejected post-perihelion. We observe that the large particles ejected near perihelion have already dissipated by the time of the image capture. We can compare this to comets. In comets, 1 mm-sized particles are typically ejected due to the sublimation of water ice, especially near perihelion, where solar heating generates enough gas pressure to mobilize smaller aggregates. This is similar to what we observe in MBCs. However, in comets, centimeter-sized particles require higher gas pressures, which are more readily generated by the sublimation of super-volatiles like CO_2 or CO . This process is more effective post-perihelion, when the comet is farther from the Sun, and super-volatile sublimation becomes more significant (Gundlach et al. 2015, 2020). In MBCs, however, CO_2 and CO are not relevant (Kelley et al. 2023). These objects contain water ice, which is more stable in the warmer regions of the asteroid belt, but they are unlikely to have significant amounts of CO_2 and CO , which had already sublimated due to the warmer conditions in this region. Even though I measured the sizes of large particles, challenges remain in constraining the dust-to-gas ratio for 324P, as the measurements were impacted by observational uncertainties.

6.2 2010 LH15: Comparative analysis

The analysis of the inactive nucleus of LH15 in 2023 yielded an absolute magnitude of $H_R = (18.4 \pm 0.2)$ mag and an estimated radius of $r_N = (0.5 \pm 0.1)$ km, consistent with a C-type object and comparable in size to the nucleus of 324P and other MBCs (Hsieh et al. 2023). This result suggests that LH15 may be a typical MBC, with a volatile-rich composition similar to other objects in this class.

LH15 is located in the middle main belt. In contrast, 324P resides in the outer portion of the main belt. This difference in location raises implications regarding the physical and compositional characteristics of these MBCs. The location of LH15 suggests it may be influenced by different dynamical and thermal conditions compared to 324P in the outer belt. For instance, the temperature profiles and collisional environments are expected to vary between these regions, potentially affecting the distribution of volatiles in the nuclei of these comets. The proximity to the warmer inner regions of the asteroid belt could also lead to more pronounced sublimation processes, influencing the activity cycles of MBCs like LH15. Moreover, the differences in orbital dynamics may impact the rotational properties and evolution of MBCs. The unresolved rotational periods for both 324P and LH15 are particularly significant, as the dynamics of rotation are critical in governing dust ejection mechanisms.

Overall, understanding the positioning and its characteristics of different MBCs not only enriches our understanding of the diversity within this class of objects but also emphasizes the intricate relationships between location, composition, and activity in the main asteroid belt. Further investigation into the rotational dynamics and the activity cycle of MBCs across different regions of the main belt may yield essential clues about the formation and evolution of these celestial bodies.

6.3 62412: A non-sublimation-driven active asteroid

From the measured average absolute R-band magnitude of 62412, (13.7 ± 0.1) mag, I estimated the nucleus radius to be $r_N = (4.0 \pm 0.4)$ km. This size makes 62412 significantly larger than 324P, LH15, and most other MBCs. Its elongated shape and its rotation period, measured near the critical threshold for structural failure (the rubble-pile spin barrier of approximately 2.2 hours; Warner et al. 2009), suggest that it is at high risk for rotational disruption. Such rapid spinning could cause surface material to shift or be ejected, potentially exposing sub-surface layers of ice. This process could, in principle, trigger sublimation-driven activity. However, my observations near perihelion in 2024 revealed no evidence of a dust tail or coma, ruling out sublimation-driven activity. Additionally, my analysis revealed significant changes in the shape and size of the asteroid from before the 2013 event to afterward, as indicated by variations in its lightcurve amplitude and derived size estimates over the years. These changes provide strong evidence that the activity observed in 2014 was not sustained but rather a transient phenomenon likely caused by fast rotation. The 2013 event likely led to the ejection of surface material, forming the dust tail, and a subsequent reshaping of the asteroid. The lack of its reactivation near perihelion, both in 2018 and 2024, shows that the 2013 event was driven by non-sublimation mechanisms such as rotational destabilization. This finding is supported by evidence of changes in its shape and size, as well as a stable absolute magnitude post-2013, indicating no significant activity in the subsequent years, classifying 62412 as a disrupted asteroid, distinct from MBCs. If confirmed, this would mark the first time a change in shape and size has been directly observed

in such an object. An additional indicator that the activity of 62412 was not sublimation-driven is the observed decrease in brightness following the dust emission event, in contrast to MBCs, where sublimation typically increases brightness due to the exposure of sub-surface ice.

6.4 Limitations and future work

This thesis enhances our understanding of MBCs by revealing insights into their volatile content, activity cycles, and dust emission characteristics. It also highlights the key distinctions between MBCs and disrupted asteroids, offering valuable insights into the diverse mechanisms underlying their behavior and activity. The results provide valuable data for the growing field of small body research, especially regarding comet-like activity within the asteroid belt. The study also emphasizes the importance of long-term monitoring of MBCs, as changes in activity over time may reveal important information about their evolution.

Continued long-term monitoring of 324P, especially during its inactive phases, is essential for a more thorough analysis of dust trail evolution and particle size distribution. This would help refine current estimates of particle ejection velocities and mass loss rates, and clarify the dynamics of large particle behavior. While this study provided important insights into particle size distribution and gas production rates, uncertainties in the dust-to-gas ratio limited the precision of these findings. Future research should aim to improve measurements of this ratio to better constrain the mass loss processes in 324P and other MBCs. Future studies should also aim to address the rotational characteristics of 324P, which remains an important unresolved question. Understanding its rotation would provide valuable information about its structural integrity and activity patterns, and should be a focus of future observational campaigns. The complex albedo variations observed in the dust of 324P suggest that spectroscopic investigations are needed to better classify its spectral type and dust compositions. Such investigations will provide insights into the material being ejected. While the presence of dust superheating at $4.5\ \mu\text{m}$ complicates the classification of dust composition of 324P, it also highlights the limitations of using simple blackbody models to fit thermal emission from comets. The elevated flux at this wavelength suggests the need for more complex models that account for particle size distribution, porosity, and the presence of volatiles.

The study of LH15 also opens up additional avenues for future research, particularly considering its position in the middle main belt in contrast to 324P, which resides in the outer main belt. This distinction has significant implications for their activity, volatile content, and evolutionary history. Observing and comparing MBCs from different regions of the asteroid belt provides a broader perspective on the distribution of volatiles and the factors influencing cometary activity in different environments. The position of LH15 in the middle belt, where solar heating is generally weaker than in the inner belt but stronger than in the outer belt, may influence the onset and intensity of its activity differently compared to 324P. Studying this comet in more detail, particularly its rotational dynamics and activity cycles, could reveal unique insights into how environmental conditions in different regions of the belt affect dust emission and sublimation processes. The uncertain rotational period of LH15 is a key question that remains unresolved. Further monitoring of its activity and rotational behavior could offer new insights into the processes driving its dust emission and nucleus structure. A comparative study of both 324P and LH15 could reveal interesting contrasts and commonalities between these MBCs, enhancing our understanding of their formation and evolution.

The investigation of 62412 faces also some challenges that limit the ability to fully character-

ize its properties and activity. The lack of consistent long-term monitoring data makes it difficult to track the complete activity history of the asteroid, including any minor events that may have occurred before or after the 2013 event. Another limitation is the absence of spectroscopic studies, which restricts the ability to determine whether water ice or other volatiles are present on or beneath its surface. This gap in knowledge limits the capacity to assess the sublimation potential of the asteroid.

Expanding the study to include a larger sample of MBCs would enable robust comparisons of activity patterns, particle sizes, and volatile content across multiple objects. This would contribute significantly to our understanding of the diversity of MBCs and their role in the evolution of small bodies in the Solar System. A particularly intriguing aspect of 324P is its unique behavior, characterized by a faint dust tail of large particles that remains near its orbit even during inactive periods. This distinct feature makes 324P a fascinating case study for exploring dust emission mechanisms in MBCs. To our knowledge, no other MBC exhibits this behavior, although this could be due to limited data, particularly during inactive periods, or inadequate signal-to-noise ratios in current observations. Conducting a detailed study of this phenomenon would enhance our understanding of the variability in dust behavior across MBCs and could reveal previously unrecognized processes driving dust emission in these bodies. Ultimately, by addressing these areas in future research, we can better understand the role of MBCs in the evolution of the Solar System and uncover the underlying mechanisms governing their activity and dust dynamics.

Bibliography

- Agarwal, J., Kim, Y., Kelley, M. S. P., & Marschall, R. 2023, arXiv e-prints, arXiv:2309.12759
- Agarwal, J., Mueller, M., & Gruen, E. 2010, arXiv e-prints, arXiv:1001.3010
- A'Hearn, M. F., Feaga, L. M., Keller, H. U., et al. 2012, *ApJ*, 758, 29
- A'Hearn, M. F., Millis, R. C., Schleicher, D. G., Osip, D. J., & Birch, P. V. 1995, *Icarus*, 118, 223
- A'Hearn, M. F., Schleicher, D. G., Millis, R. L., Feldman, P. D., & Thompson, D. T. 1984, *AJ*, 89, 579
- Alexander, C. M. O. 2011, in *IAU Symposium*, Vol. 280, *The Molecular Universe*, ed. J. Cericharo & R. Bachiller, 288–301
- Alexander, C. M. O., Bowden, R., Fogel, M. L., et al. 2012, *Science*, 337, 721
- Baggett, S., McMaster, M., Biretta, J., et al. 2002, *B. Mobasher*, Baltimore, STScI
- Barucci, M., Capria, M., Coradini, A., & Fulchignoni, M. 1987, *Icarus*, 72, 304
- Barucci, M. A., Alvarez-Candal, A., Belskaya, I., et al. 2010, *The Messenger*, 141, 15
- Bauer, J. M., Mainzer, A. K., Grav, T., et al. 2012, *ApJ*, 747, 49
- Bell, J. F. 1986, in *Lunar and Planetary Science Conference*, *Lunar and Planetary Science Conference*, 985–986
- Bell, J. F. 1988, *Meteoritics*, 23, 256
- Bell, J. F. 1989, *Icarus*, 78, 426
- Binzel, R. P., Barucci, M. A., & Fulchignoni, M. 1991, *Scientific American*, 265, 88
- Binzel, R. P., Gaffey, M. J., Thomas, P. C., et al. 1997, *Icarus*, 128, 95
- Binzel, R. P. & Xu, S. 1993, *Science*, 260, 186
- Binzel, R. P., Xu, S., Bus, S. J., et al. 1993, *Meteoritics*, 28, 324
- Biver, N. & Bockelée-Morvan, D. 2015, *Proceedings of the International Astronomical Union*, 11, 228–232
- Bockelée-Morvan, D. & Biver, N. 2017, *Philosophical Transactions of the Royal Society of London Series A*, 375, 20160252
- Bockelée-Morvan, D., Crovisier, J., Mumma, M. J., & Weaver, H. A. 2004, in *Comets II*, ed. M. C. Festou, H. U. Keller, & H. A. Weaver, 391
- Bodewits, D., Kelley, M. S., Li, J.-Y., et al. 2011, *ApJL*, 733, L3

- Boss, A. P. 1994, *Icarus*, 107, 422
- Bottke, William F., J., Vokrouhlický, D., Rubincam, D. P., & Nesvorný, D. 2006, *Annual Review of Earth and Planetary Sciences*, 34, 157
- Bottke, W. F., Durda, D. D., Nesvorný, D., et al. 2005, *Icarus*, 175, 111
- Bottke, W. F., Morbidelli, A., Jedicke, R., et al. 2002, *Icarus*, 156, 399
- Bowell, E., Hapke, B., Domingue, D., et al. 1989, in *Unknown host publication*, ed. R. P. Binzel, T. Gehrels, & M. S. Matthews, 524–556
- Brasser, R. & Morbidelli, A. 2013, *Icarus*, 225, 40
- Brearley, A. J. 1989, *Geochim. Cosmochim. Acta*, 53, 2395
- Bunch, T. E. & Chang, S. 1980, *Geochim. Cosmochim. Acta*, 44, 1543
- Burbine, T. H. 2016, *Asteroids: Astronomical and Geological Bodies*, Cambridge Planetary Science (Cambridge University Press)
- Burbine, T. H., McCoy, T. J., Meibom, A., Gladman, B., & Keil, K. 2002, in *Asteroids III*, ed. J. Bottke, W. F., A. Cellino, P. Paolicchi, & R. P. Binzel, 653–667
- Burns, J. A., Lamy, P. L., & Soter, S. 1979, *Icarus*, 40, 1
- Bus, S. J. & Binzel, R. P. 2002, *Icarus*, 158, 146
- Buseck, P. R. & Hua, X. 1993, *Annual Review of Earth and Planetary Sciences*, 21, 255
- Capria, M. T., Marchi, S., De Sanctis, M. C., Coradini, A., & Ammannito, E. 2012, *A&A*, 537, A71
- Carusi, A., Kresak, L., Perozzi, E., & Valsecchi, G. B. 1987, *A&A*, 187, 899
- Carusi, A., Kresák, Ľ., & Valsecchi, G. B. 1995, *Earth Moon and Planets*, 68, 71
- Chan, Q. H. S. & Zolensky, M. E. 2022, in *New Frontiers in Astrobiology*, ed. R. Thombre & P. Vaishampayan (Elsevier), 67–110
- Chandler, C. O., Oldroyd, W. J., Hsieh, H. H., et al. 2023, *Research Notes of the American Astronomical Society*, 7, 60
- Choukroun, M., Altwegg, K., Kührt, E., et al. 2020, *Space Sci. Rev.*, 216, 44
- Cloutis, E. A., Izawa, M. R., & Beck, P. 2018, in *Primitive Meteorites and Asteroids*, ed. N. Abreu (Elsevier), 273–343
- Combi, M. R., Capria, M. T., Cremonese, G., et al. 2002, in *Astronomical Society of the Pacific Conference Series*, Vol. 272, *The Future of Solar System Exploration (2003-2013) – First Decadal Study contributions*, ed. M. V. Sykes, 323–336
- Connelly, J. N., Bizzarro, M., Krot, A. N., et al. 2012, *Science*, 338, 651

- Cordiner, M. A., Coulson, I. M., Garcia-Berrios, E., et al. 2022, *ApJ*, 929, 38
- Council, N. R. 1998, *Evaluating the Biological Potential in Samples Returned from Planetary Satellites and Small Solar System Bodies: Framework for Decision Making* (Washington, DC: The National Academies Press)
- Cruikshank, D. P., Barucci, M. A., Emery, J. P., et al. 2007, in *Protostars and Planets V*, ed. B. Reipurth, D. Jewitt, & K. Keil, 879
- Cutri, R. M., Wright, E. L., Conrow, T., et al. 2012, *Explanatory Supplement to the WISE All-Sky Data Release Products, Explanatory Supplement to the WISE All-Sky Data Release Products*
- Dalarsson, N., Dalarsson, M., & Golubović, L. 2011, in *Introductory Statistical Thermodynamics*, ed. N. Dalarsson, M. Dalarsson, & L. Golubović (Boston: Academic Press), 139–185
- Davidsson, B., Brisset, J., Daly, R. T., et al. 2021, *Bulletin of the AAS*, 53, <https://baas.aas.org/pub/2021n4i058>
- de Val-Borro, M., Rezac, L., Hartogh, P., et al. 2012, *A&A*, 546, L4
- Dello Russo, N., Kawakita, H., Vervack, R. J., & Weaver, H. A. 2016, *Icarus*, 278, 301
- Delsemme, A. 1998, *Our Cosmic Origins: From the Big Bang to the Emergence of Life and Intelligence* (Cambridge University Press)
- Divine, N. 1981, in *ESA Special Publication, Vol. 174, The Comet Halley. Dust and Gas Environment*, ed. B. Battrock & E. Swallow, 47–53
- Drahus, M., Jewitt, D., Guilbert-Lepoutre, A., et al. 2011, *ApJ*, 734, L4
- Drahus, M., Waniak, W., Tendulkar, S., et al. 2015, *ApJL*, 802, L8
- Duncan, M., Levison, H., & Dones, L. 2004, in *Comets II*, ed. M. C. Festou, H. U. Keller, & H. A. Weaver, 193
- Duncan, M. J. & Levison, H. F. 1997, *Science*, 276, 1670
- Everhart, E. 1972, *Astrophys. Lett.*, 10, 131
- Fanale, F. P. & Salvail, J. R. 1989, *Icarus*, 82, 97
- Farinella, P., Vokrouhlický, D., & Hartmann, W. K. 1998, *Icarus*, 132, 378
- Fazio, G. G., Hora, J. L., Allen, L. E., et al. 2004, *ApJS*, 154, 10
- Ferrellec, L., Snodgrass, C., Fitzsimmons, A., et al. 2023, *MNRAS*, 518, 2373
- Fernandez, J. A. 1980, *MNRAS*, 192, 481
- Fernández, J. A., Licandro, J., Moreno, F., et al. 2017, *Icarus*, 295, 34
- Ferrín, I., Fornari, C., & Acosta, A. 2019, *arXiv e-prints*, arXiv:1907.01096

- Filacchione, G., de Sanctis, M. C., Capaccioni, F., et al. 2016, *Nature*, 529, 368
- Filacchione, G., Raponi, A., Cappacioni, F., et al. 2016, *Science*, 354, 1563
- Fink, U. & Rubin, M. 2012, *Icarus*, 221, 721
- Finkbeiner, D. P., Schlafly, E. F., Schlegel, D. J., et al. 2016, *ApJ*, 822, 66
- Finson, M. L. & Probst, R. F. 1968, *ApJ*, 154, 327
- Flowers, P., Theopold, K., Langley, R., & R., R. W. 2019, *Chemistry*, 2nd edn. (OpenStax, Rice University)
- Freudling, W., Romaniello, M., Bramich, D. M., et al. 2013, *A&A*, 559, A96
- Fulle, M. 2004, in *Comets II*, ed. M. C. Festou, H. U. Keller, & H. A. Weaver, 565
- Fulle, M., Marzari, F., Della Corte, V., et al. 2016, *ApJ*, 821, 19
- Garradd, G. J., McNaught, R. H., Meyer, M., Herald, D., & Marsden, B. G. 2008, *Minor Planet Electronic Circulars*, 2008-S46
- Gehrz, R. & Ney, E. 1992, *Icarus*, 100, 162
- Gimeno, G., Firpo, V., & Kim, H. 2019, *Boletín de la Asociación Argentina de Astronomía La Plata Argentina*, 61, 252
- Gundlach, B., Blum, J., Keller, H. U., & V., S. Y. 2015, *Astronomy Astrophysics*, 583, A12
- Gundlach, B., Fulle, M., & Blum, J. 2020, *Monthly Notices of the Royal Astronomical Society*, 493, 3690
- Gwyn, S. D. J. 2012, *AJ*, 143, 38
- Gwyn, S. D. J., Hill, N., & Kavelaars, J. J. 2012, *Publ. Astron. Soc. Pac.*, 124, 579
- Haghighipour, N. 2009, *Proceedings of the International Astronomical Union*, 5, 207–214
- Haghighipour, N., Maindl, T. I., Schäfer, C., Speith, R., & Dvorak, R. 2016, *ApJ*, 830, 22
- Haghighipour, N., Maindl, T. I., Schäfer, C. M., & Wandel, O. J. 2018, *ApJ*, 855, 60
- Hainaut, O. R., Kleyna, J., Sarid, G., et al. 2012, *A&A*, 537, A69
- Hanner, M. S., Giese, R. H., Weiss, K., & Zerull, R. 1981, *A&A*, 104, 42
- Haranas, I., Shehata, Y. M., Cobbett, K., et al. 2023, *Earth Moon and Planets*, 127, 3
- Harris, A. W. & D'Abramo, G. 2015, *Icarus*, 257, 302
- Hartzell, C. M. & Scheeres, D. J. 2011, *Planet. Space Sci.*, 59, 1758
- Hills, J. G. 1981, *AJ*, 86, 1730
- Hirayama, K. 1918, *AJ*, 31, 185

- Hofmann, M., Sierks, H., & Blum, J. 2017, *MNRAS*, 469, S73
- Holmberg, J., Flynn, C., & Portinari, L. 2006, *MNRAS*, 367, 449
- Hsieh, H., Ishiguro, M., Knight, M. M., et al. 2018, in *AAS/Division for Planetary Sciences Meeting Abstracts*, Vol. 50, *AAS/Division for Planetary Sciences Meeting Abstracts #50*, 408.06
- Hsieh, H. H. 2014, *Icarus*, 243, 16
- Hsieh, H. H. 2015, *Proceedings of the International Astronomical Union*, 10, 99–110
- Hsieh, H. H., Denneau, L., Wainscoat, R. J., et al. 2015, *Icarus*, 248, 289
- Hsieh, H. H. & Haghighipour, N. 2016, *Icarus*, 277, 19
- Hsieh, H. H., Hainaut, O., Novaković, B., et al. 2015, *ApJ*, 800, L16
- Hsieh, H. H., Ishiguro, M., Kim, Y., et al. 2018a, *AJ*, 156, 223
- Hsieh, H. H., Ishiguro, M., Kim, Y., et al. 2018b, *The Astronomical Journal*, 156, 223
- Hsieh, H. H., Ishiguro, M., Knight, M. M., et al. 2021, *Planet. Sci.*, 2, 62
- Hsieh, H. H., Ishiguro, M., Lacerda, P., & Jewitt, D. 2011, *AJ*, 142, 29
- Hsieh, H. H. & Jewitt, D. 2006, *Science*, 312, 561
- Hsieh, H. H., Jewitt, D., & Fernández, Y. R. 2009, *ApJ*, 694, L111
- Hsieh, H. H., Jewitt, D., & Ishiguro, M. 2008, *AJ*, 137, 157
- Hsieh, H. H., Jewitt, D., Lacerda, P., Lowry, S. C., & Snodgrass, C. 2010, *MNRAS*, 403, 363
- Hsieh, H. H., Jewitt, D. C., & Fernández, Y. R. 2004, *AJ*, 127, 2997
- Hsieh, H. H., Meech, K. J., & Pittichová, J. 2011, *ApJ*, 736, L18
- Hsieh, H. H., Micheli, M., Kelley, M. S. P., et al. 2023, *Planet. Sci.*, 4, 43
- Hsieh, H. H., Novaković, B., Kim, Y., & Brassier, R. 2018c, *AJ*, 155, 96
- Hsieh, H. H. & Sheppard, S. S. 2015, *MNRASL*, 454, L81
- Hsieh, H. H., Yang, B., Haghighipour, N., et al. 2012a, *ApJ*, 748, L15
- Hsieh, H. H., Yang, B., Haghighipour, N., et al. 2012b, *AJ*, 143, 104
- Huebner, W. F., Benkhoff, J., Capria, M.-T., et al., eds. 2006, *Heat and Gas Diffusion in Comet Nuclei*
- Hughes, A. L. H., Colwell, J. E., & DeWolfe, A. W. 2008, *Icarus*, 195, 630
- Hughes, D. W. 1991, in *Astrophysics and Space Science Library*, Vol. 167, *IAU Colloq. 116: Comets in the post-Halley era*, ed. J. Newburn, R. L., M. Neugebauer, & J. Rahe, 825

- Hui, M.-T. & Jewitt, D. 2017, *AJ*, 153, 80
- Hyland, D., Altwajry, H., Kim, H. S., Satak, N., & Ge, S. 2013, in
IRAC Instrument and Instrument Support Teams. 2021, *IRAC Instrument Handbook*, data type:
Text
- Irwin, M. & Lewis, J. 2001, *New A Rev.*, 45, 105
- Ishiguro, M. 2008, *Icarus*, 193, 96
- Ishiguro, M., Hanayama, H., Hasegawa, S., et al. 2011, *ApJL*, 741, L24
- Jacobson, S. A. & Scheeres, D. J. 2011, *Icarus*, 214, 161
- Jarosewich, E. 1990, *Meteoritics*, 25, 323
- Jewitt, D. 1992, 30, 85
- Jewitt, D. 1996, *Earth Moon and Planets*, 72, 185
- Jewitt, D. 2012, *AJ*, 143, 66
- Jewitt, D., Agarwal, J., Li, J., et al. 2014a, *ApJL*, 784, L8
- Jewitt, D., Agarwal, J., Weaver, H., Mutchler, M., & Larson, S. 2013, *ApJL*, 778, L21
- Jewitt, D., Agarwal, J., Weaver, H., et al. 2016, *AJ*, 152, 77
- Jewitt, D., Hsieh, H., & Agarwal, J. 2015, in *Asteroids IV* (University of Arizona Press)
- Jewitt, D., Ishiguro, M., Weaver, H., et al. 2014b, *AJ*, 147, 117
- Jewitt, D. & Meech, K. J. 1988, *AJ*, 96, 1723
- Jewitt, D., Weaver, H., Mutchler, M., Larson, S., & Agarwal, J. 2011, *ApJL*, 733, L4
- Jewitt, D., Yang, B., & Haghhighipour, N. 2009, *AJ*, 137, 4313
- Jewitt, D., Yang, B., & Haghhighipour, N. 2009, *AJ*, 137, 4313
- Joss, P. C. 1973, *A&A*, 25, 271
- Joye, W. A. 2006, in *Astronomical Society of the Pacific Conference Series*, Vol. 351, *Astronomical Data Analysis Software and Systems XV*, ed. C. Gabriel, C. Arviset, D. Ponz, & S. Enrique, 574
- Juan Luis Cano Rodríguez & Jorge Martínez Garrido. 2022, in *Proceedings of the 21st Python in Science Conference*, ed. Meghann Agarwal, Chris Calloway, Dillon Niederhut, & David Shupe, 136 – 146
- Kar, K. K. 2022, *Handbook of fly ash* / Kamal K. Kar. (London, UK: Elsevier Science Technology)
- Kelley, M. S. P., Hsieh, H. H., Bodewits, D., et al. 2023, *Nature*

- Kerridge, J. F. 1993, *Antarctic Meteorite Research*, 6, 293
- Kim, Y., Agarwal, J., Jewitt, D., et al. 2022, *A&A*, 666, A163
- Kim, Y., Ishiguro, M., & Lee, M. G. 2017a, *ApJ*, 842, L23
- Kim, Y., Ishiguro, M., Michikami, T., & Nakamura, A. M. 2017b, *AJ*, 153, 228
- Kirkwood, D. 1867, *Meteoric Astronomy: A Treatise on Shooting-stars, Fire-balls, and Aerolites* (J.B. Lippincott & Company)
- Klioner, S. A. 2016, *Basic Celestial Mechanics*
- Kolokolova, L., Hanner, M. S., Lvasseur-Regourd, A.-C., Gustafson, B. A. S., & Binzel, R. P. 2004, *Physical Properties of Cometary Dust from Light Scattering and Thermal Emission* (University of Arizona Press), 577–604
- Kosai, H. 1992, *Celestial Mechanics and Dynamical Astronomy*, 54, 237
- Kresak, L. 1982, *Bulletin of the Astronomical Institutes of Czechoslovakia*, 33, 104
- Krot, A. N., Keil, K., Goodrich, C. A., Scott, E. R. D., & Weisberg, M. K. 2003, *Treatise on Geochemistry*, 1, 711
- Küppers, M., O’Rourke, L., Bockelée-Morvan, D., et al. 2014, *Nature*, 505, 525
- Labrie, K., Simpson, C., Cardenes, R., et al. 2023, *Research Notes of the American Astronomical Society*, 7, 214
- Lagerkvist, C. I. & Magnusson, P. 1990, *A&AS*, 86, 119
- Levasseur-Regourd, A.-C., Agarwal, J., Cottin, H., et al. 2018, *Space Sci. Rev.*, 214, 64
- Levison, H. F. 1996, in *Astronomical Society of the Pacific Conference Series*, Vol. 107, *Completing the Inventory of the Solar System*, ed. T. Rettig & J. M. Hahn, 173–191
- Libanore, S. & Kovetz, E. D. 2024, *A&A*, 687, A133
- Licandro, J., Campins, H., Tozzi, G. P., et al. 2011, *A&A*, 532, A65
- Licandro, J., Tancredi, G., Lindgren, M., Rickman, H., & Hutton, R. G. 2000, *Icarus*, 147, 161
- Lupishko, D. F. & Mohamed, R. A. 2009, *Solar System Research*, 43, 475
- Magnier, E. 2006, in *The Advanced Maui Optical and Space Surveillance Technologies Conference*, E50
- Magnier, E. A. & Cuillandre, J. C. 2004, *PASP*, 116, 449
- Maindl, T. I. & Haghhighipour, N. 2014, in *AAS/Division for Planetary Sciences Meeting Abstracts*, Vol. 46, *AAS/Division for Planetary Sciences Meeting Abstracts #46*, 415.17
- Maindl, T. I., Haghhighipour, N., Schäfer, C., & Speith, R. 2016, in *The Astrophysics of Planetary Habitability*, 156–156

- Mainzer, A., Grav, T., Masiero, J., et al. 2011, *ApJ*, 736, 100
- Mainzer, A. K., Bauer, J. M., Cutri, R. M., et al. 2019, NEOWISE Diameters and Albedos V2.0, NASA Planetary Data System, urn:nasa:pds:neowise_diameters_albedos::2.0
- Makishima, A. 2017, in *Origins of the Earth, Moon, and Life*, ed. A. Makishima (Elsevier), 1–24
- Marboeuf, U. & Schmitt, B. 2014, *Icarus*, 242, 225
- Marinelli, M. & Dressel, L. 2024, *Wide Field Camera 3 Instrument Handbook, Version 16.0* (Baltimore, MD: Space Telescope Science Institute)
- Marschall, R., Markkanen, J., Gerig, S.-B., et al. 2020, *Frontiers in Physics*, 8, 227
- Marzari, F., Rossi, A., & Scheeres, D. J. 2011, *Icarus*, 214, 622
- Masiero, J. R., Mainzer, A. K., Grav, T., et al. 2011, *ApJ*, 741, 68
- Masiero, J. R., Wright, E. L., & Mainzer, A. K. 2021, *Planet. Sci.*, 2, 32
- Mastropietro, M., Hsieh, H., Kim, Y., & Agarwal, J. 2022, in *European Planetary Science Congress, EPSC2022–1211*
- Mastropietro, M., Kim, Y., Hsieh, H. H., & Agarwal, J. 2023, in *LPI Contributions, Vol. 2851, LPI Contributions*, 2041
- Mastropietro, M., Kim, Y., Hsieh, H. H., & Agarwal, J. 2024a, *AA*, 690, A298
- Mastropietro, M., Krishna, H., Kim, Y., & Agarwal, J. 2024b, *Research Notes of the American Astronomical Society*, 8, 104
- Mazeeva, O. A. 2004, *Solar System Research*, 38, 325
- McCord, T. B., Adams, J. B., & Johnson, T. V. 1970, *Science*, 168, 1445
- Meech, K. J. & Jewitt, D. 1987, *Nature*, 328, 506
- Meech, K. J. & Svoren, J. 2004, in *Comets II*, ed. M. C. Festou, H. U. Keller, & H. A. Weaver, 317
- Mink, D. J. 1997, in *Astronomical Society of the Pacific Conference Series, Vol. 125, Astronomical Data Analysis Software and Systems VI*, ed. G. Hunt & H. Payne, 249
- Montenbruck, O. & Gill, E. 2000, *Introductory Astrodynamics* (Berlin, Heidelberg: Springer Berlin Heidelberg), 15–51
- Moore, P. 2005, in *Encyclopedia of Geology*, ed. R. C. Selley, L. R. M. Cocks, & I. R. Plimer (Oxford: Elsevier), 220–227
- Moreno, F., Cabrera-Lavers, A., Vaduvescu, O., Licandro, J., & Pozuelos, F. 2013, *ApJL*, 770, L30
- Moreno, F., Lara, L. M., Licandro, J., et al. 2011, *ApJL*, 738, L16

- Moreno, F., Licandro, J., Tozzi, G. P., et al. 2010, *ApJ*, 718, L132
- Mumma, M. J., Weissman, P. R., & Stern, S. A. 1993, in *Protostars and Planets III*, ed. E. H. Levy & J. I. Lunine, 1177
- Newman, M. E. J. 2005, *Contemporary Physics*, 46, 323
- Nomen, J., Birtwhistle, P., Holmes, R., Foglia, S., & Scotti, J. V. 2010, *Central Bureau Electronic Telegrams*, 2459, 1
- Oort, J. H. 1950, *Bull. Astron. Inst. Netherlands*, 11, 91
- Ootsubo, T., Kawakita, H., Hamada, S., et al. 2011, in *EPSC-DPS Joint Meeting 2011*, Vol. 2011, 369
- Ootsubo, T., Kawakita, H., Hamada, S., et al. 2012, *The Astrophysical Journal*, 752, 15
- Pfalzner, S., Davies, M. B., Gounelle, M., et al. 2015, *Phys. Scr*, 90, 068001
- Poch, O., Pommerol, A., Fray, N., & Gundlach, B. 2023, *Laboratory Experiments to Understand Comets*
- Polishook, D. & Brosch, N. 2009, *Icarus*, 199, 319
- Pössel, M. 2020, *The Open Journal of Astrophysics*, 3, 2
- Pozuelos, F. J., Cabrera-Lavers, A., Licandro, J., & Moreno, F. 2015, *ApJ*, 806, 102
- Prialnik, D. & Rosenberg, E. D. 2009, *MNRASL*, 399, L79
- Quirico, E., Moroz, L., Schmitt, B., et al. 2016, *Icarus*, 272, 32
- Reach, W. T., Kelley, M. S., & Vaubaillon, J. 2013, *Icarus*, 226, 777
- Reach, W. T., Sykes, M. V., Lien, D., & Davies, J. K. 2000, *Icarus*, 148, 80
- Rickman, H. 2010, in *Lecture Notes in Physics*, Berlin Springer Verlag, ed. J. Souchay & R. Dvorak, Vol. 790, 341–399
- Roemer, E. 1962, *Publications of the Astronomical Society of the Pacific*, 74, 351
- Rubincam, D. P. 1987, *J. Geophys. Res.*, 92, 1287
- Rubincam, D. P. 1995, *J. Geophys. Res.*, 100, 1585
- Rubincam, D. P. 1998, *J. Geophys. Res.*, 103, 1725
- Rubincam, D. P. 2000, *Icarus*, 148, 2
- Russell, H. N. 1916, *ApJ*, 43, 173
- Saito, T., Kozuka, Y., Saito, K., & Minami, S. 1994, *Plasma Tail and Dust Tail of Comets*, ed. H. Kikuchi (Boston, MA: Springer US), 55–71
- Sarmecanic, J., Fomenkova, M., Jones, B., & Lavezzi, T. 1997, *ApJ*, 483, L69

- Schleicher, D. 2010, Composite Dust Phase Function for Comets, <https://asteroid.lowe11.edu/comet/dustphase/>, Accessed: July 3, 2024
- Schorghofer, N. 2008, *ApJ*, 682, 697
- Schorghofer, N. 2016, *Icarus*, 276, 88
- Schörghofer, N. & Hsieh, H. H. 2018, *Journal of Geophysical Research (Planets)*, 123, 2322
- Scott, E. R. D. & Krot, A. N. 2003, *Treatise on Geochemistry*, 1, 711
- Sekanina, Z. 1996, *A&A*, 314, 957
- Sekanina, Z., Chodas, P. W., & Yeomans, D. K. 1994, *A&A*, 289, 607
- Sekanina, Z., Larson, S. M., Hainaut, O., Smette, A., & West, R. M. 1992, *A&A*, 263, 367
- Sheppard, S. S. & Trujillo, C. 2015, *AJ*, 149, 44
- Simpson, C., Labrie, K., Teal, D., et al. 2024, DRAGONS
- Skorov, Y., Keller, H. U., Mottola, S., & Hartogh, P. 2020, *Monthly Notices of the Royal Astronomical Society*, 494, 3310
- Smithsonian Astrophysical Observatory. 2000, SAOImage DS9: A utility for displaying astronomical images in the X11 window environment, *Astrophysics Source Code Library*, record ascl:0003.002
- Snodgrass, C., Agarwal, J., Combi, M., et al. 2017, *A&A Rev.*, 25, 5
- Snodgrass, C., Jones, G. H., Boehnhardt, H., et al. 2018, *Advances in Space Research*, 62, 1947
- Snodgrass, C., Tubiana, C., Vincent, J.-B., et al. 2010, *Nature*, 467, 814
- Sonnett, S., Kleyna, J., Jedicke, R., & Masiero, J. 2011, *Icarus*, 215, 534
- Spohn, T. 2011, *Small Solar System Body*, ed. M. Gargaud, R. Amils, J. C. Quintanilla, H. J. J. Cleaves, W. M. Irvine, D. L. Pinti, & M. Viso (Berlin, Heidelberg: Springer Berlin Heidelberg), 1516–1517
- Steckloff, J. K., Graves, K., Hirabayashi, M., Melosh, H. J., & Richardson, J. E. 2016, *Icarus*, 272, 60
- Stern, S. A. 1995, *AJ*, 110, 856
- Strazzulla, G., Pirronello, V., & Foti, G. 1983, *A&A*, 123, 93
- Sunshine, J. M., Groussin, O., Schultz, P. H., et al. 2007, *Icarus*, 190, 284, deep Impact Mission to Comet 9P/Tempel 1, Part 2
- Szebehely, V. 1967, in *Theory of Orbit*, ed. V. Szebehely (Academic Press), 7–41
- Taylor, G. & Scott, E. 2003, in *Treatise on Geochemistry*, ed. H. D. Holland & K. K. Turekian (Oxford: Pergamon), 477–485

- Tedesco, E. F. 1979, *Icarus*, 40, 375
- Thiel, K., Koelzer, G., Kochan, H., et al. 1989, 302, 221
- Tholen, D. J. 1984, PhD thesis, University of Arizona
- Tholen, D. J. & Barucci, M. A. 1989, in *Asteroids II*, ed. R. P. Binzel, T. Gehrels, & M. S. Matthews, 298–315
- Tisserand. 1891, *Traité de mécanique céleste*, *Traité de mécanique céleste* No. Bd. 2 (Gauthier-Villars)
- Tody, D. 1986, in *Society of Photo-Optical Instrumentation Engineers (SPIE) Conference Series*, Vol. 627, *Instrumentation in astronomy VI*, ed. D. L. Crawford, 733
- Tody, D. 1993, in *Astronomical Society of the Pacific Conference Series*, Vol. 52, *Astronomical Data Analysis Software and Systems II*, ed. R. J. Hanisch, R. J. V. Brissenden, & J. Barnes, 173
- Tommei, G. 2019, in *1st NEO and Debris Detection Conference_ESA2019*, 16
- Tommei, G. 2021, *Universe*, 7
- Tonry, J. L., Stubbs, C. W., Lykke, K. R., et al. 2012, *ApJ*, 750, 99
- Tsuchiyama, A. 2014, *Elements*, 10, 45
- Vincent, J. 2014, in *Asteroids, Comets, Meteors 2014*, ed. K. Muinonen, A. Penttilä, M. Granvik, A. Virkki, G. Fedorets, O. Wilkman, & T. Kohout, 565
- Vincent, J.-B., Bodewits, D., Besse, S., et al. 2015, *Nature*, 523, 63
- Vokrouhlický, D. & Farinella, P. 1998, *AJ*, 116, 2032
- Vokrouhlický, D. & Farinella, P. 1999, *AJ*, 118, 3049
- Vokrouhlický, D. & Čapek, D. 2002, *Icarus*, 159, 449
- Warner, B. D., Harris, A. W., & Pravec, P. 2009, *Icarus*, 202, 134
- Wasson, J. T. 1985, *Meteorites : their record of early solar-system history*
- Weisberg, M. K., McCoy, T. J., & Krot, A. N. 2006, in *Meteorites and the Early Solar System II*, ed. D. S. Lauretta & H. Y. McSween, 19
- Whipple, F. L. 1950, *ApJ*, 111, 375
- Whitney, C. 1955, *ApJ*, 122, 190
- Williams, D. M., Mason, C. G., Gehrz, R. D., et al. 1997, *ApJ*, 489, L91
- Willmer, C. N. A. 2018, *ApJS*, 236, 47
- Woitke, P., Drażkowska, J., Lammer, H., Kadam, K., & Marigo, P. 2024, arXiv e-prints, arXiv:2404.15715

- Womack, M., Sarid, G., & Wierzchos, K. 2017, *PASP*, 129, 031001
- Wood, J. 2019, *The Dynamics of Small Solar System Bodies*
- Wright, E. L., Eisenhardt, P. R. M., Mainzer, A. K., et al. 2010, *AJ*, 140, 1868
- Xin, Y., Shi, J., & Ma, Y. 2024, *MNRAS*, 527, 10309
- Xu, S., Binzel, R. P., Burbine, T. H., & Bus, S. J. 1995, *Icarus*, 115, 1
- Yamamoto, T. 1985, *A&A*, 142, 31
- Yang, B., Jewitt, D., & Bus, S. J. 2009, *AJ*, 137, 4538
- Yang, J., Goldstein, J. I., & Scott, E. R. D. 2007, *Nature*, 446, 888
- Zolensky, M. & McSween, Harry Y., J. 1988, in *Meteorites and the Early Solar System*, ed. J. F. Kerridge & M. S. Matthews, 114–143
- Żółtowski, M., Lique, F., Loreau, J., Faure, A., & Cordiner, M. 2023, *MNRAS*, 520, 3887

Publications and conference proceedings

- Mastropietro, M., Kim, Y., Hsieh, H. H., and Agarwal, J. (2024). "*Activity of main-belt comet 324P/La Sagra*", *A&A*, 690, A298, DOI: 10.1051/0004-6361/202451090 - Journal article.
On arXiv, DOI: 10.48550/arXiv.2411.02034.
- Mastropietro, M., Kim, Y., and Agarwal, J. (2024). "*Dust dynamics modelling on the main-belt comet 324P/La Sagra*", Europlanet Science Congress 2024, Berlin, Germany, 8–13 Sep 2024, EPSC2024-153, DOI: 10.5194/epsc2024-153 - Conference abstract.
- Mastropietro, M., Krishna, H., Kim, Y., and Agarwal, J. (2024). "*Photometric Analysis of the Nucleus of the Main-belt Comet 2010 LH15*", *Research Notes of the American Astronomical Society*, 8(4), 104, DOI: 10.3847/2515-5172/ad3e85 - Journal article.
- Mastropietro, M., Kim, Y., Hsieh, H. H., and Agarwal, J. (2023). "*Activity of the Main-Belt Comet 324P/La Sagra*", Asteroids, Comets, Meteors Conference, Flagstaff, Arizona, 18-23 Jun 2023, LPI Contributions 2851, 2041, BIBCODE: 2023LPICo2851.2041M - Conference paper.
- Mastropietro, M., Hsieh, H., Kim, Y., and Agarwal, J. (2022). "*Activity of the Main-Belt Comet 324P/La Sagra*", Europlanet Science Congress 2022, Granada, Spain, 18–23 Sep 2022, EPSC2022-1211, DOI: 10.5194/epsc2022-1211 - Conference abstract.

Curriculum Vitae

Personal Information

Name: Maria Mastropietro

Date of Birth: 28.10.1995

Nationality: Italian

ORCID: orcid.org/0000-0002-4966-4639

ADS Publications: ADS Library

LinkedIn: [linkedin.com/in/m-mastropietro](https://www.linkedin.com/in/m-mastropietro)

Education

Jun 2021 - Apr 2025

PhD Researcher in Astronomy and Physics

Institut für Geophysik und Extraterrestrische Physik, Braunschweig, Germany

Thesis Title: Activity of the main-belt comet 324P/La Sagra

Supervisor: Prof. Dr. Jessica Agarwal

Nov 2019 - Jan 2020

24 Credits for teaching

Post graduate certification (eCAMPUS Telematic University), Padova, Italy

Courses: Antro-psycho-pedagogic disciplines and Teaching methodologies and technologies

Sep 2017 - Sep 2019

Master of Science in Astronomy

Padova University, Italy

Thesis Title: Analysis of Oxia Planum region (Mars): the landing site of the ESA ExoMars 2020 rover

Supervisor: Prof. Dr. Monica Lazzarin

Co-supervisors: Prof. Dr. Gabriele Cremonese and Dr. Maurizio Pajola

Sep 2014 - Oct 2017

Bachelor of Science in Astronomy

Padova University, Italy

Thesis Title: Il rapporto D/H nel Sistema Solare

Supervisor: Prof. Dr. Monica Lazzarin

Achievements

Feb 2022 - Apr 2025

PhD scholarship

International Max Planck Research School for Solar System Science at the University of Göttingen, Germany

Supervision experience

Dec 2023 - Jan 2024

Praktikum project supervision

Institut für Geophysik und Extraterrestrische Physik, Braunschweig, Germany

Project title: Photometric Analysis of a Newly Discovered Main-Belt Comet

Supervisor: Prof. Dr. Jessica Agarwal

Co-supervisor: Maria Mastropietro

Institutional service

Jan 2025

Exercise sessions "Interiors and Surfaces of Planetary Bodies" (Block 3)

Institut für Geophysik und Extraterrestrische Physik, Braunschweig, Germany

Apr 2023 - Jul 2024

Oberseminar organization at IGEP

Institut für Geophysik und Extraterrestrische Physik, Braunschweig, Germany

Working experience

Oct 2020 - May 2021

High school teacher

Liceo Artistico Modigliani, Padova, Italy

Acknowledgments

I would like to sincerely thank all those who supported me during the completion of this thesis.

First, I would like to express my deep gratitude to my supervisor, Prof. Dr. Jessica Agarwal, for her guidance, feedback, and encouragement throughout this project. Her expertise and support were invaluable to my work.

I also extend my thanks to the faculty and staff at the Institut für Geophysik und Extraterrestrische Physik in Braunschweig and the Max Planck Institute for Solar System Research in Göttingen. Special thanks go to Dr. Sonja Schuh for supporting my application to the PhD program at the IMPRS, as well as to the committee that decided to accept me into the program. I also thank the PhD students for the shared time in courses and during the retreat.

I am very thankful to my family and friends for their support and understanding throughout this journey. Un ringraziamento speciale ai miei genitori, per il loro amore e il loro costante incoraggiamento, anche da lontano.

I would also like to express my gratitude to my Indian friends I met here in Braunschweig. The time we spent together and the memories we shared have made this journey both enjoyable and memorable.

Lastly, I would like to thank my colleagues Manuela, Pablo, Yoonyoung, Johannes, Yuna, Marius, Nick, and Oriol, for their collaboration and the valuable exchange of ideas during this academic journey.

Thank you all.